東京大学
THE UNIVERSITY OF TOKYO

Master Thesis
修士論文

Design of Al-free GaAs based 1000 nm semiconductor optical amplifier for application to optical phased array

(光フェーズドアレイ応用に向けたAlフリーGaAs系
1000nm半導体光増幅器の設計)

Théophile Seijiro Mascia

37-186517

Academic year 2020

Department of Electrical Engineering and Information Systems
Graduate School of Engineering, The University of Tokyo

Research Supervisor
Prof. Yoshiaki Nakano

Contents

Acknowledgments

The work presented in this thesis was my first experience with conducting a research project. Completing it at the laboratory of Professor Nakano was a privilege and provided me with robust and wide knowledge that are invaluable not only for my future carrier, but also for my personal development. I also hope that this document and the associated Python code will be useful for future fellows that will start a research in the fascinating field of semiconductor optical devices, as I did put a lot of efforts in writing it as clearly as possible. I would like to express here my deep and sincere gratitude to all the people that not only have helped me for my research in one of the most challenging domain of physics, but also provided strong mental support and counseling during very difficult moments that were exacerbated by the sad coronavirus pandemic.

Professor Yoshiaki Nakano, my supervising professor, gave me the opportunity to join and study in Japan from France, and warmly welcomed me to his laboratory where I had the chance to meet many members with great personalities and intelligence. He gave me much valuable advice about my research, which were decisive for the progress of my work. He also generously offered to extend my stay at the laboratory for six months to compensate for the time lost on the sanitary situation. I efficiently took advantage of this extra period of time to deepen my understanding of the physical phenomena involved in active semiconductor optical devices and to achieve a more refined research project.

I also thank associate professor Takuo Tanemura for his guidance and for the many ideas that I would never have got by myself. He tremendously supported me at the onset of, and throughout my research and generously dedicated a lot of his time to me. At the beginning of my first research project ever, his repeated advice was essential for me to make the first and most important steps. He also introduced me to the lab's members with whom I had fruitful discussions and built strong friendship.

Former student Shota Onoduka, who accomplished his master degree in spring 2020, helped me on many occasions not only about the content of my research, but also regarding the student life at the University of Tokyo. The many conversations I had with him were all interesting and fun at the same time, and he was always eager to tell me about anything I asked.

I would also like to kindly salute all the other fellow lab's members from whom I learned notably during the meetings and presentation practices. I took inspiration from their motivation, outstanding knowledge and insights to improve my research.

Last but not least, I am also sincerely grateful to my family for staying by my side, for supporting me at times of doubts and for providing the best environment imaginable to achieve my work which was another challenging exercise of my life.

Notations, conventions and alloy parameters

Vectors are denoted in bold fonts. For instance, the position and wave vectors in the Euclidean space are noted $\mathbf{r} = \begin{pmatrix} x \\ y \\ z \end{pmatrix}$ and $\mathbf{k} = \begin{pmatrix} k_x \\ k_y \\ k_z \end{pmatrix}$ and the momentum of operator is noted $\mathbf{p} = \begin{pmatrix} p_x \\ p_y \\ p_z \end{pmatrix} = \begin{pmatrix} -i\hbar\frac{\partial}{\partial x} \\ -i\hbar\frac{\partial}{\partial y} \\ -i\hbar\frac{\partial}{\partial z} \end{pmatrix}$

Wave propagation is always along the z-direction.

We use the International System of Units.

$\lfloor \rfloor$ denotes the floor function.
$\mathbb{1}_P$ denotes the indicator function, equal to 1 if the proposition P is true and 0 otherwise.

Physical constants

m_0	kg	Electronic mass.
c	m s^{-1}	Speed of light.
k or k_B	J K^{-1}	Boltzmann constant.
q or e	C	Elementary charge.
h	J s	Planck constant.
$\hbar$	J s $radian^{-1}$	Planck constant, $\hbar = \frac{h}{2\pi}$.
ε_0	F m^{-1}	Vacuum permittivity.

Main variables

L	m	Length of the device in the direction z of light propagation.
d_x or d	m	Width of a well layer in the direction x.
w	m	Width of the device in the direction y.
N	m^{-3}	Electron carrier density along the axis z.
P	m^{-3}	Hole carrier density along the axis z.
N_P	m^{-3}	Photon density along the axis z.
I	A	Injection current.
η_i	-	Efficiency of the injection current.
Γ	-	Optical confinement factor.
τ	s	Miscellaneous lifetimes.
R_{st}	$\mathrm{m}^{-3}\ \mathrm{s}^{-1}$	Transition rate of net stimulated emission. $R_{st} = g v_g N_p$
v_g	$\mathrm{m\ s}^{-1}$	Group velocity of light.
g	m^{-1}	Gain along z as function of z and N. $g = \frac{1}{N_p}\frac{dN_p}{dz}$.
$G_0(L)$	-	Unsaturated total gain over the length of the device.
$G(L)$	-	Total gain over the length of the device.
a	m^2	The differential gain, $a = \frac{dg}{dN}$. or Lattice constant.
ε_{xx}	-	Compression and tensile strain $\varepsilon_{xx} = \frac{\Delta a}{a}$.
n	-	Refractive index of material. $n = \frac{c}{v}$ with v the phase velocity of light in the material.
P_{o_s}	$\mathrm{J\ s}^{-1}$	Saturation output power where the total gain is half of the gain at low powers.
ν	s^{-1}	Photon frequency. $\nu = \frac{c}{\lambda}$.
λ	m	Photon wavelength.
ω	radian s^{-1}	Photon angular frequency. $\omega = 2\pi\nu$.
E_1, E_2	J	During a transition, the states of an electron in the valence and the conduction bands are respectively indexed by 1 and 2. E_1 is the energy of the electron before it leaves or when it reaches the valence band. E_2 is its energy in the conduction band.
E_{21}	J	$E_{21} = E_2 - E_1$
E_{F_c}	J	Quasi Fermi level for conduction band.
E_{F_v}	J	Quasi Fermi level for valence band.
E_c	J	Energy at the bottom of the conduction band.
E_v	J	Energy at the top of the valence band.
E_g	J	Band gap at the Γ point for direct band gap semiconductors. $E_g = E_c - E_v$.
m_c, m_v	kg	Effective masses of electrons in the conduction and valence bands.
m_r	kg	Reduced mass used to compute the reduced density of states. $\frac{1}{m_r} = \frac{1}{m_c} + \frac{1}{m_v}$.
$\rho(E)$	$\mathrm{J}^{-1}\ \mathrm{m}^{-3}$	Density of states.
$\rho_r(E)$	$\mathrm{J}^{-1}\ \mathrm{m}^{-3}$	Reduced density of states, or density of transition pairs.
M_T	$\mathrm{kg}^{\frac{1}{2}}\ \mathrm{J}^{\frac{1}{2}}$	Transition matrix element.
$f(E)$	-	Fermi statistics that gives a probability of occupation of states.
E_1^∞	J	Minimum quantum of energy for a well of infinite potential. $E_1^\infty = \frac{1}{2m}\left(\frac{\hbar\pi}{d}\right)^2$.
ψ		Wave function of an electron.
ϕ		Bloch wave functions, that form a basis of periodic solutions of the Schrödinger equation applied to the one-electron Hamiltonian.
$\mathbf{r}$		Position vector.
$\mathbf{k}$		Wave vector.
$\mathbf{p}$		Hermitian momentum operator.
$\mathbf{p}^2$		$\mathbf{p}^2 = -\hbar^2\nabla^2 = -\hbar^2\Delta$, where ∇ and Δ are the gradient and the Laplacian operators. $\Delta = \nabla^2 = \frac{\partial^2}{\partial x^2} + \frac{\partial^2}{\partial y^2} + \frac{\partial^2}{\partial z^2}$

Parameter	Gap	a	$E_g^\Gamma(0K)$	A^Γ	B^Γ	$E_g^\Gamma(300K)$	E_v^0	Δ_0	$\bar{E}_v^0$
Unit	-	($\mathring{A}$)	(eV)	(meV/K)	(K)	(eV)	(eV)	(eV)	(eV)
GaAs	Γ	5.6533	1.52	0.54	204	1.422	-0.8	0.341	-6.92
InP	Γ	5.8688	1.42	0.36	162	1.353	-0.49	0.108	-7.04
AlAs	X	5.66	3.1	0.89	530	3.003	-1.33	0.28	-7.49
GaSb	Γ	6.0959	0.81	0.42	140	0.727	-0.03	0.76	-6.25
AlSb	X	5.66	2.39	0.42	140	2.3	-0.41	0.676	-6.66
InAs	Γ	6.0583	0.42	0.28	93	0.354	-0.59	0.39	-6.67
GaP	X	5.4505	2.89			2.757	-1.27	0.08	-7.4
AlP	X	5.4635	3.63	0.58	372	3.553	-1.74	0.07	-8.09
InSb	Γ	6.4794	0.24	0.32	170	0.174	0	0.81	-6.09

Table 1: Lattice constant a, energy band gaps at Γ point for $T = 0K$ and $T = 300K$ and corresponding Varshni parameters A and B, valence band edge reference level E_v^0, split-off energy Δ_0 and averge valence band energy $\bar{E}_v^0$ (main source: [68], [19]). For GaP, $E_g^\Gamma(T)$ is calculated with Takizawa formula ([92]): $E = 2.866 - 0.108\big(\coth\frac{168}{T} - 1\big)$

Parameter	m_c	m_{hh}	m_{lh}	m_{so}	$n(1\mu m)$	E_p	F_b
Unit	($\times\, m_0$)	($\times\, m_0$)	($\times\, m_0$)	($\times\, m_0$)	-	(eV)	-
GaAs	0.067	0.5	0.076	0.14	3.5	28.8	-1.94
InP	0.0795	0.56	0.12	0.12	3.41	20.7	-1.31
AlAs	0.15	0.76	0.15	0.24	2.95	21.1	-0.48
GaSb	0.039	0.28	0.05	0.13	4.16	27	-1.63
AlSb	0.14	0.94	0.14	0.29	3.42	18.7	-0.56
InAs	0.026	0.57	0.025	0.14	3.55	21.5	-2.9
GaP	0.13	0.79	0.14	0.46	3.18	31.4	-2.04
AlP	0.22	0.63	0.2	0.29	2.75	17.7	-0.65
InSb	0.0135	0.43	0.015	0.19	4.05	23.3	-0.23

Table 2: Effective masses of holes in multiple of m_0 at room temperature, refactive index at $1\mu m$ (main source: [68])

	Bulk		Well	
Polarization	c-hh	c-lh	c-hh	c-lh
TE	1/3	1/3	1/2	1/6
TM	1/3	1/3	0	2/3

Table 3: $\frac{|M_T|^2}{|M|^2}$

Parameter **Unit**	γ_1 -	γ_2 -	γ_3 -	C_{11} (GPa)	C_{12} (GPa)	b (eV)	a_v (eV)	a_c (eV)
GaAs	6.98	2.06	2.93	1221	566	-2	1.16	-7.17
InP	5.08	1.6	2.1	1011	561	-2	0.6	-6
AlAs	3.76	0.82	1.42	1250	534	-2.3	2.47	-5.64
GaSb	13.4	4.7	6	884.2	402.6	-2	0.8	-7.5
AlSb	5.18	1.19	1.97	876.9	434.1	-1.35	1.4	-4.5
InAs	20	8.5	9.2	832.9	452.6	-1.8	1	-5.08
GaP	4.05	0.49	2.93	1405	620.3	-1.6	1.7	-8.2
AlP	3.35	0.71	1.23	1330	630	-1.5	3	-5.7
InSb	34.8	15.5	16.5	684.7	373.5	-2	0.36	-6.94

Table 4: Luttinger parameters γ_1, γ_2 and γ_3, elastic stiffness constants C_{11} and C_{12} and deformation poentials b, a_v and a_c for cubic semiconductors at room temperature (source: [68])

Parameter **Unit**	$C(E_g^\Gamma)$ (eV)	$C(E_g^X)$ (eV)	$C(E_g^L)$ (eV)	$C(E_v^0)$ (eV)	$C(\Delta_0)$ (eV)
AlAsAlSb	0.84	0.28	0.28	-1.71	0.15
AlPAlSb	3.56	2.7	2.7		
AlPAlAs	0.22	0.22	0.22		
GaAsGaSb	1.43	1.2	1.2	-1.06	0.6
GaPGaSb	2.558	2.7	2.7		
GaPGaAs	0.19	0.24	0.16		
InAsInSb	0.67	0.6	0.6		1.2
InPInSb	1.9	1.9	1.9		0.75
InPInAs	0.1	0.27	0.27		0.16
AlPGaP	0	0.13			
AlPInP	-0.48	0.38			-0.19
GaPInP	0.65	0.2	1.03		
AlAsGaAs	-0.127+1.31x	0.55			
AlAsInAs	0.7			-0.64	0.15
GaAsInAs	0.477	1.4	0.33	-0.38	0.15
AlSbGaSb	-0.044+1.22x				0.3
AlSbInSb	0.43				0.25
GaSbInSb	0.415	0.33	0.4		0.1

Table 5: Bowing parameters in eV, at room temperature (source: [68])

Sources for tables: [68], [19], [43], [88], [89], [90]

1 Context of the work: optical phased arrays

1.1 What are optical phased arrays and semiconductor optical amplifiers?

The Optical Phased Array (OPA) is a type of Photonic Integrated Circuit (PIC). The PIC is a family of devices that accomplish by themselves optoelectronic functions. Some aim at reproducing properties already achieved by the standard classical electronic integrated circuits, while others offer new functionalities, which is the case for OPAs.

The main components of OPA are illustrated in the left of fig. 1. From the source to the emitting end, we have in order:

- A laser diode that is the light source of the device. It has to be spatially coherent (point source emitting into long distance) and temporally coherent (monochromatic) for the device to work properly. Although such ideal and theoretical sources do not exist in reality, lasers characteristics are close enough.
- Waveguides that are made of media that allow directional propagation of light at long distance. These are passive media, meaning that they do not alter the properties of the propagating light, except for the absorption of part of it.
- Couplers, also called splitters, divide the light propagating in one waveguide into multiple waveguides, while preserving the optical properties.
- Phase shifters modify the phase of the light inside each waveguide independently. They are is the central and key components of the OPA, since the difference in phase between the light in each waveguide at the output results in the change of the laser's direction as depicted by the right diagram of fig. 1. The phase shifters allow to adjust the angle of the light plane without mechanical parts and this confers to the OPA its primary attractive property.
- A number of Semiconductor Optical Amplifiers that increase the power of light source and output. While some applications of OPA does not require SOA, increasing the intensity of light is necessary in others. SOA is the research topic of the present work.

Fig. 1 represents the OPA as a 1D array for sake of simplicity. In actual OPA, a fused quartz waveguide is placed at its end and transforms the 1D array of, for instance 64 beams, into a 2D 8×8 matrix. The 2D output enables to operate the OPA with enough degrees of freedom and scan 3D spaces.

The object of the research documented herein is the SOA. Although the SOA is not the central operational part of OPA (OPA can work without SOA), it is still a very important component and there are many applications as discussed in sect. 1.3 that require strong OPA output signals to work properly.

1.2 Beam-steering methods

The OPA is primarily used as a type of beam steering device that finds many applications such as in autonomous driving (using LiDAR), augmented and virtual reality, optical coherence tomography, weather and soil observation, etc.

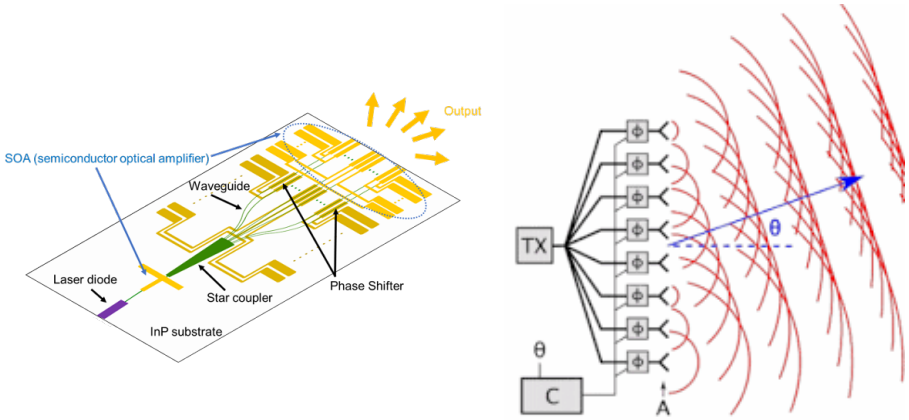

Figure 1: Left: Diagram illustrating the main components of an OPA. Electrodes are not represented here, but are necessary to drive the laser diode, the phase shifters and SOA, whose properties can be altered by current injection. Source: [1]
Right: Schematic figure illustrating the wavefront of the light at the output of the OPA. The ends of every waveguides act as several point sources and interference between them results in a linear wavefront. Dephasing of light between each waveguide allows the operator to control the direction of the output light. Source: Wikipedia.

These are the three major types of beam steering devices that are commonly used for these applications :

- A **mirror rotation** beam-steering device illustrated by the left diagram of fig. 2, includes multiple lasers at different angles that are pointed towards a rotating mirror which reflects light to the subject environment. As the mirror is rotating, the reflected light changes direction and gradually scans through the environment. The sum of the returning signals allows a 3D mapping.
- A **micro electro-mechanical systems (MEMS)** of right part of fig. 2 consists of a single laser pointing on a mirror which tangential and saggital angles are electronically controlled. Only one mirror and one laser is needed to scan through the entire 3D space.
- **Optical phased array (OPA)** : As mentioned above, an OPA has no mirror at all and does not need mechanical movements to control the beam direction.

The OPA offers many advantages over mechanical beam steering methods that motivates its wide use today. While traditional beam steering devices require mechanical movements, the OPA only uses electronic control signal, making it the best choice with respect to the five following criteria : steering speed, size, cost, energy efficiency and robustness.

1. First, OPA exceeds other methods in its operating **speed**. While the steering speed of the OPA is directly proportional to the modulation of an electronic signal, the other two technologies are hampered by much lower mechanical rotations.
2. The second criterion is **size**. MEMS and OPA are integrated on small chips and consequently extremely compact. Mirror rotation beam steering on the other hand requires a significantly large mirror, as well as a motor.
3. The third criterion is the **energy efficiency**. A large proportion of energy is lost due to friction (and kynetic energy) for devices with mechanical movements. The thermal energy loss of OPA is considerably smaller in comparison.

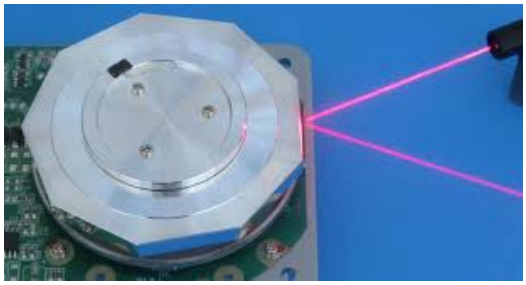
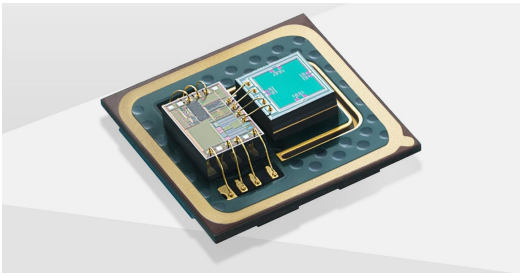

Figure 2: Left: Picture of polygon mirror type beam scanner. Source: precisionlaserscanning.com
Right: Picture of MEMS beam steering device. Source: mccourier.com

4. OPA has lower **material cost**. Even though the growing process of semiconductor is expensive, the OPA is still cheaper because of its size. Additionally, producing good quality mirrors is also expensive to begin with.

5. At last, OPA are **robust**. In most applications, beam steering devices are mounted to mobile systems that are subject to shocks and therefore must be resilient. Since the OPA is grown on a single chip and has no moving parts, shocks do not affect its function at all. Concerning the two other devices however, as the mirror and the laser are separate parts, their relative position may move due to shocks, making them vulnerable.

1.3 Application and advantages of OPA at 1μm

Event though 1.55μm wavelength OPA are more widely studied because of their applications mostly in telecommunication, 1μm wavelength exhibits some different characteristics that make their development interesting and useful. OPA at 1μm presents three major advantages compared to other wavelength: precision, water absorption, solar noise and detector cost.

First, having shorter wavelength means more precision. This is widely known because it is a common property for all types of electromagnetic waves, including radars. It is said that measurement precision is approximately equal to the wavelength. Therefore 1μm wavelength permits the detection of 1μm-sized object. For example, as red cells, the smallest cells in human beings, have a thickness of about 1μm, their accurate detection requires 1μm wavelength.

Second, the absorption spectra of water is lower in the 1μm wavelength band, as shown in fig 3. The majority of applications of OPA require sending and receiving signal through some medium. In the case of optical coherence tomography, light will have to go through organic tissues to detect anomalies. The presence of water particles will hamper the detection for 1.55μm wavelength light because of high absorption, while much less for 1μm.

Third, the solar spectrum around 1μm is low, translating in a low background noise for such wavelengths as depicted in fig. 3. This characteristic is valuable for applications pertaining to signal detection in outside environment. For example LIDARs mounted on self-driving cars detect objects that are under sun lighting. Reduced noise induces higher detection reliability, therefore increasing safety for the LIDAR.

At last, silicon detectors have higher sensitivity near 1μm wavelength than 1.55μm. Although the production cost of emitters (the OPA) is often discussed, the cost of receivers (the photo-detectors) is also important and can not be neglected in the total cost of a system. Si photo-detectors are one of the

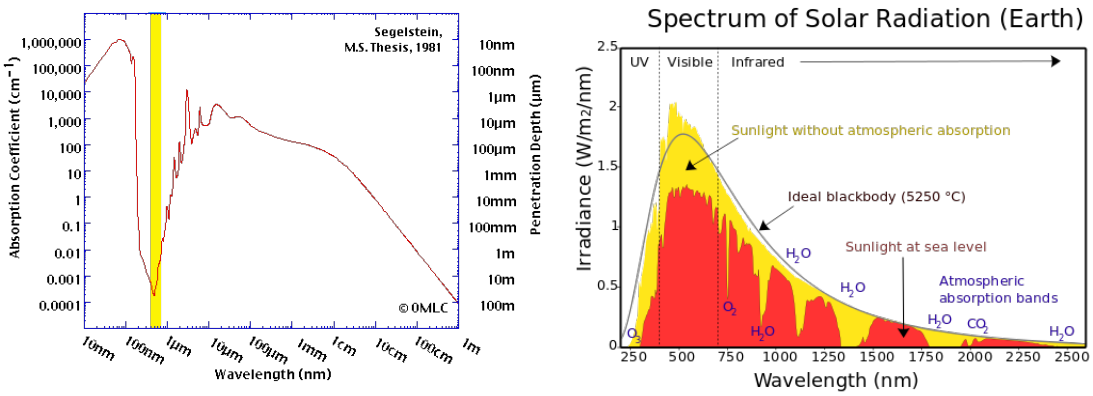

Figure 3: Left: Absorption spectra of light by water: The absorption coefficient of light by water expressed in cm^{-1} is the lowest at wavelengths between 0.2 and 1μm. Source: omlc.org
Right: Sunlight spectrum in space and at earth's surface: The solar spectrum at the earth's surface reaches a local minimum at around 950nm. This is due to the absorption and reflection of light by particles in the atmosphere. Source: e-education.psu.edu

cheapest currently available and as shown in fig.4, their sensitivity around 1μm is greater. High sensitivity is required for reliable detection. While 1.55μm wavelength OPA require more expensive sensors made with III-V compound semiconductors, it is possible to use cheaper Si detectors in combination with 1μm OPA.

1.4 Current state of research on 1μm OPA and SOA

There are currently only a few research results and papers about OPA at 1μm since it is a relatively new technology despite of its interesting and potentially wide scope of applications. While it shares the same physical principles than OPA at other wavelengths, especially those at 1.55μm, it is not possible to apply their structures directly to 1μm OPA because of fundamental reasons we will discuss later.

Some papers in the literature reports successful production of OPA at 1μm (c.f. for instance [3] and [4]). While they are perfect for primary use, they contain aluminum compounds that are very easily oxidized during fabrication (namely during the etching process) and this can affect the properties of actual fabricated devices. Therefore, it is impossible to integrate large number of arrays in OPA when aluminum is used, whereas increasing the number of arrays would increase the size of the output matrix and give the OPA a higher maneuverability, detection accuracy and scanning speed. **As there are many advantages for multiplying the number of arrays, removing aluminum from OPA design is key and motivates the object of the present research work.**
As research about SOA at 1μm without Aluminum is non existent, this work offers a first tentative to design such a device on GaAs substrate. Now, semiconductor lasers working at 1μm wavelength are widely developed and documented and can be a source of inspiration for the conception of an SOA. This is particularly valid because lasers and SOA are light amplifying medium alike, that are both based on current injection, carrier inversion and stimulated emissions.

Yet, the purpose of both devices are fundamentally different and so must be the targeted criteria for their engineering. On one hand, the laser's structure design focuses on lowering the threshold current (at which the laser start lasing) and increasing the bandwidth (increasing the reaction speed of the laser). On the other hand, the SOA's structure design must focus on increasing the output saturation gain at

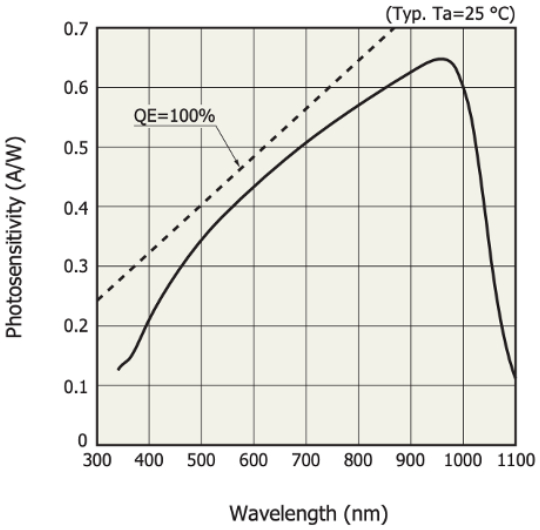

Figure 4: Si sensor sensitivity at short wavelengths. The sensitivity reaches its maximum between 950 and 1000nm. High detection sensitivity is crucial for reliable and precise detection, increasing the overall performance of the system from light beam emission to detection. Source: Hamamatsu Photonics K.K.

which the signal becomes saturated. This will at the same time allow larger amplification and prevent the destruction of the information contained in the incoming signal. In effect, the original information is modified when the SOA of some waveguides has saturated while others have not and this should be avoided at all cost.

The reason why the laser and SOA focuses on different properties comes from the fundamental differences of their overall structures: The laser is the light source itself with a structure surrounded by cavities and mirrors meant to create lasing resonance, The SOA is a mere amplifying medium that receives a signal coming from outside, must amplify it without distortion and often has antireflection coating at its edges to have uniform amplification.

Various laser structures at 1μm are studied and simulated in section 7 to compare their material gain spectra, their differential gain at maximum gain and their saturation power in the search for an appropriate candidate for the SOA. With these structures as a starting point and highlighting which parameters can be engineered to achieve desired properties, sect. 7 proposes a new structure for an Al-free SOA operating at 1μm and compares it with an Aluminum-based equivalent.

1.5 Objective and content of the research

As aforementioned, the objective of the research is to study and propose a design of Al-Free GaAs-based 1μm semiconductor optical amplifier. Now, before starting with the design of SOA, it is important to precisely understand what are the physical phenomena at work in optoelectronics. Therefore, parts of this dissertation provide a description of the fundamental physics involved, with detailed derivations when necessary to facilitate the reading (or the programming in Python). Besides, because programming numerical algorithms is a very good way to deepen one's understanding in practice, we have implemented most of the physical model equations in Python, a language that we chose because of its widespread use. **We hope that this document together with the code would be useful for future students or for teaching purpose. The advantages of a Python library for simulations are exposed in sect. 8.1.** The last part consists in using the Python library to simulate the properties of several active region structures. From these results, we conclude the research and this document by proposing a new structure for 1μm SOA.
The document is structured as follows:

Section 1 described the actual context of this work. The OPA finds many applications that require amplification, making the role of the SOA important. Besides, light at 1μm exhibits several advantageous characteristics that other wavelengths do not have. Aluminum-free SOA operating at 1μm is therefore thought to be useful for industrial purposes.

Section 2 gives a brief introduction to the basic working principles of semiconductor optical active regions and to the macroscopic dynamics of carriers and photons in active semiconductors, modeled by their rate equations. It also gives a derivation of the output saturation power which is a key metric for SOA.

Section 3 describes the physical phenomena participating to the behavior of SOA from models of the nanoscopic many-body problem of electrons in crystals to the derivation of the material gain. **Section 3.4 derives the expression of the material photonic gain by establishing the relationship between the time-derivatives of probabilities of states of a particle given by the Fermi Golden rule and the derivatives along the propagation axis of the density of photons in the device.**

To compute the material gain, we need to know how many states, characterized by energy and spin, are possibly available in the bands for transition. This is given by the density of states. Besides, carriers in a crystal occupy states by obeying to the Fermi statistics, with an occupation probability density function with two parameters: the Fermi level and temperature. The expression of carrier densities is required to infer the quasi Fermi levels from the density of carriers that are pumped into the device. The resulting occupation probabilities are used in the calculation of the gain of a SOA. **Sections 4 and 4.6 provide detailed derivations and expressions of the densities of states and of transition pairs, as a help or documentation to read the Python code.**

For the simulation of single or multiple quantum well SOA, we need numerical methods to solve the Schrödinger equation of the one-electron Hamiltonian in crystal. **Section 5** begins by solving the Schrodinger equations of ideal and simple potential wells. These are classical exercises of textbooks on quantum mechanics but are necessary for the understanding of more complex structures. It ends with **sect. 5.6 proposes a novel derivation and formulation of the Eigen-energies of a particle in a three-dimension multi-layer structure with heterogeneous effective masses, by first and second order perturbation.** Solutions are obtained by standard resolution of the finite-dimension linear system obtained by discretization and finite-difference method.

Whereas sect. 3 gives the theoretical expression of the gain, **Section 6 describes the step-by-step procedures for its computation in practice on three examples and validates the Python code and its underlying equations by replicating charts of gain spectrum from [19] for bulk and quantum wells. It ends with the explanation of the algorithm for the most complex multiple quantum well structures.**

With the aim to design a device well-suited for operation at 1μm, **section 7 addresses the desired properties of the device and the parameters to engineer the appropriate band-gap**. With a step-by-step approach, it demonstrates that InGaAs is the only appropriate material for the well while this is also supported by articles in the literature, and analyses the impact of the material chosen for barriers on the characteristics of the gain. It concludes with a proposal of a single quantum well and opens some questions for further work.

Finally, **the Python code is briefly documented in section 8 with a short user guide**.

2 Macroscopic dynamics of SOA

2.1 Working principles of semiconductor optical active regions

Semiconductor optical active regions of lasers or SOA make use of the electromagnetic field of light beams to stimulate transitions of electrons between the conduction and valence bands of an *active* material. The material is chosen so that its band-gap E_g corresponds more or less to the maximum light wavelength range of interest.
The electric field of the light modifies the Hamiltonian of electrons in such a way that the projection of the superposition state of electrons on Eigen-states is evolving quickly over time. The probability of an electron to move from a state of energy E to a state of energy $E \pm h\nu$ is driven by the incoming photons of energy $h\nu$.

2.1.1 Carrier transitions

In equilibrium conditions with no power supply, the valence band of a semiconductor crystal is the highest energy band that is partially filled with electrons, while there are no electron in the conduction band as depicted in fig. 11. When an electron at the bottom the conduction band transits to the top of the valence band, it releases energy E_g in the form of the emission of a photon with an energy $h\nu$. Therefore, in order to produce light, carriers (electrons in the conduction band or holes in the valence band) have to be injected resulting in an inversion of the population of the bands. This is done by supplying energy in the form of either heat, incoming light or vacuum electromagnetic field or by applying a voltage across a double heterostructure PN junction.
Note that electrons in bands of energy lower than that of the valence band are not of interest because either, they are too close and tightly bonded to their nuclei, or their transition will release photon at wavelengths that are outside of the spectrum of interest.
Several types of electronic transitions occur in the active crystal as illustrated in fig. 5:

1. Spontaneous emission: This is the emission of a photon by the transition of an electron to the valence band.

2. Stimulated absorption: The energy of a radiating photon is absorbed by the transition of an electron from the valence band to the conduction band, leaving a hole in the valence band.

3. Stimulated emission: An incoming photon induces a recombination of an electron and the emission of second photon.

4. Recombinations that are nonradiative because they do not result in the absorption or emission of photons. They are of two types:

   (a) Auger recombination where the energy released is transfered to a carrier as a kinetic energy instead of emitting a photon.

   (b) Recombination due to imperfections in the crystal or at its surface and interface with barriers.

Because of transitions, the carrier density N in m^{-3} will evolve along the direction of light propagation at a total rate $\frac{dN}{dt}$ expressed in $\mathrm{m}^{-3}\mathrm{s}^{-1}$.
The rates of the above transitions are respectively noted R_{sp}, R_{12}, R_{21} and R_{nr} and the total rate of stimulated transitions is defined as

$$R_{st} = R_{21} - R_{12}$$

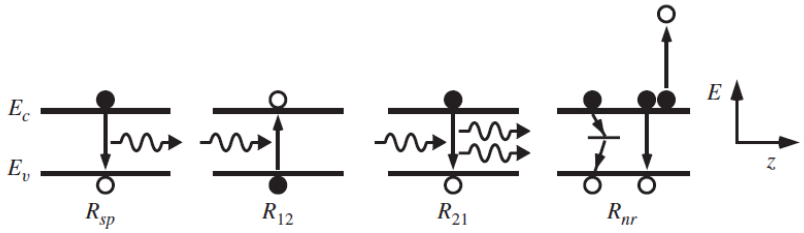

Figure 5: Electronic transitions between the conduction and valence bands. The first three represent radiative transitions in which the energy to free or bind an electron is supplied by or given to a photon. The fourth illustrates two nonradiative processes. Source: [19]

2.1.2 Confinement of carriers and photons in a well

Fig. 6 shows a simple PIN structure of a double heterostruture of a laser diode. Despite its simple design, it is very effective at creating two important characteristics for the purpose of controlling the interaction between carriers and photons:

- Because the crystal of the p and n barriers have a higher energy gap E_{gcl} than the gap E_g in the active intrinsic region layer, the active region forms two potential wells: One with a positive potential barrier for negatively-charged electrons, one with a negative barrier for the positively-charged holes. As a result, carriers created by absorption of photons or by current injection are mostly confined in the active region, increasing their probability of interaction. When a voltage is applied to the pin, holes (positively charged carrier) will flow from the p layer into the valence band of the active region), while electrons from the n layer will fill the conduction band.

- In order to maximize the interaction between photons and carriers, the electromagnetic field of the light inside the well is also confined thanks to the difference of refractive indices between the active region and the barriers. Consequently, the magnitude of the electric field of the light is at its maximum in the middle of the well.

Fig. 7 represents the same PIN structure in 3D. The notations used in the diagram will be applied throughout the document. In particular, the wave propagation is along the z axis and the well width is along the x axis.

2.2 Actual structure of SOA

The general layout of an SOA is depicted in fig. 8. It is very similar to that of semiconductor diode lasers, which is expected since they both are light amplifying devices. The major difference is the presence of mirrors for the laser well, while SOA often have anti-reflection coating at each end.

The structure is grown on a material called the substrate by using various fabrication methods like the Metal-Organic Vapor Phase Epitaxy (MOVPE, also called MOCVD) or the Molecular Beam Epitaxy (MBE). Each fabrication technology has its pros and cons that are subject to extensive research works that we will not discuss in this document.

In order to control the carrier density inside the active region, the SOA is typically built as the PIN junction described in the prior section. In most structures, n-doped regions are fabricated at the bottom of the well just above the substrate, while p-doped regions are inserted at the top. They are called cladding regions. The confinement of carriers enables positive gain inside the active region. It is desirable to have

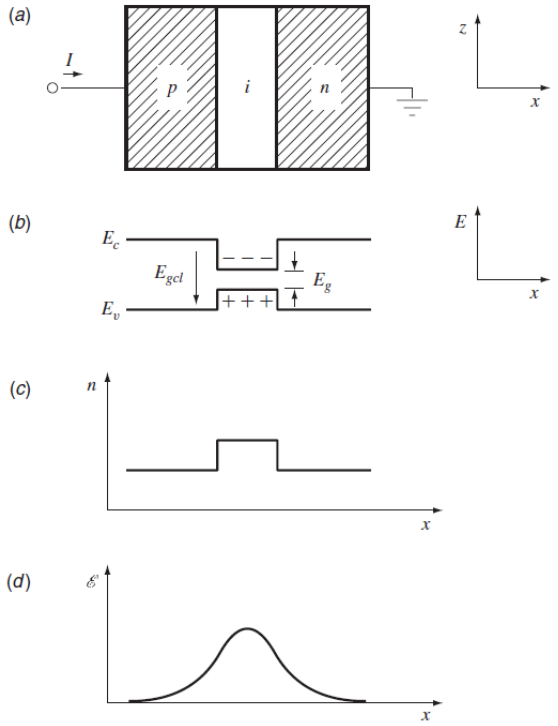

Figure 6: Aspects of the double-heterostructure diode laser: (a) a schematic of the material structure; (b) an energy diagram o the conduction and valence bands vs. transverse distance; (c) the refractive index profile; and (d) the electric field profile for a mode traveling in the z -direction. Source: [19]

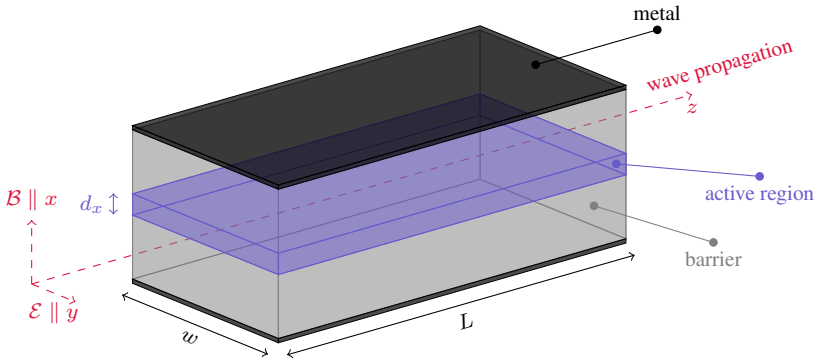

Figure 7: GaAs quantum well SOA with Transverse Electric (TE) field: A GaAs active region of a few nanometers thickness is sandwiched between the P and N barrier layers made of GaAs dopped by aluminum, creating a PIN (P type/Intrinsic/N type) diode.

the active region inside the intrinsic region of the PIN junction. Since the intrinsic region has no free carriers at equilibrium, creating carriers requires less current injection and allows full control of the gain of the structure. The active region is most often designed as either a single well or as a multiple quantum

wells, but other shapes exist such as bulks, quantum wires or quantum dots. The active region is where carriers will be concentrated and the overall structure of the SOA must be engineered so that the light electromagnetic field overlaps with the active region as much as possible as illustrated by fig. 9.

The electrodes are made of conductive material, typically gold or copper, and are used to apply voltage and inject current into the active region of the SOA. They are in contact with the n and p-doped claddings. The contact zone is narrowed by adding insulators (mostly oxides) to help confining carriers. Carefully restricting areas of charge carriers into the active zone maximizes their interaction with the incident light and achieve a better gain efficiency while keeping a low injection current requirement.

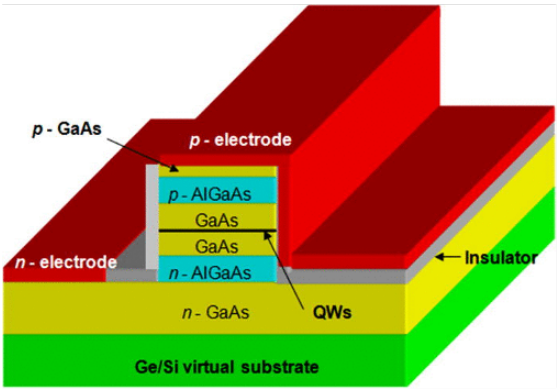

Figure 8: Schematic of an example of an amplifying medium (laser in this case) using Aluminum. Source: [2]

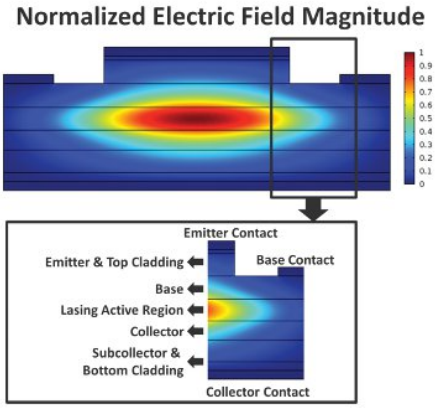

Figure 9: Cross-section of SOA and profile of the electric field of the light beam. For a good efficiency, the SOA must be designed in such a way that most of the light is confined in the active region where stimulated emissions at the right wavelength can occur. Source: compoundsemiconductor.net

2.3 Rate equations

We will see in sect. 3.4 how to compute the net material gain g born by stimulated emission and absorption. The material gain is related the stimulated rate R_{st} as

$$R_{st} = g v_g N_p$$

where N_p is the photon density (assumed to be uniform over x and y) and v_g is the group velocity. If there were no loss of current or carriers, a perfect confinement of photons and no other radiative or non-radiative phenomena, the total gain over the length of the SOA would be simply e^{gL}. However, there are many other sources of photon rates. Besides, we have to remember that the gain g is in fact a function of the carrier density N and that the carriers will be used concurrently by all types of transitions. Therefore, it is not possible to know the gain of the entire device without taking into account of all these phenomena that occur at the same time.
This section first provides the general and simplified expressions for the carrier rate equation and the photon rate equation.
There are many different models ([100], [97], [93], [76] among others) for the rate equations in the literature. Some introduce a better description of various losses. Others define a specific carrier rate equation in each of the wells in MQW structures and in each of the SCH layers. We end this section by a short description of one of such models, for a SQW with partially refractive input and output facets.
For all these models, there is a set of several ordinary differential equations that are coupled, that is, they can not be solved independently one from each others, because they share common terms related to the carrier density. Specific numerical procedures must be designed and implemented for each model.
This is out of the scope of the present work as we only focused on material gain and saturation.

2.3.1 Carrier rate equation

The carrier rate equation describes the density of charge carriers at any time t and position z. For any period dt, it assesses the carriers that are created and lost as follows:

$$\frac{dN}{dt} = G_{gen} - R_{loss}$$

where N is the carrier density in m^{-3}.
G_{gen} is the generation rate of carriers per unit volume defined in $\mathrm{m}^{-3}\mathrm{s}^{-1}$. Since all of the generation is made through injection, we simply have:

$$G_{gen} = \frac{\eta_i I}{qV}$$

where η_i is the injection efficiency, I the injection current, q the fundamental charge of an electron, and V the volume of the active region.
R_{loss} is the loss rate per unit volume. Electrons are largely lost due to various types of recombination. The rate of loss can be expressed as the sum:

$$R_{loss} = R_{st} + R_{sp} + R_{nr} + R_l$$

where R_{st} is the net recombination rate by stimulated emission and absorption, R_{sp} is the rate of spontaneous emission, R_{nr} is from non radiative emissions and R_l is by carrier leakage. To be noted is that carrier leakage is the only term that is not a recombination, but a loss due to insufficient confinement of carriers.

We should focus upon R_{st} since it is through the net stimulated emission that gain occurs in an amplifying medium. Combining other loss rates as a single term, we obtain:

$$R_{loss} = R_{st} + \frac{N}{\tau}$$

where

$$\frac{1}{\tau} = A + BN + CN^2$$

and τ is homogeneous to a lifetime that is typically of a few ps.
A, B, C are coefficients that are respectively related to carrier leakage, spontaneous emission, and Auger recombination. These are carriers that are not useful to amplify the light (except for spontaneous emission B, where a very small fraction will contribute).

As the purpose of the carrier rate equation is to relate the carrier density N with the current injection I and the stimulated emission, the final expression of the carrier rate equation is written as

$$\frac{dN}{dt} = \frac{\eta_i I}{qV} - R_{st} - \frac{N}{\tau} \tag{2.1}$$

2.3.2 Photon rate equation

In the same manner as the carrier rate equation, the photon rate equation estimates photons created and lost during a period dt. As such we have

$$\frac{dN_p}{dt} = N_{p,gen} - N_{p,loss}$$

All photons generated in the active medium **in the wanted optical mode** are due to net stimulated emission. Few are also generated by spontaneous emission, that are luckily in the wanted mode. The photon generation rate is therefore

$$N_{p,gen} = \Gamma R_{st} + \Gamma \beta_{sp} R_{sp}$$

where β_{sp} is the spontaneous emission factor which is of the order of 10^{-4}. Since the carrier rate equation is defined in a volume V_a of the active region, while the photon rate equation defined in a volume V_p of the light surface, we introduce the confinement factor Γ defined as:

$$\Gamma \equiv \frac{V_a}{V_p}$$

There are several factors for optical loss such as absorption and scattering, but we will not look into the details and analogically to the carrier rate equation, set

$$N_{p,loss} = \frac{N_p}{\tau_p}$$

where τ_p is a photon lifetime that includes all sorts of material losses.
The final form of the photon rate equation is therefore:

$$\frac{dN_p}{dt} = \Gamma R_{st} + \Gamma \beta_{sp} R_{sp} - \frac{N_p}{\tau_p} \tag{2.2}$$

2.3.3 Description of carrier rate equation models

Connelly's model [76] defines the incoming signal as the sum of N_s signals of different frequencies ν_k (N_s can be set to one to simulate a single signal). This is interesting because multiple signals will each stimulate emissions and therefore commonly use the carriers pumped into the conduction bands. Therefore, the action of the SOA in presence of multiple inputs is not the sum of its action on individual input taken separately.
The model assumes facets at input and output are partially reflective. As a result, parts of the stimulated emissions will be reflected and travel back to the input where they are also are partially reflected and so forth.
Because of the reflecting facets, spontaneous emission noise experiences resonance and only N_m frequencies at various longitudinal well modes are taken into account, forward and backward. As the well resonance is born by a filtering action of the well, the modulus of the spontaneous rates is adjusted by a single-pass filter-gain.
This leads to $2(N_s + N_m)$ photon rate equations that are only function of z and not of t, for a density of carriers $n(z)$ given. The equations are only coupled by $n(z)$ and can be solved independently for a given profile of $n(z)$.
The carrier rate equation takes into account carrier injection by current and losses as usual, as well as the consumption or creation of carriers by the $2(N_s + N_m)$ stimulated and spontaneous emission and absorption. The equation depends on time as it defines $\frac{dn(z)}{dt}$ but the model solves for the steady-state regime with $\frac{dn(z)}{dt} = 0$. Given an initial profile of discretized $n(z)$, the model numerically solves for the photon rates and injects them back in the carrier equation. If the carrier steady-state condition is not satisfied, the $n(z)$ are adjusted by fixed proportional decrements or increments [1] and photon rates are recomputed. The method converges after a few iterations.

2.4 Optical saturation power

The ideal total gain expression e^{gL} also assumes that the material will be able to provide sufficient carriers to maintain the same gain even if the incoming optical power were very large. This is obviously physically impossible because the crystal can only provide a limited numbers of carriers. This is when a saturation effect occurs. The derivation here is following sect 8.2.5 of [19] on SOA, but provides more details.

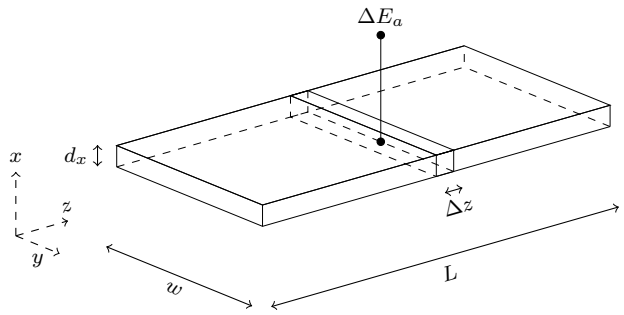

Figure 10: Energy ΔE_a at time t in the volume of length Δz of the active region of the SOA of fig. 7

Fig. 10 represents a slice of length Δz of the active region. The amount of photon energy contained in this tranche is simply given as the number of photons $N_p v_a$ times the energy per photon $h\nu$, where v_a

[1] It should be possible to adjust the numerical procedure and implement a gradient descent that may be more efficient.

is the small volume of the active region $v_a = d_x w \Delta z$ and N_P is the photon density. Hence we have:

$$\Delta E_a = N_p d_x w \Delta z h\nu$$

Considering that not all photons are confined in the active region, this corresponds to a larger total photon energy ΔE, including outside the active region, of:

$$\Delta E = N_p \frac{d_x w}{\Gamma_{\text{xy}}} \Delta z h\nu$$

where $\Gamma_{\text{xy}} \leq 1$ is the confinement factor.
Noting d_x by d for sake of ease, this can be rewritten as

$$\frac{\Delta E}{\Delta t} \frac{\Delta t}{\Delta z} = N_p \frac{dw}{\Gamma_{\text{xy}}} h\nu$$

Noting that $\frac{\Delta E}{\Delta t}$ is the optical power of the light beam $P(z)$ and $\frac{\Delta z}{\Delta t}$ is the group velocity v_g, it gives

$$P(z) = v_g N_p \frac{dw}{\Gamma_{\text{xy}}} h\nu$$

or

$$v_g N_p = \frac{P\Gamma_{\text{xy}}}{dwh\nu}$$

In the carrier rate eq. 2.1, the stimulated recombination rate R_{st} is given as

$$R_{st} = g v_g N_P$$

Therefore, the rate equation can be rewritten from

$$\frac{dN}{dt} = \frac{\eta_i I}{qV} - R_{st} - \frac{N}{\tau} \tag{2.3}$$

to

$$\frac{dN}{dt} = \frac{\eta_i I}{qV} - g\frac{P\Gamma_{xy}}{wdh\nu} - \frac{N}{\tau} \tag{2.4}$$

To compute the saturation power in a simple manner, the gain is often approximated as a linear function of the carrier density N

$$g = a\left(N - N_{\text{th}}\right) \tag{2.5}$$

where a is the differential gain (or the slope of the line equation).
At steady-state with $\frac{dN}{dt} = 0$ and when the optical power is low, P can be neglected and eq. 2.6 becomes:

$$\frac{\eta_i I}{qV} - \frac{N}{\tau} = 0 \tag{2.6}$$

This yields to a carrier density N_0 and a gain g_0 at low optical power and steady-state given as

$$N_0 = \frac{\eta_i I \tau}{qV}$$
$$g_0 = a\left(N_0 - N_{\text{th}}\right)$$

This defines the carrier density when no carrier are used by incoming light and the gain g_0 that can be achieved when no photons are using available carriers. From this, the threshold density can be expressed as

$$N_{\text{th}} = \frac{\eta_i I \tau}{qV} - \frac{g_0}{a} \tag{2.7}$$

At steady state, eq. 2.6 becomes

$$\frac{\eta_i I}{qV} - g\frac{P\Gamma_{xy}}{wdh\nu} - \frac{N}{\tau} = 0 \tag{2.8}$$

therefore,

$$N = \frac{\eta_i I \tau}{qV} - g\frac{P\Gamma_{xy}\tau}{wdh\nu} \tag{2.9}$$

Injecting eq. 2.7 and 2.9 into the linear expression of the gain of eq. 2.5 gives:

$$g = a\left(\frac{\eta_i I \tau}{qV} - g\frac{P\Gamma_{xy}\tau}{wdh\nu} - \frac{\eta_i I \tau}{qV} + \frac{g_0}{a}\right) = g_0 - gP\frac{a\Gamma_{xy}\tau}{wdh\nu} = g_0 - g\frac{P}{P_s} \tag{2.10}$$

where $P_s = \frac{wdh\nu}{a\Gamma_{xy}\tau}$.
Solving for g gives

$$g = \frac{g_0}{1 + \frac{P}{P_s}} \tag{2.11}$$

Note that g and P are function of z in this equation.
The optical power amplification can be gain by the gain g as

$$\frac{dP}{dz} = P' = gP$$

Injection the expression of g yields

$$P' = g_0\frac{P}{1 + \frac{P}{P_s}}$$

Integration from 0 to z gives the expression

$$G(z) = G_0(z)e^{-\frac{G(z)-1}{G(z)}\frac{P(z)}{P_s}} \tag{2.12}$$

where $G(z) = \frac{P(z)}{P(0)}$ and $G_0(z) = e^{g_0 z}$. The above equation is not easy to derive but we can easily checked it is consistent with the ordinary differential equation above.

Proof. Eq. 2.17 develops as

$$P(z) = P(0)e^{g_0 z}e^{-\frac{P(z)-P(0)}{P_s}} \tag{2.13}$$

Deriving gives

$$P' = P\left(g_0 - \frac{P'}{P_s}\right) \tag{2.14}$$

or, moving the second term on the right to the left side of the equation

$$P'\left(1 + \frac{P}{P_s}\right) = g_0 P \tag{2.15}$$

Dividing by $\left(1+\frac{P}{P_s}\right)$ finally gives the same expression as before

$$P' = g_0 \frac{P}{1+\frac{P}{P_s}}$$

■

Finally, for $z = L$, the total gain for large signals is

$$G = G_0 e^{-\frac{G-1}{G}\frac{P(L)}{P_s}} \tag{2.16}$$

$G_0(L)$ is the unsaturated gain when the optical power at the input or at the output is significantly lower than P_s.
The saturation output power P_{o_s} is defined as the value of output power $P(L)$ such that the gain G is half of G_0. Replacing all term in G by $\frac{G_0}{2}$

$$\frac{G_0}{2} = G_0 e^{-\frac{\frac{G_0}{2}-1}{\frac{G_0}{2}}\frac{P_{os}}{P_s}} \tag{2.17}$$

Therefore

$$\frac{1}{2} = e^{-\frac{G_0-2}{G_0}\frac{P_{os}}{P_s}}$$

$$\ln 2 = \frac{G_0-2}{G_0}\frac{P_{o_s}}{P_s}$$

$$P_{o_s} = P_s \frac{G_0 \ln 2}{G_0 - 2} \tag{2.18}$$

3 Physics of semiconductor photonics

This section provides a description of the physical phenomenon that participates in the emission and absorption of photons in pumped semiconductor crystals. The purpose is to have an overall understanding without going into much details, of the mechanisms underlying the interaction of carriers (electrons and holes) with incoming light beam and of the derivation of the material gain due to stimulated transitions.
The section is organized as follows:

- The Hamiltonian of electrons and nuclei in a crystal is very complex. It can however be approximated by the Hamiltonian of a single electron subject to a periodic potential created by the ions in the crystal. This is described in sect. 3.1
- Because of the periodic structure of its lattice, electrons of a crystal can take continuous energy values in non-overlapping bands separated by forbidden energy levels. From the geometry of the crystal, it is possible to determine the shape of the bands with the energy E expressed as a function of the wave vector $\mathbf{k}$, and to determine the wave function ψ of an electron. Besides, for small values of $\mathbf{k}$, the shape of the $E - \mathbf{k}$ graph can be approximated by a parabola and carriers can be viewed as free particles with a so-called *effective* mass that is function of the band and of the material. This is discussed in sect. 3.2.
- Light is a electromagnetic wave. The electric field of a light beam propagating through the crystal perturbs the Hamiltonian of electrons. This perturbation is such that the wave functions of electrons in the conduction and valence bands overlap, stimulating transition of electrons between them as discussed in sect. 2.1.1. This is the object of sect. 3.3.
- Sect. 3.4 briefly explains how to derive the material gain of the active region from the transition rate. The actual set-by-step calculation of the gain will be addressed in sect. 6.
- At last, the calculation of the gain requires to know some material parameters that are dependent on the alloy used in the SOA. The properties of binary alloys have been well studied, measured by experiments and are available in the literature or in databases. Because there are less experimental data on ternary or quaternary alloys, their parameters must be estimated by interpolation methods. Finally, a strain will be applied on barriers and active regions because made of crystals with different lattice constants than the substrate on which they are grown. Parameters such as band gaps and effective masses must be adjusted accordingly. This is documented in sect. 3.5.

3.1 Hamiltonian of a particle in a crystal

3.1.1 Hamiltonian of a crystal: a many body problem

The Hamiltonian that describes the entire physical system of a crystal is born from the kinetic energies of all particles and their electrostatic interaction potentials and reads:

$$\mathcal{H} = \sum_i \frac{\mathbf{p}_i^2}{2m_i} + \sum_k \frac{\mathbf{P}_k^2}{2M_k} + \frac{1}{2}\sum_{k\neq l} \frac{Z_k Z_l e^2}{4\pi\varepsilon_0 |\mathbf{R}_k - \mathbf{R}_l|} - \sum_{i,k} \frac{Z_k e^2}{4\pi\varepsilon_0 |\mathbf{r}_i - \mathbf{R}_k|} + \frac{1}{2}\sum_{i\neq j} \frac{e^2}{4\pi\varepsilon_0 |\mathbf{r}_i - \mathbf{r}_j|}$$

This accounts for all electrons (indexed by i or j), with mass m_i, position vector $\mathbf{r}_i$ and momentum operator $\mathbf{p}_i$ and for all nuclei (indexed by k or l) with mass M_k, atomic number Z_k, position $\mathbf{R}_k$ and

momentum $\mathbf{P}_k$. The Schrödinger equation with this Hamiltonian is far too complex because of the huge number of nuclei and electrons and needs to be simplified. First, core electrons that are not in the valence or conduction bands are very close to nuclei and do not participate to conduction. Therefore, we can replace the nuclei in $\mathcal{H}$ by the ions formed of nuclei and core electrons. The only electrons we need to consider are those in the valence and conduction bands and this significantly reduces the number of particles in the system. Besides, the Hamiltonian can be split in three components: one related to the dynamic of electrons assuming static ions, one describing the vibration of ions, and one that expresses the influence of the movements of ions on electrons.
Here we will focus on the first part, the electronic Hamiltonian for all electrons, given as:

$$\mathcal{H}_e = \sum_i \frac{\mathbf{p}_i^2}{2m_i} - \sum_{i,k} \frac{Z_k e^2}{4\pi\varepsilon_0 |\mathbf{r}_i - \mathbf{R}_{k_0}|} + \frac{1}{2} \sum_{i \neq j} \frac{e^2}{4\pi\varepsilon_0 |\mathbf{r}_i - \mathbf{r}_j|} \tag{3.1}$$

where $\mathbf{R}_{k_0}$ are the positions of the static ions. This still is a many-body problem as the Hamiltonian involves all electrons in the valence and conduction bands and all ions. There are several numerical approaches to solve it including, to mention the main ones:

- Quantum Monte Carlo
- Density Function Theory. [61], [62], [63].
- Although not widely applied it is worth mentioning the more recent applications of machine learning, using either neural network or Boltzmann machines.

Such ab-initio methods are complex and their study or implementation is out of the scope of the present work. Instead, we will work with other methods based on further simplification.

3.1.2 One-electron Hamiltonian $\mathcal{H}_0$

Instead of solving eq. 3.1 with ab-initio methods, we can assume that any single electron is subject to the same potential $V(\mathbf{r})$ and that the stationary Schrödinger equation for one electron is written as

$$\mathcal{H}_0 \psi = \left(\frac{\mathbf{p}^2}{2m} + V(\mathbf{r}) \right) \psi = E\psi \tag{3.2}$$

$\mathcal{H}_0$, ψ and E respectively denote the Hamiltonian for one electron, the wave function and the energy of an electron in an eigenstate. $\mathbf{p}$ is the momentum operator and $\mathbf{r}$ is the position vector.
$V(\mathbf{r})$ contains the information about the presence of other electrons and ions and, in particular, the periodicity of the potential.

3.2 Energy band structure and free particle with effective mass

3.2.1 Bloch functions

As per the Bloch's theorem, solutions ψ_n of eq. 3.2 can be expressed in an infinite basis of functions $\phi_{n,k}$, called Bloch wave functions, with eigenvalue $E_{n,k}$ and given by:

$$\phi_{n,\mathbf{k}}(\mathbf{r}) = e^{i\mathbf{k}\cdot\mathbf{r}} u_n(\mathbf{k}, \mathbf{r}) \tag{3.3}$$

where $u_n(\mathbf{k}, \mathbf{r})$ are the so-called Bloch functions with the same periodicity in $\mathbf{r}$ as the crystal lattice and where $\mathbf{k}$ is the wave vector. To any given index n, called the band index, corresponds a band of continuous

energy $E_{n,\mathbf{k}}$. n designate a band here, not some discrete eigen solutions.
Because the set of $\phi_{n,\mathbf{k}}$ form a basis, any solution (in the band n) of the equation can be expressed by its continuous projection on the basis:

$$\psi_n = \int A(\mathbf{k}) e^{i\mathbf{k}\cdot\mathbf{r}} u_n(\mathbf{k}, \mathbf{r}) d\mathbf{k} \tag{3.4}$$

where $A(\mathbf{k})$ are imposed by boundary or periodicity conditions and where the integral is over three dimensions.
Following a note in [60], it is worth noting that the $\mathbf{k}$ in the equation is not such that $\hbar\mathbf{k}$ is the electron momentum. Instead it is the momentum of the crystal as a whole.

3.2.2 Energy band structures

In an isolated atom, electrons can only take discrete energy levels, each with a corresponding wave function. Table 6 shows the atomic structure of usual elements of semiconductors. As underlined by the curly braces, the outermost valence electrons are either in the s-type or p-type orbital.

When P atoms are close, the interaction of the Hamiltonians born for each of the atoms is such that one original energy levels of a single atom are split into P levels spaced symmetrically around their original values.

In semiconductor solids, for a large number of atoms, equally spaced in the crystal by the lattice distance a, each discrete energy level is transformed into a band of energy. For instance and in an ideal simplified one-dimension case, the Eigen-energy of an electron in the first band can take a continuum of values that can be approximated by a cosine of the momentum k of period $\frac{2\pi}{a}$:

$$E = E_1 + \Delta E_1 \cos ka$$

This is assuming that the wave function of an atom is only influenced by its near two neighbors. In reality the band width is not a pure cosine.
To summarize, the periodicity of the lattice on the crystal is such that the solutions of the Schrödinger equation have energies that can take values in bands as illustrated in fig. 11 and already hinted in sect. 3.2.1. Bands are due to the interaction of wave functions of neighbor atoms when the dimensions of the crystal are very large compared with the lattice constant a. This creates a periodicity of the energy versus the wave vector $\mathbf{k}$ as shown in fig. 12.
The only bands of interest in semiconductors are typically the conduction (C), heavy hole (HH), light hole (LH), and split-off (SO) bands ([58]). Each of these four bands has two spin components, so there are altogether eight bands. As discussed in [59], electrons in valence and conduction bands retain their p-type and s-type properties. The light and heavy holes bands are anisotropic, while the spin-orbit split-off band is isotropic.
More explanations on the calculation on bands can be found in [52], [59], [58], [53], [54], [55], [60] and [56].

3.2.3 Parabolic $E - \mathbf{k}$ and effective mass

The energy of a free particle of mass m in an infinite space of zero potential [2] is equal to its kinetic energy $E = \frac{\mathbf{p}^2}{2m}$. As $\mathbf{k} = \frac{\mathbf{p}}{\hbar}$, the energy is a parabolic function of $\mathbf{k}$:

$$E = \frac{\hbar^2}{2m}\mathbf{k}^2$$

[2] The potential can be 0 everywhere or constant everywhere. This is only a matter of definition of the origin of the energy scale.

IV Semiconductors

C	$1s^2\,\underbrace{2s^2 2p^2}$
Si	$1s^2 2s^2 2p^6\,\underbrace{3s^2 3p^2}$
Ge	$1s^2 2s^2 2p^6 3s^2 3p^6 3d^{10}\,\underbrace{4s^2 4p^2}$

III-V Semiconductors

Ga	$1s^2 2s^2 2p^6 3s^2 3p^6 3d^{10}\,\underbrace{4s^2 4p^1}$
As	$1s^2 2s^2 2p^6 3s^2 3p^6 3d^{10}\,\underbrace{4s^2 4p^3}$

Table 6: Atomic structures of common elements in semiconductors. Electrons in the valence bands are underlined by curly brackets. Core electrons in filled band below the valence band are not of interest.

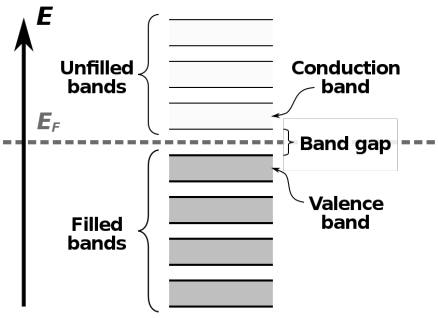

Figure 11: Energy bands in a semiconductor crystal. The valence band is the filled band of highest energy. The conduction band is unfilled in absence of carrier injection. (Source: Wikipedia)

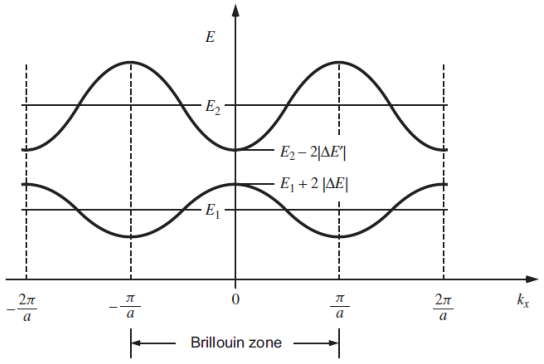

Figure 12: Energy bands created by a periodic series of atoms in one dimension. Two bands resulting from two original discrete atomic states are shown. Source: [19]

For energy bands, the function $E(\mathbf{k})$ can be approximated by a parabola for $\mathbf{k} \approx 0$, near the top of the valence band and bottom of the conduction band of fig. 12. Indeed, if $\frac{d^2E}{dk^2}$ is nearly constant for $\mathbf{k} \approx 0$, E can be written as

$$E = \frac{1}{2}\frac{d^2E}{dk^2}\mathbf{k}^2$$

plus a constant. Defining m^* as

$$\frac{\hbar^2}{2m^*} = \pm\frac{1}{2}\frac{d^2E}{dk^2}$$

The energy parabolic approximation becomes

$$E = \pm\frac{\hbar^2}{2m^*}\mathbf{k}^2$$

The sign depends on the orientation of the parabola.
As a result, an electron in a crystal at small modulus of $\mathbf{k}$ behaves like a free electron in a region of uniform potential, but with an **effective mass** m^* that is dependent of the material. m^* is usually given as

fraction of the actual electron mass m_0. For instance, for GaAs, an electron in the conduction band bears an effective mass $m^* = 0.067 \times m_0$.
Therefore, an electron in the conduction band behaves as a particle of mass m^* in a well built by the difference of bandgaps between the active region and its barriers.

At the bottom of the conduction band, the energy band reads:

$$E = E_c + \frac{\hbar^2 k^2}{2m_c} \quad \text{or} \quad E - E_c = \frac{\hbar^2 k^2}{2m_c}$$

where m_c is the effective mass of the particle in the conduction band in the relevant crystal.
At the top of the valence band, the parabola is concave with:

$$E = E_v - \frac{\hbar^2 k^2}{2m_v} \quad \text{or} \quad E_v - E = \frac{\hbar^2 k^2}{2m_v}$$

where m_v is the effective in the relevant valence band (heavy hole, light hole) for the relevant crystal.

3.2.4 Wave function of electrons

With some approximations (see [19] for details), eq. 3.4 becomes, with the indices 1 or v and 2 or c denoting the valence and conduction bands:

$$\psi_1(\mathbf{r}) = F_1(\mathbf{r})u_v(\mathbf{r}) \quad \text{and} \quad \psi_2(\mathbf{r}) = F_2(\mathbf{r})u_c(\mathbf{r}) \tag{3.5}$$

The envelope functions $F(\mathbf{r})$ satisfy the Schrödinger equation using the macroscopic well potential illustrated by fig. 13 in a one-dimension representation. This is the potential well created by the difference of band-gap between the active region and barrier of lasers or SOA already discussed in 2.1.2. The $F(\mathbf{r})$ are slow-varying function and alike the solutions of 1D finite well equation of sect. 5.3.
u_v and u_c are the Bloch functions of the valence and conduction bands where we assumed that $u_n(\mathbf{k}, \mathbf{r})$ (with n represented by v or c) does not strongly depend on $\mathbf{k}$ and can be replaced by $u_n(\mathbf{0}, \mathbf{r})$ noted $u_n(\mathbf{r})$. As a reminder, the Bloch functions are related to the periodic nature of the potential in the lattice at the microscopic atomic level and they are consequently varying rapidly as shown in fig. 13.
Here, we do not know the shapes of the envelope and Bloch functions. They can only be determined by the actual resolution of the Schrödinger equation with the relevant conditions but we will see in sect. 3.3.3 that we only need to know some of their geometrical properties when estimating matrix transition elements.

3.3 Perturbation of the one-electron Hamiltonian by the electric field of light

3.3.1 Motion of a charged particle

The Hamiltonian of electron of charge $-q$ and of mass m_0 in an electromagnetic field is given by (c.f. [84])

$$\mathcal{H} = \frac{1}{2m_0} \left(\mathbf{p} + q\mathbf{A}(\mathbf{r}, t)\right)^2 + q\phi(\mathbf{r}, t)$$

where $\mathbf{A}$ is the magnetic vector potential (a vector field) and ϕ is the electric potential (a scalar field).
The magnetic field $\mathbf{B}$ and electric field $\mathbf{E}$ can be derived from $\mathbf{A}$ and ϕ as follows:

$$\mathbf{B} = \nabla \times \mathbf{A} \quad \text{and} \quad \mathbf{E} = -\nabla\phi - \frac{\partial \mathbf{A}}{\partial t}$$

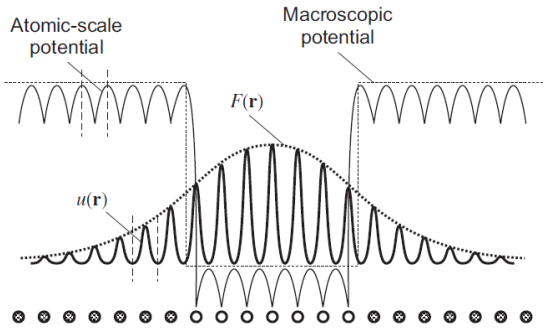

Figure 13: Illustration of a quantum-well potential and the corresponding lowest energy electron wave function. Source: [19]

With $\Lambda(\mathbf{r}, t)$ an arbitrary scalar function, the gauge transformation

$$\mathbf{A} \rightarrow \mathbf{A}' = \mathbf{A} + \nabla\Lambda \quad \text{and} \quad \phi \rightarrow \phi' = \phi - \frac{\partial\Lambda}{\partial t}$$

leads to the same magnetic and electric fields. If we choose Λ s.t. $\phi = \frac{\partial\Lambda}{\partial t}$, i.e., $\Lambda(\mathbf{r}, t) = \int_u^t \phi(\mathbf{r}, u)du$, the term in the electric potential vanishes. Renaming $\mathbf{A}'$ by $\mathbf{A}$, the Hamiltonian and $\mathbf{E}$ simplifies to

$$\mathcal{H} = \frac{1}{2m_0}\left(\mathbf{p} + q\mathbf{A}(\mathbf{r}, t)\right)^2, \quad \mathbf{E} = -\frac{\partial\mathbf{A}}{\partial t}$$

3.3.2 Transition rate

The electromagnetic wave of the light modifies the Hamiltonian, via the vector potential $\mathbf{A}$ given as

$$\mathbf{A}(\mathbf{r}, t) = \hat{\mathbf{e}}\frac{\mathcal{A}(\mathbf{r})e^{i\omega t} + \mathcal{A}^*(\mathbf{r})e^{-i\omega t}}{2}$$

where $\hat{\mathbf{e}}$ is the normalized polarization direction and ω the angular frequency of photons.
As $\mathbf{A}^2$ can be neglected[3], we get $(\mathbf{p} + q\mathbf{A})^2 \approx \mathbf{p}^2 + 2q\mathbf{A}\cdot\mathbf{p}$ and the one-electron Hamiltonian $\mathcal{H}_0$ of eq. 3.2 becomes:

$$\mathcal{H}_0 + \mathcal{H}'(\mathbf{r}, t)$$

where $\mathcal{H}'(\mathbf{r}, t)$ takes the same form as in the derivation of the Fermi Golden rule eq. B.2:

$$\mathcal{H}'(\mathbf{r}, t) = \mathcal{H}'(\mathbf{r})e^{i\omega t} + \mathcal{H}'^{\dagger}(\mathbf{r})e^{-i\omega t})$$

with

$$\mathcal{H}' = \frac{q}{2m_0}\mathcal{A}(\mathbf{r})\hat{\mathbf{e}}\cdot\mathbf{p} \quad \text{and} \quad \mathcal{H}'^{\dagger} = \frac{q}{2m_0}\mathcal{A}^*(\mathbf{r})\hat{\mathbf{e}}\cdot\mathbf{p}$$

where * denotes the complex conjugate and $\mathcal{H}'^{\dagger}$ is the Hermitian adjoint of $\mathcal{H}'$. [4]
According to the Fermi Golden rules of sect. B, an electron in a state of energy E_1 will see its probability

[3] As per [19], this is due to the orthogonality of the wave functions. [66] justifies by $|q\mathbf{A}| \lll |\mathbf{p}|$.
[4] In appendix A, we show that if $\mathcal{H}' = \frac{q}{2m_0}\mathcal{A}(\mathbf{r})\hat{\mathbf{e}}$, then $\mathcal{H}'^{\dagger} = \frac{q}{2m_0}\mathcal{A}^*(\mathbf{r})\hat{\mathbf{e}}\cdot\mathbf{p}$

to be in a state of energy E_2, separated by $\hbar\omega$, evolves because of the electric field perturbation. The speed at which the probability change is given as:

$$W_{21} = \frac{2\pi}{\hbar}|H'_{21}|^2\delta(E_{21} - \hbar\omega)$$

The Fermi Golden rule was derived here for a system with discrete Eigen-energies. In case of a continuum of Eigen-energy (for an energy band), we have to replace the delta-dirac density by the density of energy E_{21}, the difference of the energy between the two states involved in the transition. Dividing by the volume, this yields to the expression of the transition rate R as:

$$R = \frac{2\pi}{\hbar}|H'_{21}|^2\rho_r(E_{21})|_{E_{21}=\hbar\omega} \tag{3.6}$$

where H'_{21} is the matrix element that defines the strength of overlap between states 1 and 2 detailed in the next section.
$\rho_r(E_{21})$ is the density of all possible transition pairs of states with a energy difference between the two states equal to E_{21}. This density is called **reduced density of states** because it can be computed as a density of states calculated with a reduced mass as derived in sect. 4.5. For bulk active region or for single quantum wells, the density of states can be computed from the formulae of sect. 4. For complex multiple-layer devices, a novel and more accurate expression is derived in sect. 5.6.

3.3.3 Transition matrix element

This section is very short. See [19] for more details. The matrix element $H'_{21} = \langle\psi_2|H'(\mathbf{r})|\psi_1\rangle$ defines the strength of the overlap of the eigen-states 1 and 2 due to the influence of the electric field of photons. For transitions between the conduction and valence bands, assuming that the variation in space of $\mathcal{A}(\mathbf{r})$ is of the form $\mathcal{A}_0 e^{-i\mathbf{k}\cdot\mathbf{r}}$, $|H'_{21}|^2$ is approximated by:

$$|H'_{21}|^2 = \left(\frac{q\mathcal{A}_0}{2m_0}\right)^2 |M_T|^2 \tag{3.7}$$

where $|M_T|^2$ is the transition matrix element defined as:

$$|M_T|^2 = |\langle u_c|\hat{\mathbf{e}}\cdot\mathbf{p}|u_v\rangle|^2 |\langle F_2|F_1\rangle|^2$$

We can see that the strength of the transition rate depends on the geometry of the Bloch functions and on the inner products of the envelop wave functions. With further approximations, $|M_T|^2$ is expressed as

$$|M_T|^2 = \frac{|M_T|^2}{|M|^2}|M|^2$$

where $\frac{|M_T|^2}{|M|^2}$ depends on the polarization and the symmetries of the Eigen-states of the bands and is given in table 3. $|M|^2$ is a constant per alloy, expressed by $|M|^2 = \frac{m_0 E_p}{2}$ where E_p is homogeneous to an energy and is found in table 2.
Finally R reads

$$R = \frac{2\pi}{\hbar}\left(\frac{q\mathcal{A}_0}{2m_0}\right)^2 |M_T|^2\rho_r(E_{21})|_{E_{21}=\hbar\omega} \tag{3.8}$$

3.3.4 k selection rule

Because of the Hermitian inner product of the envelop functions $\langle F_2|F_1\rangle$, transitions are only possible:

- if preserving $\mathbf{k}$ for bulk: Hence the so-called $\mathbf{k}$ preservation rule. [5]
- between same quantum numbers (for instance $n_v = n_c = 1$) for quantum wells. [6]

3.4 Material gain of simulated emissions

3.4.1 Stimulated emission and absorption

A stimulated emission occurs when the state of an electron evolves from the conduction band to the valence band. For each transition, the electron liberates an amount of energy equal to $\hbar\omega$, therefore a new photon is emitted.
Stimulated absorption is when the energy of an incoming photon is transferred to an electron that moves from the valence band to the conduction band.
Both transitions occur at the same transition rate R of eq. 3.8, but only if the starting state is occupied by a carrier and the arrival state is empty. Therefore, they occur respectively at the rate R_{21} and R_{21}:

$$R_{21} = R \times f_2(1 - f_1)$$
$$R_{12} = R \times f_1(1 - f_2)$$

where f_1 and f_2 are the so-called Fermi factors, the occupation probabilities of the states given by the Fermi statistics further described in sect. 6.1.1.
The net transition rate born from stimulation by light is therefore:

$$R_{\text{st.}} = \frac{dN_p}{dt} = R_{21} - R_{12} = R \times (f_2 - f_1) \tag{3.9}$$

3.4.2 General expression of the gain

As we are interested in the increase of the light intensity along the axis z, the material gain due to stimulated emission, is defined as

$$g = \frac{1}{N_p}\frac{dN_p}{dz}$$

where N_p is the photon density along the axis z.
If g is constant, N_p is easily obtained by integration as

$$N(z) = N_0 e^{gz}$$

Because of the expression in exponential the compounding effect of the gain is accounted for. Indeed, if we split the length L into P intervals of length $\frac{L}{P}$, the density at the point $p + 1$ is expressed from the density at the point p by

$$N_{p+1} = N_p e^{g\frac{L}{P}}$$

[5] Because $\langle F_2|F_1\rangle = \delta_{\mathbf{k}_1,\mathbf{k}_2}$. If the spacial dependency of $\mathcal{A}(r)$ was not neglected, the $\mathbf{k}$ preservation rule would require $\mathbf{k}_2 = \mathbf{k}_1 + \kappa$ where κ is the wave vector of the field which can be neglected.

[6] This relies on the orthogonality of the wavefunctions in an infinite-potential wells. When the potential gap is finite, other transitions can occur but with a smaller occurrence.

Compounding gives

$$N(L) = N_0 \prod_{p=1}^{P} e^{g\frac{L}{P}} = N_0 e^{g\frac{L}{P}P} = N_0 e^{gL}$$

Hence, this accounts for the fact that, if a new photon is emitted at some point z, it will itself participate to possible transitions as it travels through the device.
As photons are absorbed or emitted along z, they will also modify the electric field which is the source of the perturbation of the Hamiltonian of electrons in the crystal. This effect is also included in the derivation of the gain below because the modulus of $\mathcal{A}_0$ will be derived from the local density of photon $N_p(z)$.

We now need to relate the transition rate and the gain. This can be done by expressing the gain as a change over time as follows. When photons travel a distance dz, the density changes by dN and it takes a time equal $v_g dt$. Therefore, the change of the density over z is not due to the traveled length per se, but to the time it takes to travel and we can write

$$\frac{dN_p}{dt} = \frac{dN_p}{dz}\frac{dz}{dt} = \frac{dN_p}{dz} v_g$$

where v_g is the group velocity. This yields:

$$g = \frac{1}{v_g N_p}\frac{dN_p}{dt} = \frac{1}{v_g N_p} R_{st}$$

Injecting the transition rate from eq. 3.9 and eq. 3.8 yields:

$$g = \frac{1}{v_g N_p}\frac{2\pi}{\hbar}\left(\frac{q\mathcal{A}_0}{2m_0}\right)^2 |M_T|^2 \rho_r(E_{21})(f_2 - f_1)$$

$\mathcal{A}_0^2$ is derived by expressing the energy of the light in two manners:

- As the total number of photons N_p times the energy per photon $\hbar\omega$, $N_p\hbar\omega$.
- As the energy of the electric field $\frac{1}{2} n n_g \varepsilon_0 \omega^2 |\mathcal{A}_0|^2$ where n_g is the group refractive index such that $n_g v_g = c$.

Finally, the material gain is expressed as

$$g = \frac{\pi q^2 \hbar}{n\varepsilon_0\, cm_0^2}\frac{1}{\hbar\nu}|M_T|^2 \rho_r(E_{21})(f_2 - f_1) \tag{3.10}$$

3.5 Calculation of alloy parameters and impact of strain

The calculation of the gain requires parameters such as the band-gaps and effective masses of the materials used in the device. This section describes how to obtain the parameters for ternary or quaternary alloys from known parameters of common binary alloys. It follows chap. 2 of [68] and is implemented in the Python class Alloy.
Any parameter B for binary III-V alloy is taken from tables 1, 2 and 4. Any parameter T of a ternary alloy AB_xC_{1-x} is obtained by a linear interpolation adjusted by a bowing term C:

$$T_{\text{ABC}}(x) = xB_{\text{AB}} + (1-x)B_{\text{BC}} - x(1-x)C_{\text{ABC}}$$

where C is taken from table 5.
A parameter Q of a quaternary alloy of the form $A_xB_{1-x}C_yD_{1-y}$ is interpolated as:

$$\begin{aligned} Q_{\text{ABCD}}(x,y) = \{ &+ x(1-x)\big(yT_{\text{ABC}}(x) + (1-y)T_{\text{ABD}}(x)\big) \\ &+ y(1-y)\big(xT_{\text{ACD}}(y) + (1-x)T_{\text{BCD}}(y)\big) \} \\ &/\{ x(1-x) + y(1-y) \} \end{aligned}$$

as also discussed in [91] and [90].
The top of valence bands at $\mathbf{k} = 0$ under strain are obtained by a perturbation of the 4×4 Hamiltonian (heavy and light holes bands with spin) and read:

$$\begin{aligned} E^0_{hh} &= E^0_v - P_\varepsilon - Q_\varepsilon \\ E^0_{lh} &= E^0_v - P_\varepsilon + Q_\varepsilon \\ E^0_c &= E^0_v + E_g + R_\varepsilon \end{aligned}$$

In this section only, z is the growth direction of the quantum well to be consistent with the notations with [68]. It is noted x elsewhere in this document.
In the above formulae, we use:

$$\begin{aligned} \varepsilon_{xx} &= \varepsilon_{yy} = \frac{a_{\text{st}} - a}{a} \\ \varepsilon_{zz} &= -2\frac{C_{12}}{C_{11}}\varepsilon_{xx} \\ P_\varepsilon &= -a_v(\varepsilon_{xx} + \varepsilon_{yy} + \varepsilon_{zz}) \\ Q_\varepsilon &= -\frac{b}{2}(\varepsilon_{xx} + \varepsilon_{yy} - 2\varepsilon_{zz}) \\ R_\varepsilon &= a_c(\varepsilon_{xx} + \varepsilon_{yy} + \varepsilon_{zz}) \end{aligned}$$

where a is the lattice constant the alloy, a_{st} is after strain, C_{12} and C_{11} are elastic stiffness constants, a_c and a_v hydrostatic deformation potentials and b the shear deformation potential.
For strained bulk materials, we apply the results of 6×6 to get effective masses (along z and the transverse plane t) of heavy and light holes, and of an 8×8 Hamiltonian for the effective mass in the conduction band. This gives:

$$m^z_{hh} = \frac{m_0}{\gamma_1 - 2\gamma_2} \tag{3.11}$$

$$m^t_{hh} = \frac{m_0}{\gamma_1 + \gamma_2} \tag{3.12}$$

$$m^z_{lh} = \frac{m_0}{\gamma_1 + 2\gamma_2 f} \tag{3.13}$$

$$m^t_{lh} = \frac{m_0}{\gamma_1 - \gamma_2 f} \tag{3.14}$$

$$m_c = m_0\big(1 + 2F_b + \frac{2M_b^2}{m_0}\frac{3E_g + 2\Delta_0}{E_g(E_g + \Delta_0)}\big)^{-1} = m_0\big(1 + 2F_b + \frac{E_p(3E_g + 2\Delta_0)}{E_g(3E_g + 3\Delta_0)}\big)^{-1} \tag{3.15}$$

where $M_b^2 = \frac{m_0}{6} E_p$ is the momentum matrix element for bulk, E_g is the band gap at the Γ point, Δ_0 the split-off energy offset and E_p and F_b are given by tables. f is a strain factor given by

$$
\begin{aligned}
s &= \frac{Q_\varepsilon}{\Delta_0} \\
r &= s - 1 + \sqrt{1 + 2s + 9s^2} \\
f &= \frac{2s(1 + 1.5r) + 6s^2}{0.75r^2 + r - 3s^2}
\end{aligned}
$$

At last band offset alignment is also done as per [68] by electron affinity. E_c^0 is aligned at the electron affinity χ_0 below the universal vacuum energy E_0 by:

$$E_c^0 = E_0 - \chi_0$$

For sake of simplicity χ_0 and unlike in [68] is interpolated in the code as $C(\chi_0) = -0.55C(E_g)$

4 Density of states, carriers and transition pairs

With a state being characterized by its energy and its spin, the **density of states** is the density of the possible number of states as a function of the energy level and per unit of volume. It is expressed in $\mathrm{J}^{-1}\mathrm{m}^{-3}$. The density of state is a key quantity for the material gain and the total gain of active regions of lasers or SOA. Because it is so important and central, this section is dedicated to it and gives detail derivations for the ease of understanding and for the sake of the Python code implementation. We derive results for quantum dots, wires, wells and for bulk, each case being a limit of the prior case as the dimension becomes very large, one direction at a time. Results assume a very **ideal physically-impossible case** where the active region is at zero-potential and limited by infinite potential. Therefore a quantum dot is the classical "particle in a box" problem of quantum mechanics textbooks described in sect. 5.4. Although this ideal case can be accurate enough for bulk and for a single quantum well, sect. 5.6 derives the density of states for a more **realistic multiple quantum well**.
The density of states is required to compute the **density of carriers** N which combines the density of states and the probability of occupation of states. N itself is used in the carrier and photon rate equations that model the dynamics of the SOA and yield to the total gain of a device as discussed in sect. 2. Because N reflects the level of energy injection for the inversion of the band population, it is also necessary to determine quasi-Fermi levels for the conduction and valence bands and to compute the material gain born from net stimulated emission as described in sect. 3.4.
At last, the **density of the possible transition pairs** electron-hole is also necessary for the calculation of the transition rate. We will see it can be computed as a **so-called reduced density of states** for a particle with an appropriate reduced mass.

4.1 Definition of the density of states

Let $N_s(E)$ be the number of possible states inside the volume $V = d_x d_y d_z$, up to energy E. The density of states is defined by $\rho(E)$ such that

$$N_s(E) = V \int_{u=-\infty}^{E} \rho(u)du \tag{4.1}$$

That is, the number of states up to E, per unit of volume is $\int_{u=-\infty}^{E} \rho(u)du$, the integral of the density function $\rho()$ over all energy levels between $-\infty$ and E.
A state is characterized by a wave function and a spin. From sect. 5.4, we know that several states may share the same degenerate energy level. Here, it does not matter as we want to count the number of triplets (n_x, n_y, n_z), multiplied by two for the spin: we are not counting the number of possible energy levels.
Taking the derivatives of eq. 4.1 w.r.t. E gives another definition of ρ, that will be more useful:

$$\rho(E)dE = \frac{dN_s(E)}{V} \tag{4.2}$$

The unit of ρ is $J^{-1}m^{-3}$. It can also be written as $\rho = \frac{dN_s(E)}{V dE}$, where dN_s has no unit (it is a number of carriers),V is in m^3 and dE is in J.

4.2 Parabolic $E - \mathbf{k}$

Action regions can take the shape of quantum dots, wires or wells or be in a bulk format. Now, the assumption of a parabolic energy and effective masses is valid regardless of the shape. From the parabolic expression of the $E-\mathbf{k}$ function of a particle in a box of sect. 5.4, using an effective mass m^*, the energy of a particle in a quantum dot (similar to a box) can be written as:

$$E = \frac{\hbar^2\pi^2}{2m^*}\left(\frac{n_x^2}{d_x^2} + \frac{n_y^2}{d_y^2} + \frac{n_z^2}{d_z^2}\right) = \frac{\hbar^2}{2m^*}\mathbf{k}^2 = \frac{\hbar^2}{2m^*}\left(k_x^2 + k_y^2 + k_z^2\right) \tag{4.3}$$

For sake on convenience, we can also express the energy as the sum of three components along the axes x, y and z by

$$E = E_{n_x} + E_{n_y} + E_{n_z}$$

Whatever the shape of the active region, the density of states that we will obtain for dots is the most generic form and is also valid for all other shapes.
Now, we will derive more convenient expressions for wires, wells and bulk that are merely limit cases of the dot shape. When the length of a dot is becoming very large along one direction, it becomes a wire and the discrete energy increment $\frac{n^2}{d^2}$ along that direction is becoming smaller and smaller as d increases. Eventually, it is so small that we can assume the increment is not discrete anymore and that the component of the energy along this axis becomes continuous.
For all shape, the fact that energy can only take discrete values is always true, but the discrete density of states expressed as a sum of delta dirac function (the delta dirac function is itself a density function) converges to more finite densities, when one or several of the dimensions of action region becomes large.

4.3 Dots, wires, bulk and wells

4.3.1 Dots

The number of states (before accounting for spin) up to E is the infinite sums over n_x, n_y and n_z of 1 if $E \geq E_{n_z} + E_{n_y} + E_{n_x}$ and 0 otherwise. Dividing by the volume and multiplying by 2 for the spin, gives

$$\frac{N_s(E)}{V} = 2\frac{1}{V}\sum_{n_x=1}^{\infty}\sum_{n_y=1}^{\infty}\sum_{n_z=1}^{\infty}\mathbb{1}_{E\geq E_{n_x}+E_{n_y}+E_{n_z}} \tag{4.4}$$

Finally, taking the derivative and simplifying dE on each side, the density reads

$$\rho(E) = 2\frac{1}{V}\sum_{n_x,n_y,n_z}\delta\left(E - (E_{n_x} + E_{n_y} + E_{n_z})\right) \tag{4.5}$$

where δ is the Dirac delta function.

4.3.2 Wires

We rewrite eq. 4.4 as

$$\frac{N_s(E)}{V} = 2\frac{1}{d_x d_y}\sum_{n_x}\sum_{n_y}\frac{1}{d_z}\sum_{n_z=1}^{\infty}\mathbb{1}_{E-E_{n_x}-E_{n_y}\geq E_{n_z}}$$

With $c = E - E_{n_x} - E_{n_y}$, we can write the indicator as

$$\mathbb{1}_{\alpha \frac{n_z^2}{d_z^2} \leq c} = \begin{cases} \mathbb{1}_{n_z \leq d_z \sqrt{\frac{c}{\alpha}}}, & \text{if } c \geq 0 \\ 0, & \text{otherwise} \end{cases}$$

For $c \geq 0$, the inner most sum simply counts the number of integers below or equal a constant, hence this is the mere floor function. Dividing by the length d_z and taking the limit when $d_z \to \infty$ gives

$$\frac{1}{d_z} \lfloor d_z \sqrt{\frac{c}{\alpha}} \rfloor \xrightarrow[d_z \to \infty]{} \sqrt{\frac{c}{\alpha}}$$

For shapes longer than dots, d_z is large in that sense that increments of energy $\frac{\hbar^2 \pi^2}{2m^*} \frac{n_z^2}{d_z^2}$ when n_z goes up by 1 are very small. Therefore, we can take the limit when $d_z \to \infty$

$$\frac{N_s(E)}{V} = 2 \frac{1}{d_x d_y} \sum_{n_x} \sum_{n_y} \begin{cases} \sqrt{\frac{E - E_{n_x} - E_{n_y}}{\alpha}}, & \text{if } E - E_{n_x} - E_{n_y} \geq 0 \\ 0, & \text{otherwise} \end{cases}$$

Taking the derivatives gives

$$\rho(E) = 2 \frac{1}{d_x d_y} \frac{2m^*}{\hbar^2 \pi^2} \sum_{n_x} \sum_{n_y} \begin{cases} \left(\frac{2m^*}{\hbar^2 \pi^2} \left(E - E_{n_x} - E_{n_y} \right) \right)^{-\frac{1}{2}}, & \text{if } E - E_{n_x} - E_{n_y} \geq 0 \\ 0, & \text{otherwise} \end{cases}$$

Finally

$$\rho(E) = 2 \frac{1}{d_x d_y} \frac{2m^*}{\hbar^2 \pi^2} \sum_{n_x, n_y, \frac{2m^*}{\hbar^2 \pi^2} E - \frac{n_y^2}{d_y^2} - \frac{n_z^2}{d_z^2} \geq 0} \left(\frac{2m^*}{\hbar^2 \pi^2} E - \frac{n_y^2}{d_y^2} - \frac{n_z^2}{d_z^2} \right)^{-\frac{1}{2}}$$

4.3.3 Bulk

The density is given by [7]

$$\rho(E) = \frac{1}{2\pi^2} \left(\frac{2m^*}{\hbar^2} \right)^{\frac{3}{2}} \sqrt{E} \tag{4.6}$$

Proof. We work in the space of quantum numbers illustrated by fig. 14. In this space, we compute the volume, i.e. the number of wave functions, of one eighth of a sphere of radius n. To get the number of states including the spin, we multiply it by 2. For n sufficiently large, it can be approximated by:

$$N_s(n) = \frac{1}{8} \times 2 \times \frac{4}{3} \pi n^3 = \frac{\pi n^3}{3}$$

Assuming that the crystal is a cube of size d with $d_x = d_y = d_z = d$, the sphere in the quantum number space is delimited by the surface

$$n_x^2 + n_y^2 + n_z^2 = n^2$$

Eq. 4.3 of the energy is rewritten as:

$$E = \frac{\hbar^2 \pi^2}{2m^* d^2} n^2 \tag{4.7}$$

[7] We can check the unit of ρ again as follows.
$\frac{kg^{\frac{3}{2}}}{J^3 s^3} J^{-\frac{1}{2}} = kg^{\frac{3}{2}} J^{-\frac{5}{2}} s^{-3} = kg^{\frac{3}{2}} kg^{-\frac{5}{2}} m^{-5} s^5 s^{-3} = kg^{-1} m^{-2} s^2 \times m^{-3} = J^{-1} m^{-3}$

Therefore, taking the power $\frac{3}{2}$,

$$n^3 = \left(E \frac{2m^* d^2}{\hbar^2 \pi^2} \right)^{\frac{3}{2}}$$

The number of states up to the energy E is

$$N_s(E) = \frac{\pi}{3} \left(E \frac{2m^* d^2}{\hbar^2 \pi^2} \right)^{\frac{3}{2}}$$

and eq. 4.2 yields:

$$\rho(E)dE = \frac{dN_s(E)}{V} = \frac{1}{V} \frac{\pi}{3} \left(\frac{2m^* d^2}{\hbar^2 \pi^2} \right)^{\frac{3}{2}} \frac{3}{2} \sqrt{E} dE$$

Finally

$$\rho(E) = \frac{1}{d^3} \frac{\pi}{3} \left(\frac{2m^* d^2}{\hbar^2 \pi^2} \right)^{\frac{3}{2}} \frac{3}{2} \sqrt{E} = \frac{1}{2\pi^2} \left(\frac{2m^*}{\hbar^2} \right)^{\frac{3}{2}} \sqrt{E}$$

■

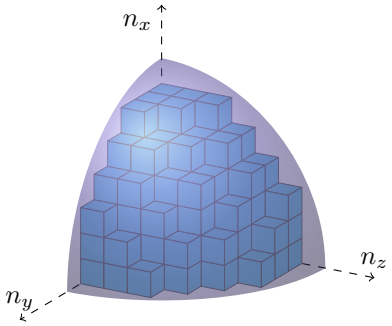

Figure 14: Space of quantum numbers, where each small cube represents a triple of quantum numbers $(n_x, n_y, n_z) \in \mathbb{Z}^{+3}$

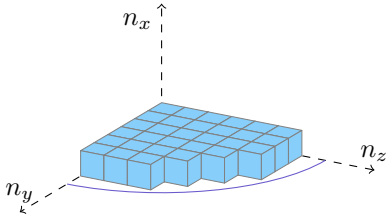

Figure 15: Planar space of quantum numbers for n_x given, where each small cube represents a triple of quantum numbers $(n_x, n_y, n_z) \in \mathbb{Z}^{+3}$

4.3.4 Wells

$$\rho(E) = \frac{m^*}{\pi\hbar^2 d_x} \sum_{n_x=1,\cdots} \mathcal{H}(E - E_{n_x}) \tag{4.8}$$

where

$$E_{n_x} = n_x^2 E_{111} \quad \text{and} \quad E_{111} = \frac{\hbar^2\pi^2}{2m^* d_x^2} \tag{4.9}$$

and $\mathcal{H}$ is the heavyside unit step function: $\mathcal{H}(x) = 1$ for $x > 0$, and null otherwise.
This can be also written as:

$$\rho(E) = \frac{m^*}{\pi\hbar^2 d_x} \lfloor d_x \sqrt{E \frac{2m^*}{\hbar^2\pi^2}} \rfloor$$

Proof. First, we count the number of states in the disk of fig. 15, where the scales of the axes are expressed in quantum numbers. We measure $N_s(n_y, n_z)$, the surface of one-fourth (because the quantum numbers are positive) of the ellipse defined by n_x and n_y, multiplied by two for the spins. Note that we compute the surface as if the quantum numbers were not discrete but continuous:

$$N_s(n_y, n_z) = \frac{1}{4} \times 2 \times \pi(n_y^2 + n_z^2) = \frac{\pi}{2}(n_y^2 + n_z^2)$$

Let's split E of eq. 4.7 into the energy coming from x and the energy coming from y and z:

$$E = E_{n_x} + E_{n_y,n_z}$$

with $E_{n_x} = \frac{\hbar^2\pi^2 n_x^2}{2m^* d_x^2}$ and $E_{n_y,n_z} = \frac{\hbar^2\pi^2}{2m^*}\left(\frac{n_y^2}{d_y^2} + \frac{n_z^2}{d_z^2}\right)$.
Assuming $d_y = d_z = d$ [8] and injecting $N_s(n_y, n_z)$, we have:

$$E_{n_y,n_z} = \frac{\hbar^2\pi^2}{2m^* d^2}(n_y^2 + n_z^2) = \frac{\hbar^2\pi^2}{2m^* d^2}\frac{2}{\pi}N_s(n_y, n_z)$$

Therefore, the number of states up to the energy level E_{n_y,n_z}, for quantum numbers up to n_y and n_z is given by:

$$N_s(n_y, n_z) = \frac{m^* d^2}{\pi\hbar^2} E_{n_y,n_z}$$

For a given n_x, if $E - E_{n_x} < 0$, there are no valid states as E_{n_y,n_z} cannot be negative. if $E - E_{n_x} > 0$, then $E_{n_y,n_z} > 0$ and the number of states up to $E_{n_y,n_z} = E - E_{n_x}$ is $\frac{m^* d^2}{\pi\hbar^2}(E - \frac{\hbar^2\pi^2 n_x^2}{2m^* d_x^2})$. Taking the sum over the possible n_x, we obtain:

$$N_s(E) = \sum_{n_x=1,\cdots} \frac{m^* d^2}{\pi\hbar^2}(E - E_{n_x})^+$$

where $()^+$ is the ramp function defined by $x^+ = \begin{cases} x, & \text{if } x \geq 0 \\ 0, & \text{otherwise} \end{cases}$ and whose derivatives is the Heaviside unit step function: $\frac{dx^+}{dx} = \mathcal{H}(x) = \begin{cases} 1, & \text{if } x \geq 0 \\ 0, & \text{otherwise} \end{cases}$.
Using the definition of the density by eq. 4.2 gives:

$$\rho(E)dE = \frac{dN_s(E)}{V} = \frac{1}{V} \sum_{n_x=1,\cdots} \frac{m^* d^2}{\pi\hbar^2}\mathcal{H}(E - E_{n_x})dE$$

[8] When $d_y \neq d_z$, the same result can be derived using the Gauss Circle problem in the case of ellipses.

Finally, with $V = d^2 d_x$,

$$\rho(E) = \frac{m^*}{\pi\hbar^2 d_x} \sum_{n_x} \mathcal{H}(E - E_{n_x}) = \frac{m^*}{\pi\hbar^2 d_x} \sum_{n_x} \mathbb{1}(E_{n_x} \leq E)$$

Again, $\mathcal{H}(E-E_{n_x})$ can be written as $\mathbb{1}(E_{n_x} \leq E) = \mathbb{1}(n_x \leq d_x\sqrt{E\frac{2m^*}{\hbar^2\pi^2}})$ and their sum is $\lfloor d_x\sqrt{E\frac{2m^*}{\hbar^2\pi^2}}\rfloor$. Finally,

$$\rho(E) = \frac{m^*}{\pi\hbar^2 d_x}\lfloor d_x\sqrt{E\frac{2m^*}{\hbar^2\pi^2}}\rfloor$$

Note that the unit of the density is still per unit of volume. d_x appears at the denominator because the number of states, that we divide by the volume V, is discrete in n_x and therefore not proportional to d_x, unlike in the case of bulk regime. ■

Properties

- $\rho(E)$ has a stair-like shape, going up by increments of $\frac{m^*}{\pi\hbar^2 d_x}$ at each squared-integer multiple of E_{111}.
- For E equal to E_{n_x}, the densities of the bulk and well are equal. Indeed, for $E = \frac{\hbar^2\pi^2 n_x^2}{2m^* d_x^2}$, we have

$$\rho_{\text{bulk}}(E) = \frac{1}{2\pi^2}\left(\frac{2m^*}{\hbar^2}\right)^{\frac{3}{2}}\left(\frac{\hbar^2\pi^2 n_x^2}{2m^* d_x^2}\right)^{\frac{1}{2}} = \frac{1}{2\pi^2}\left(\frac{2m^*}{\hbar^2}\right)^{\frac{3}{2}}\frac{n_x\hbar\pi}{(2m^*)^{\frac{1}{2}}d_x} = n_x\frac{m^*}{\pi\hbar^2 d_x} = \rho_{\text{QW}}(E)$$

- When d_x tends to $+\infty$, the density of the well tends to the density of the bulk because

$$\frac{1}{d_x}\lfloor d_x\sqrt{E\frac{2m^*}{\hbar^2\pi^2}}\rfloor \xrightarrow[d_x\to\infty]{} \sqrt{E\frac{2m^*}{\hbar^2\pi^2}}$$

This is illustrated by fig. 16a.

4.4 Application to conduction and valence bands

In the above section, we assumed that the energy of the particle was only coming from its term in $\mathbf{k}^2$ because the particle was in a box at zero potential. In order to compute the density of states for the conduction and valence bands, we need to make the adjustment discussed below.

At the bottom of the conduction band, the energy reads $E - E_c = \frac{\hbar^2 k^2}{2m_c}$, where m_c is the effective mass in the conduction band for the relevant crystal. This is the same expression in k^2 as eq. 4.3. Therefore, $E-E_c$ is subject to the same quantum constraints (i.e. the boundary conditions of Schrödinger differential equation) as in the prior sections and the density of states is obtained by simply replacing E by $E - E_c$ for $E \geq E_c$ and m^* by m_c.

Likewise, at the top of the valence band, the parabola is $E_v - E = \frac{\hbar^2 k^2}{2m_v}$ and the density of states is obtained by replacing E by $E_v - E$ for $E < E_v$ and m^* by m_v.

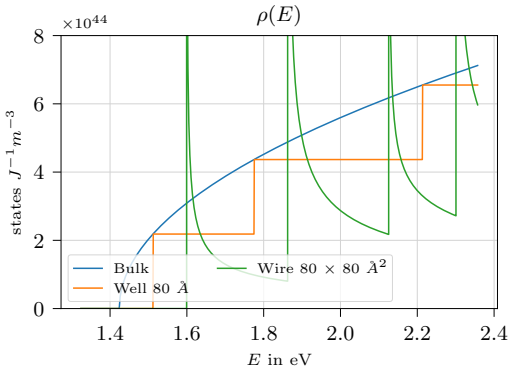

(a) Comparison between bulk, well with $d_x = 80\mathring{A}$ and wire with $d_x = d_y = 80\mathring{A}$. Densities of bulk and well are equal for $E = n_x^2 E_{111}$.

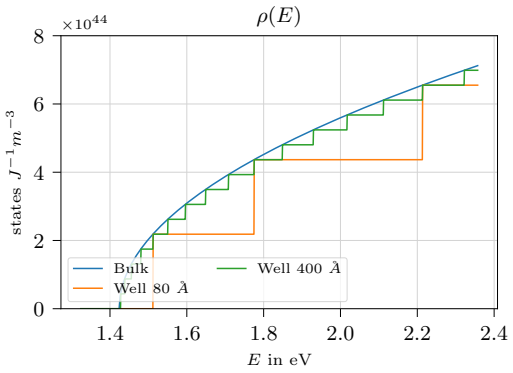

(b) The density of state of a well converges to that of a bulk when d_x increases from $d_x = 80\mathring{A}$ to $d_x = 400\mathring{A}$).

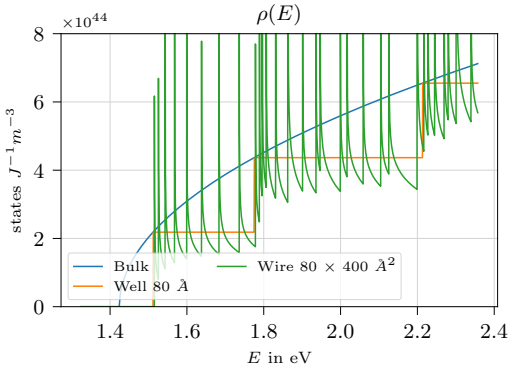

(c) The density of a wire converges to that of a well when d_y is large at $400\mathring{A}$ for the same $d_x = 80\mathring{A}$. Note that the square root terms of the wire are going to infinity at discrete values but are not well represented here due to the limited number points for the E abscissa.

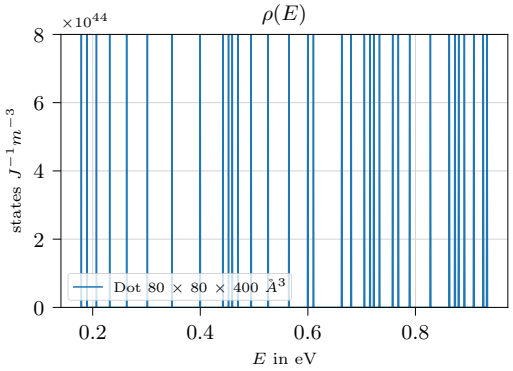

(d) The density of states for a dot with $d_x = d_y = 80\mathring{A}$ and $d_z = 400\mathring{A}$ is a series of Dirac delta functions represented by infinite vertical lines.

Figure 16: Densities of states of GaAs structures for bulk, well, wire and dot, assuming $E_{F_c} = 2eV$, with $m_c = 0.067$,$E_c = 1.424eV$ and 300K.

4.5 Reduced density of states

Reduced mass and density of states The reduced density of states refers to the density of transition pairs at E_{21}. In order to estimate the gain, we must combine the density of possible states in the valence and the conduction band for the transition of energy E_{21} at iso-momentum. As the transition energy is the sum of the bandgap and the kinetic energies of the electron and the hole that share the same k, we can write:

$$E_{21} = E_g + \frac{\hbar^2 k^2}{2m_c} + \frac{\hbar^2 k^2}{2m_v}$$

Hence,

$$E_{21} - E_g = \frac{\hbar^2 k^2}{2m_r}$$

where m_r is the reduced mass defined from:

$$\frac{1}{m_r} = \frac{1}{m_c} + \frac{1}{m_v}$$

The density of possible transition pairs is obtained by replacing E by $E_{21} - E_g$ for $E_{21} > E_g$, and m^* by the reduced mass m_r.

4.6 Carrier densities

This section describes the calculation[9] of carrier density for conduction and valence bands, for bulk material and simple quantum wells.
Carrier densities will be needed to infer the quasi Fermi levels, that determine the probability of occupation of states, from the density of carriers that are pumped into the device.

4.6.1 Bulk

Conduction band For bulk regime, the carrier density of the conduction band is:

$$N = \frac{1}{2\pi^2}\left(\frac{2m_c}{\hbar^2}\right)^{\frac{3}{2}} \int_{E_c}^{+\infty} \frac{1}{e^{(E-E_{F_c})/k_BT}+1}\sqrt{E-E_c}dE$$

To be rigorous, we should integrate up to the top of the conduction band. However, as the Fermi function becomes tiny for energies which are more than a few k_BT above the Fermi level, we can replace by $+\infty$ without introducing much errors.
Setting $x = \frac{E-E_c}{k_BT}$[10], $v = (E_{F_c} - E_c)/k_BT$ and integrating for $E \geq E_c$ gives:

$$\begin{aligned} N &= N_c \frac{2}{\sqrt{\pi}} \int_0^{+\infty} \frac{1}{e^{x-v}+1}\sqrt{x}dx \\ &= N_c \frac{2}{\sqrt{\pi}} F_{1/2}(v) \end{aligned} \tag{4.10}$$

where $N_c = 2\left(\frac{m^* k_B T}{2\pi\hbar^2}\right)^{\frac{3}{2}}$ is called the *effective* density of states in the conduction band, and $F_{1/2}(v)$ denotes the Fermi-Dirac integral of order 1/2.

Valence band For holes in the valence band, we use the probability of non-occupation, $1 - f_1$ and we have:

$$P = \frac{1}{2\pi^2}\left(\frac{2m_v}{\hbar^2}\right)^{\frac{3}{2}} \int_{-\infty}^{E_v} \left(1 - \frac{1}{e^{(E-E_{F_v})/k_BT}+1}\right)\sqrt{E_v - E}dE$$

As $\frac{1}{e^y+1}$ is anti-symmetric[11], we rewrite P as:

$$P = \frac{1}{2\pi^2}\left(\frac{2m_v}{\hbar^2}\right)^{\frac{3}{2}} \int_{-\infty}^{E_v} \frac{1}{e^{(E_{F_v}-E)/k_BT}+1}\sqrt{E_v - E}dE$$

[9] Implemented in StateAndCarrierDensity.py
[10] $dE = k_BTdx$
[11] $1 - \frac{1}{e^y+1} = \frac{e^y}{e^y+1} = \frac{1}{e^{-y}+1}$

Defining $x = \frac{E_v - E}{k_B T}$[12] and $v = (E_{F_v} - E_v)/k_B T$ gives:

$$\begin{aligned} P &= N_v \frac{2}{\sqrt{\pi}} \int_0^{+\infty} \frac{1}{e^{x+v}+1} \sqrt{x} dx \\ &= N_v \frac{2}{\sqrt{\pi}} F_{1/2}(-v) \end{aligned} \tag{4.11}$$

4.6.2 Quantum well

Conduction band with $E \geq E_c$

$$N = \int_{E_c}^{\infty} \rho(E - E_c) f_2(E) dE = \int_{E_c}^{\infty} \frac{1}{e^{(E-E_{F_c})/k_B T}+1} \frac{m^*}{\pi \hbar^2 d_x} \sum_{n_x} \mathcal{H}(E - E_c - E_{n_x}) dE$$

With $v = E - E_c$

$$\begin{aligned} N &= \int_0^{\infty} \frac{1}{e^{(v+E_c-E_{F_c})/k_B T}+1} \frac{m^*}{\pi \hbar^2 d_x} \sum_{n_x} \mathcal{H}(v - E_{n_x}) dv \\ &= \frac{m^*}{\pi \hbar^2 d_x} \sum_{n_x} \int_0^{\infty} \frac{1}{e^{(v+E_c-E_{F_c})/k_B T}+1} \mathcal{H}(v - E_{n_x}) dv \\ &= \frac{m^*}{\pi \hbar^2 d_x} \sum_{n_x} \int_{E_{n_x}}^{\infty} \frac{1}{e^{(v+E_c-E_{F_c})/k_B T}+1} dv \end{aligned}$$

With $u = e^{-\frac{v+E_c-E_{F_c}}{kT}}$ and $du = -\frac{u}{kT} dv$, we have:

$$\begin{aligned} \int_{E_{n_x}}^{\infty} \frac{1}{e^{(v+E_c-E_{F_c})/k_B T}+1} dv &= -kT \int_{e^{-\frac{E_{n_x}+E_c-E_{F_c}}{kT}}}^{0} \frac{du}{u(1+\frac{1}{u})} = kT \int_0^{e^{-\frac{E_{n_x}+E_c-E_{F_c}}{kT}}} \frac{1}{1+u} du \\ &= kT [\log(1+u)]_0^{e^{-\frac{E_{n_x}+E_c-E_{F_c}}{kT}}} = kT \log\left(1 + e^{\frac{E_{F_c}-E_{n_x}-E_c}{kT}}\right) \end{aligned}$$

Re-injecting in the expression of N gives:

$$N = \frac{kT m^*}{\pi \hbar^2 d_x} \sum_{n_x} \log\left(1 + e^{\frac{E_{F_c}-E_{n_x}-E_c}{kT}}\right) \tag{4.12}$$

Note the d_x at the denominator disappears for the surface density $N dx$, but it still depends on dx because E_{n_x} does as per eq. 4.9.

Valence band with $E \leq E_v$

$$P = \int_{-\infty}^{E_v} \rho(E_v - E)\,(1 - f_1(E))\,dE = \int_{-\infty}^{E_v} \frac{1}{e^{(E_{F_v}-E)/k_B T}+1} \frac{m^*}{\pi \hbar^2 d_x} \sum_{n_x} \mathcal{H}(E_v - E - E_{n_x}) dE$$

[12] $dE = -k_B T dx$

With $v = E_v - E$

$$\begin{aligned} P &= -\int_{+\infty}^{0} \frac{1}{e^{(E_{F_v}+v-E_v)/k_BT}+1} \frac{m^*}{\pi\hbar^2 d_x} \sum_{n_x} \mathcal{H}(v-E_{n_x})dv \\ &= \frac{m^*}{\pi\hbar^2 d_x} \sum_{n_x} \int_{0}^{\infty} \frac{1}{e^{(E_{F_v}+v-E_v)/k_BT}+1} \mathcal{H}(v-E_{n_x})dv \\ &= \frac{m^*}{\pi\hbar^2 d_x} \sum_{n_x} \int_{E_{n_x}}^{\infty} \frac{1}{e^{(E_{F_v}+v-E_v)/k_BT}+1} dv \end{aligned}$$

With $u = e^{-\frac{E_{F_v}+v-E_v}{kT}}$ and $du = -\frac{u}{kT}dv$, we have:

$$\begin{aligned} \int_{E_{n_x}}^{\infty} \frac{1}{e^{(E_{F_v}+v-E_v)/k_BT}+1} dv &= -kT \int_{e^{-\frac{E_{F_v}+E_{n_x}-E_v}{kT}}}^{0} \frac{du}{u(1+\frac{1}{u})} \\ &= kT[\log(1+u)]_0^{e^{-\frac{E_{F_v}+E_{n_x}-E_v}{kT}}} = kT\log\left(1+e^{-\frac{E_{F_v}+E_{n_x}-E_v}{kT}}\right) \end{aligned}$$

This gives:

$$P = \frac{kTm^*}{\pi\hbar^2 d_x} \sum_{n_x} \log\left(1+e^{-\frac{E_{F_v}+E_{n_x}-E_v}{kT}}\right) \tag{4.13}$$

5 Potential wells

In a device made of layers of various semiconductors, the Schrödinger equation of a carrier is the usual ordinary differential equation of a particle in a quantum well studied in quantum mechanics. Hence, this section begins with a reminder of the derivation of the Eigen-solutions of an ideal one-dimensional infinite or finite potential well. Although this is theoretical, it is necessary to introduce and understand the more complex cases.
In reality, the structure of a semiconductor is such that the carrier behaves as if it was a free particle that had a specific *effective* mass, different in each layer. Besides, the energy band-gap in each layer is also different. Therefore, it is necessary to solve the Schrödinger equation with an Hamiltonian with masses and potentials dependent on layers.
This is the ultimate object of sect. 5.6 which handles the most general case of multiple layers in three-dimensions and proposes a new derivation of the density of states with Eigen-energy using an inverse probability-weighted average mass in the transversal plane.

5.1 General problem

We consider a particle subject to a potential V that is constant over time but not necessarily over space. We look for stationary solutions (also called time-independent) of the Schrödinger equation such that:

$$-\frac{\hbar^2}{2m}\nabla^2\psi(\mathbf{r}) + V(\mathbf{r})\psi(\mathbf{r}) = E\psi(\mathbf{r})$$

where E is an eigenvalue of the Hamiltonian, constant over time.
If the potential is only a function of x, the wave function also is only a function of x, that is:

$$\forall \mathbf{r} \quad \psi(\mathbf{r}) = \psi(x)$$

Note that this means that the potential is extending to infinity along the directions y and z.
The equation becomes

$$-\frac{\hbar^2}{2m}\frac{\partial^2\psi}{\partial x^2} + V(x)\psi(x) = E\psi(x)$$

or

$$\psi'' = \frac{2m}{\hbar^2}\left(V - E\right)\psi$$

We will consider the case of E constant over an interval of x.

Case of E larger than V Let $k = \sqrt{-\frac{2m}{\hbar^2}\left(V - E\right)}$, the equation simplifies to

$$\psi'' = -k^2\psi$$

with general solutions of the form[13]

$$\psi = \frac{A}{2}e^{ikx} + \frac{B}{2}e^{-ikx}$$

[13]This is a well-known expression. To see that a general solution is $\psi = \frac{A}{2}e^{ikx} + \frac{B}{2}e^{-ikx}$, we proceed in two steps. First, it is easy to check that both $f = e^{ikx}$ and $g = e^{-ikx}$ are solutions. For instance, we have $f' = ike^{ikx} = ikf$ and $f'' = -k^2 f$. Second, as the equation is of order 2, its solutions belong to a vector space of dimension 2, a sub-space of the functions that are twice-differentiable. At last, because their Wronskian $W(x)$ is not null for x, i.e. $\forall x$, $\begin{vmatrix} f(f) & g(x) \\ f'(x) & g'(x) \end{vmatrix} \neq 0$, then, for any solution h, there are constant coefficients λ_1 and λ_2 such that $h = \lambda_1 f + \lambda_2 g$.

Case of E smaller than V Let $\kappa = \sqrt{\frac{2m}{\hbar^2}(V-E)}$, the equation simplifies to

$$\psi'' = \kappa^2 \psi$$

with general solutions of the form

$$\psi = Ce^{\kappa x} + De^{-\kappa x}$$

5.2 Infinite well

Let's consider an infinite potential well with $V = 0$ for $x \in [0, d]$ and infinite elsewhere. Because the potential is null, the only energy of the particle is its kinetic energy, $E = \frac{p^2}{2m}$. Hence, the variable k defined above is the so-called wave vector (a scalar in this case) $k = \frac{p}{\hbar}$. Because of the infinite potential barrier, the particle can not be at $x = 0$ or $x = d$. Hence, ψ must be null. At $x = 0$, the condition implies that $B = -A$ and ψ becomes:

$$\psi = \frac{A}{2}\left(e^{ikx} - e^{-ikx}\right) = iA\sin(kx)$$

To get 0 at $x = d$, we can see that kx needs to be a multiple of π. Therefore, there must exist an integer n such that:

$$kd = n\pi$$

E can therefore only take discrete values given by the De Broglie energy equation:

$$E = \frac{p^2}{2m} = n^2 \frac{1}{2m}\left(\frac{\hbar\pi}{d}\right)^2 = n^2 E_1^\infty \tag{5.1}$$

with

$$E_1^\infty = \frac{1}{2m}\left(\frac{\hbar\pi}{d}\right)^2 \tag{5.2}$$

At last, we get A by normalizing the total probability P[14]:

$$P = \int_0^d \psi^2(x)dx = -A^2\int_0^d \sin^2(kx)dx = -A^2\frac{d}{2} = 1 \quad \Rightarrow \quad A = \pm i\sqrt{\frac{2}{d}}$$

Finally, the wave function depicted in fig. 17 are given as

$$\psi(x) = \pm\sqrt{\frac{2}{d}}\sin(kx)$$

The sign does not matter as both choices represent the same state and the same probability density.

[14] Let's show that $\int_0^d \sin^2(kx)dx = \frac{d}{2}$.

$$\int_0^d \sin^2(kx)dx = -\frac{1}{k}\int_0^d \sin(kx)\cos'(kx)dx = -\frac{1}{k}\left([\sin(kx)\cos'(kx)]_0^d - k\int_0^d \cos^2(kx)dx\right) = \int_0^d \cos^2(kx)dx$$

where we replaced $\sin(kx)$ by $-\frac{1}{k}\cos'(kx)$ and used the fact that $\sin(kx) = 0$ at the boundaries. Besides, we have $\int_0^d \sin^2(kx)dx + \int_0^d \cos^2(kx)dx = \int_0^d \left(\cos^2(kx) + \sin^2(kx)\right)dx = d$. Finally, we get $\int_0^d \sin^2(kx)dx = \frac{d}{2}$

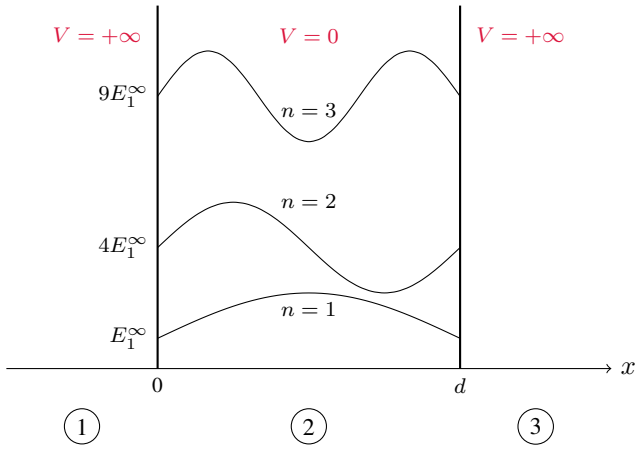

Figure 17: Energy levels and wave functions of a particle in a infinite well for quantum numbers 1, 2 and 3. For sake of the illustration, the wave function ordinates are translated by their energy levels. In fact, they all are oscillating around 0.

Notes:

- The same result applies if the potential was a non-null, constant inside the well, as potential are only known relative to an arbitrary origin. A shift of origin will only shift the Eigen-values by the same amount.
- A particle can not be outside the well otherwise it would have an infinite energy from the potential alone. This is physically not possible.
- n can not be null otherwise ψ would be null everywhere. As $\psi^2(x)$ is the probability density of the presence of the particle at x, it would mean that the particle is nowhere.

5.3 Finite well

In this section, we consider a well with barriers at $x = -\frac{d}{2}$ $x = +\frac{d}{2}$ and a finite potential V and look for solutions of the Schrödinger equation with energies below V. We will express the solution $\psi(x)$ piecewise by ψ_1, ψ_2 and ψ_3 fo the three regions defined in fig. 17.
In regions (1) and (3) of the well of fig. 17 , if $E < V$, the wave functions are of the form:

$$\psi = Ce^{\kappa x} + De^{-\kappa x}$$

In (1) (resp. (3)), as x can go to $-\infty$ (resp. $+\infty$), D (resp. C) must be null, otherwise the function will diverge which is not physically possible. Therefore, we get:

$$\psi_1 = Ce^{\kappa x} \quad \text{and} \quad \psi_3 = De^{-\kappa x}$$

In (2), the function is of the form

$$\psi_2 = \frac{A}{2}e^{ikx} + \frac{B}{2}e^{-ikx}$$

At the boundaries $x = \pm\frac{d}{2}$, the continuity of ψ and its derivatives ψ' will impose conditions for the integration constants.

5.3.1 Symmetric solutions

Let's look for symmetrical solutions first. The symmetry imposes three conditions:

- $C = D$ for decay tails.
- $A = B$ to have $\psi_2(-x) = \psi_2(x)$. Therefore $\psi_2 = A\cos(kx)$.
- We only need to do the derivation for one boundary.

The continuity of ψ and ψ' gives

$$A\cos\left(k\frac{d}{2}\right) = De^{-\kappa\frac{d}{2}} \quad \text{and} \quad Ak\sin\left(k\frac{d}{2}\right) = -D\kappa e^{-\kappa\frac{d}{2}}$$

Taking the ratio of these two equations gives

$$\tan\left(k\frac{d}{2}\right) = \frac{\kappa}{k}$$

and replacing k and κ by their values yields:

$$\tan\left(\sqrt{\frac{m}{2}}\frac{d}{\hbar}\sqrt{E}\right) = \sqrt{\frac{V}{E} - 1} \tag{5.3}$$

5.3.2 Antisymmetric solutions

For Antisymmetric solutions, the boundary conditions are:

- $C = -D$
- $B = -A$, $\psi_2 = iA\sin(kx)$.
- We only need to do the derivation for one boundary.

and expressed by:

$$iA\sin\left(k\frac{d}{2}\right) = De^{-\kappa\frac{d}{2}} \quad \text{and} \quad iAk\cos\left(k\frac{d}{2}\right) = D\kappa e^{-\kappa\frac{d}{2}}$$

Taking the ratio gives

$$\cot\left(k\frac{d}{2}\right) = -\frac{\kappa}{k}$$

With $\cot(x) - \tan\left(x - \frac{\pi}{2}\right)$ and replacing k and κ by their values, gives

$$\tan\left(\sqrt{\frac{m}{2}}\frac{d}{\hbar}\sqrt{E} - \frac{\pi}{2}\right) = \sqrt{\frac{V}{E} - 1} \tag{5.4}$$

5.3.3 Example

[15] Terms of eq. 5.3 and 5.4 are illustrated in fig. 18 for two values of V. The energy is quantified as the intersections of the tangent or cotangent and $\sqrt{\frac{V}{E}-1}$. The multiplicity of energies is born from the periodicity of the trigonometric functions.
As E must be smaller than V, the number of solutions is

$$\lceil\sqrt{\frac{V}{E_1^\infty}}\rceil$$

and increases with the potential.
The nth solution E_n is noted using a non-integer quantum number q_n defined as $q_n = \sqrt{\frac{E_n}{E_1^\infty}}$. q_n is smaller than n but converges to n as the potential rises. We have

$$q_n \leq n$$

The symmetrical and anti-symmetrical solutions are represented in fig. 19 for the same two values of V. We observe that there are more solutions for energies below V if V is higher. We can also see that the probability density tends to zero as the particle goes deeper into the barrier.
In the next two sections, we determine A and D by normalizing the probability.

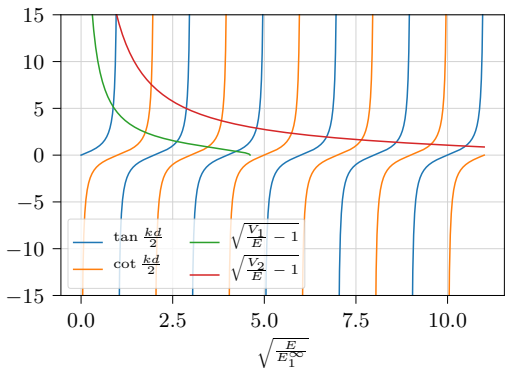

Figure 18: Discrete solutions of the finite well energy levels, for a well of width $d = 200\mathring{A}$. We show the right-hand part of eq. 5.3 and 5.4 with two values of potential $V_1 = 20meV$ (green line) and $V_2 = 200meV$ (red line). The non-integer quantum numbers q of the solutions are the abscissas of the intersections points. For larger potential, the number of solutions increases and the quantum numbers q_n converge to n, the values for infinite potential.

5.3.4 Probability for symmetric case

With $D = A\cos(k\frac{d}{2})e^{\kappa\frac{d}{2}}$, we find A by normalizing the probability:

$$P = D^2\left(\int_{-\infty}^{-\frac{d}{2}} e^{2\kappa x}dx + \int_{\frac{d}{2}}^{\infty} e^{-2\kappa x}dx\right) + A^2\int_{-\frac{d}{2}}^{\frac{d}{2}}\cos^2(kx)dx = 1$$

[15] Implemented in FiniteWell.py

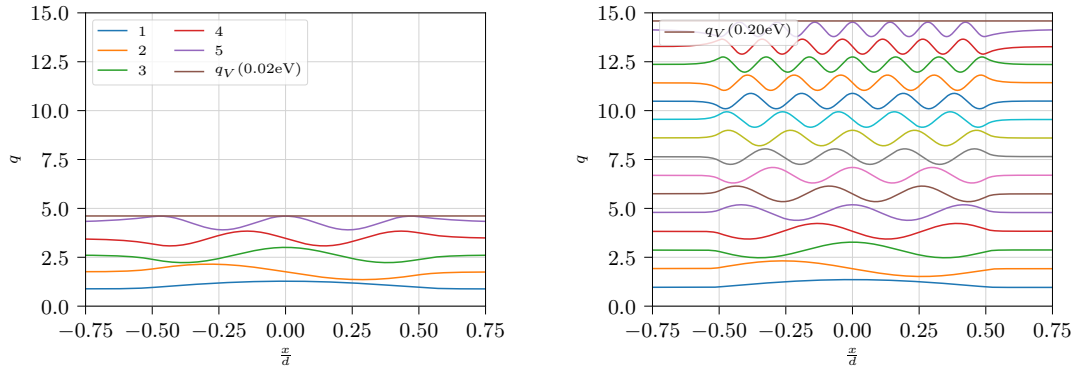

Figure 19: Quantum energy levels and wave functions in a 200$\mathring{A}$-width quantum well for $x \in [-\frac{d}{2}, \frac{d}{2}]$, with $V = 20meV$ and $V = 200meV$. The graphs are the wave functions shifted up by their quantum number: $q_n + 0.4\sqrt{\frac{d}{2}}\psi_n(x)$ where the multiplier of ψ was chosen to *normalize* A. Lines representing V are for $q_V = \sqrt{\frac{V}{E_1^\infty}}$. The number of solutions increases with the potential as it takes more energy levels to *fill* the well height represented by q_V. The particle can get outside the well more easily, that it ψ^2 is larger outside, at high energy levels relative to the potential barrier.

As the two terms for the tails are equal, we only calculate one:

$$\int_{+\frac{d}{2}}^{\infty} e^{-2\kappa x} dx = \left[-\frac{1}{2\kappa} e^{-2\kappa x}\right]_{\frac{d}{2}}^{+\infty} = \frac{1}{2\kappa} e^{-\kappa d}$$

Next, we compute the term in cosine.

$$\int_{-\frac{d}{2}}^{\frac{d}{2}} \cos^2(kx) dx = \frac{1}{k} \int_{-\frac{d}{2}}^{+\frac{d}{2}} \cos(kx) \sin'(kx) dx = \frac{1}{k} \left(\left[\cos(kx) \sin'(kx)\right]_{-\frac{d}{2}}^{+\frac{d}{2}} + k \int_{-\frac{d}{2}}^{+\frac{d}{2}} \sin^2(kx) dx \right)$$
$$= \left[\cos^2(kx)\right]_{-\frac{d}{2}}^{+\frac{d}{2}} + \int_{-\frac{d}{2}}^{+\frac{d}{2}} \sin^2(kx) dx = \int_{-\frac{d}{2}}^{+\frac{d}{2}} \sin^2(kx) dx$$

Therefore, because of the symmetry of $\cos^2$, we have

$$\int_{-\frac{d}{2}}^{\frac{d}{2}} \cos^2(kx) dx = \int_{-\frac{d}{2}}^{\frac{d}{2}} \sin^2(kx) dx = \frac{d}{2}$$

The probability becomes

$$P = A^2 \left(\frac{\cos^2(k\frac{d}{2}) e^{\kappa d}}{\kappa} e^{-\kappa d} + \frac{d}{2} \right) = A^2 \left(\frac{\cos^2(k\frac{d}{2})}{\kappa} + \frac{d}{2} \right) = 1$$

Finally

$$A = \left(\frac{\cos^2(k\frac{d}{2})}{\kappa} + \frac{d}{2} \right)^{-\frac{1}{2}} \quad \text{and} \quad D = A \cos\left(k\frac{d}{2}\right) e^{\kappa \frac{d}{2}}$$

5.3.5 Probability for antisymmetric case

The probability becomes

$$P = \frac{D^2}{\kappa} e^{-\kappa d} - A^2 \frac{d}{2} = -A^2 \left(\frac{\sin^2(k\frac{d}{2})}{\kappa} + \frac{d}{2} \right) = 1$$

Noting $\tilde{A} = \frac{A}{i}$,

$$\tilde{A} = \left(\frac{\sin^2(k\frac{d}{2})}{\kappa} + \frac{d}{2} \right)^{-\frac{1}{2}} \quad \text{and} \quad D = -\tilde{A} \sin\left(k\frac{d}{2}\right) e^{\kappa \frac{d}{2}}$$

Note In both cases, A is closed to the value $\sqrt{\frac{2}{d}}$ obtained for infinite wells.

5.3.6 Probability of the particle to be outside

Unlike in the case of infinite potential barriers, the particle can be outside of the well despite it has an energy lower than the potential of the barrier. It is interesting to see what is the probability of the particle to be outside. The probability illustrated in fig. 20 can be be written as $\frac{d_1}{d_1 + \frac{d}{2}}$ where $d_1 = \frac{\cos^2(k\frac{d}{2})}{\kappa}$ or $d_1 = \frac{\sin^2(k\frac{d}{2})}{\kappa} = \frac{\cos^2(k\frac{d}{2} + \frac{\pi}{2})}{\kappa}$ for respectively even and odd solutions. As $\kappa \to 0$ when $E \to V$, $d_1 \to \infty$ and the probability of the particle to be outside tends to 100%. From the figure, we can see that the probability to be outside the well is very low for eigen-states of low energies.

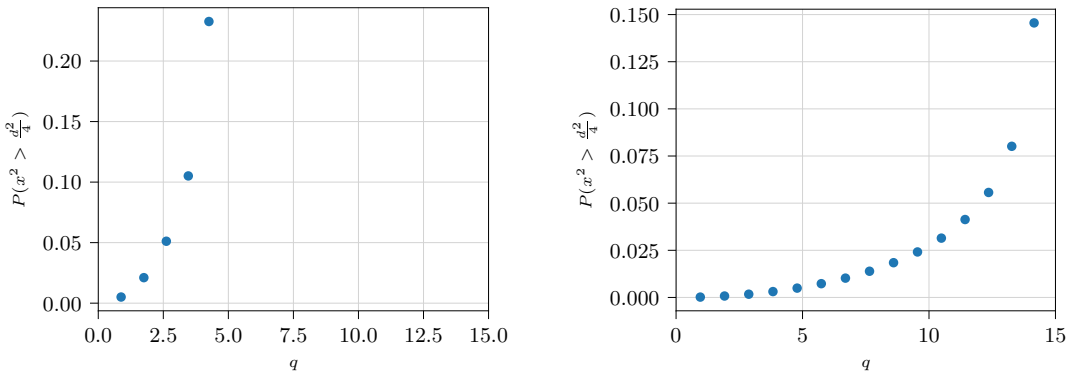

Figure 20: Probability of the particle to be outside of the well for $d = 200\mathring{A}$ and $V = 20meV$ (left) or $V = 200meV$ (right). It can become close to 100% if d and V are such that there are energy eigenvalues close to V. 0.15 means 15% for instance.

5.3.7 Higher energies

We only focused on solutions with Eigen-energies below V but note there are solutions with higher energies than V with wave functions that are sinusoidal in all regions but with different angular frequencies k. If regions (1) and (3) are infinitely large which is physical not possible but can be thought of as a limit case, there are an infinite number of solutions, on a continuum of energy above V.

5.4 Particle in a box

This section extends results of infinite well to three dimensions. This is another theoretical system but it is very useful as it yields to the De Broglie equation in 3D that is important when introducing the notion of effective masses for instance. We consider a particle in the box of fig. 21 with zero potential inside and infinite potential outside.
Inside the box, Schrödinger equation reads

$$-\frac{\hbar^2}{2m}\left(\frac{\partial^2\psi(\mathbf{r})}{\partial x^2}+\frac{\partial^2\psi(\mathbf{r})}{\partial y^2}+\frac{\partial^2\psi(\mathbf{r})}{\partial z^2}\right)=E\psi(\mathbf{r})$$

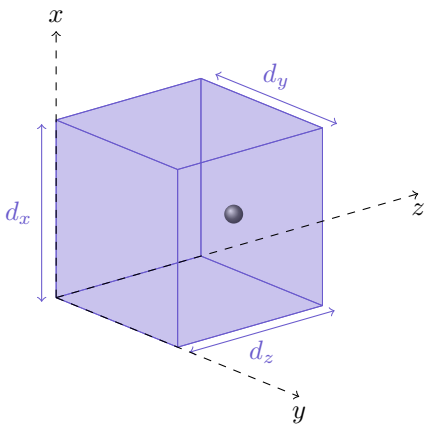

Figure 21: Schematic of particle in a box model.

With a classical separation of variables, we look for solutions defined as the product of individual functions of x, y and z:

$$\psi(\mathbf{r})=\psi_x(x)\psi_y(y)\psi_z(z)$$

The second order derivative of ψ w.r.t. x are

$$\frac{\partial^2\psi(\mathbf{r})}{\partial x^2}=\frac{\partial^2\psi_x(x)}{\partial x^2}\psi_y(y)\psi_z(z)$$

and we can find symmetric expressions for y and z. Replacing those in the equation and dividing by $\psi_x(x)\psi_y(y)\psi_z(z)$ gives

$$-\frac{\hbar^2}{2m}\frac{1}{\psi_x(x)}\frac{\partial^2\psi_x(x)}{\partial x^2}-\frac{\hbar^2}{2m}\frac{1}{\psi_y(y)}\frac{\partial^2\psi_y(y)}{\partial y^2}-\frac{\hbar^2}{2m}\frac{1}{\psi_z(z)}\frac{\partial^2\psi_z(z)}{\partial z^2}=E$$

As E is constant, it is not a function of x, y or z. Therefore, the left terms of the equation also must be constant, that we shall note E_x, E_y and E_z with $E_x+E_y+E_z=E$. Therefore, the equation is rewritten as three equations:

$$\begin{aligned}
-\frac{\hbar^2}{2m}\frac{\partial^2\psi_x(x)}{\partial x^2}&=E_x\psi_x(x)\\
-\frac{\hbar^2}{2m}\frac{\partial^2\psi_y(y)}{\partial y^2}&=E_y\psi_y(y)\\
-\frac{\hbar^2}{2m}\frac{\partial^2\psi_z(z)}{\partial z^2}&=E_z\psi_z(z)
\end{aligned}$$

We recognize the equation of an infinite well. Therefore the solution are given as

$$\psi(\mathbf{r}) = \sqrt{\frac{8}{V}} \sin\left(\frac{n_x \pi x}{d_x}\right) \sin\left(\frac{n_y \pi y}{d_y}\right) \sin\left(\frac{n_z \pi z}{d_z}\right)$$

where V is the volume $V = d_x d_y d_z$. Finally, the total energy is given by the De Broglie equation:

$$E = E_x + E_y + E_z = \frac{\hbar^2 \pi^2}{2m} \left(\frac{n_x^2}{d_x^2} + \frac{n_y^2}{d_y^2} + \frac{n_z^2}{d_z^2}\right) \tag{5.5}$$

Therefore, the energy can take only discrete values, some of which might be degenerate as there can be different wave functions, i.e. different choices of (n_x, n_y, n_z), for the same energy.

5.5 Multiple wells in one dimension

The python code associated to this section in DiscreteEigen.py.
When we have to deal with more complex structures with multiple layers of different bandgaps and effective masses, it is generally not possible to look for analytical solutions. We need to resort to discretization of the space and numerical methods.
This section describes such methods in the one-dimensional case that will be useful for multi-layers quantum wells. We consider a structure of P layers of effective mass m_p, potential V_p and width d_p, starting from $x = 0$ to $x = d_x = \sum_p d_p$, with K wells of fig. 22. Wells are defined here as the regions where the potential is null.

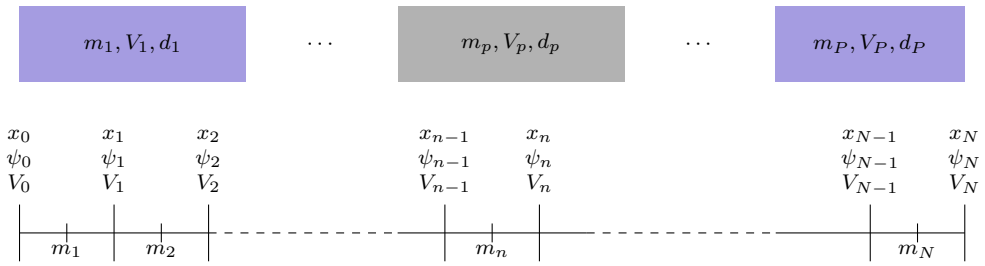

Figure 22: Multiple layers quantum well.

5.5.1 Discretization with constant mass

We want to solve the Schrödinger eq.

$$-\frac{\hbar^2}{2m} \frac{\partial^2 \psi}{\partial x^2} + V(x)\psi(x) = E\psi(x)$$

over the finite interval $[0, d_x]$. We cut the range into N intervals of equal width $l = \frac{d_x}{N}$ and obtain $N + 1$ points:

$$\forall i = 0, \cdots, N \quad \begin{cases} x_i = il \\ \psi_i = \psi(x_i) \\ V_i = V(x_i) \end{cases}$$

We approximate $\frac{\partial^2\psi}{\partial x^2}$ by finite differences as either:

$$\frac{\partial^2\psi}{\partial x^2} = \frac{\psi(x+l) - 2\psi(x) + \psi(x-l)}{l^2} + O(l^2) \tag{5.6}$$

$$= \frac{-\psi(x+2l) + 16\psi(x+l) - 30\psi(x) + 16\psi(x-l) - \psi(x-2l)}{12l^2} + O(l^4) \tag{5.7}$$

Results of this section will show that the accuracy is satisfactory with the approximation with three points and we will use it below. Dropping $O(l^2)$, the equation becomes

$$\forall i = 1, \cdots, N-1 \quad -\frac{\hbar^2}{2m}\frac{\psi_{i+1} - 2\psi_i + \psi_{i-1}}{l^2} + V_i\psi_i = E\psi_i$$

We set $\psi_0 = \psi_N = 0$ because the structure is bounded by barriers either

- with infinite potential at $x = 0$ and $x = d_x$.
- with finite potential but large enough so that the wave function vanishes in $e^{\pm\kappa(x-c)}$ at $x = 0$ and $x = d_x$ as we observed in fig. 19

Noting $a = -\frac{\hbar^2}{2ml^2}$ and $b_i = \frac{\hbar^2}{ml^2} + V_i$, the equation becomes

$$\forall i = 1, \cdots, N-1 \quad a\psi_{i-1} + b_i\psi_i + a\psi_{i+1} = E\psi_i$$

or in matrix form

$$\mathbf{H}\psi = E\psi$$

with

$$\mathbf{H} = \begin{pmatrix} b_1 & a & 0 & \cdots & 0 \\ a & b_2 & a & \cdots & 0 \\ 0 & \ddots & \ddots & \ddots & 0 \\ \vdots & \ddots & a & b_{N-2} & a \\ 0 & \cdots & 0 & a & b_{N-1} \end{pmatrix} \quad \text{and} \quad \psi = \begin{pmatrix} \psi_1 \\ \psi_2 \\ \vdots \\ \psi_{N-1} \end{pmatrix}$$

$\mathbf{H}$ is $(N-1)^2$ tri-diagonal symmetric, hence Hermitian, matrix. We want to solve for E, the possible eigen-energies, and ψ, their eigen-vectors, discrete versions of the wave functions. This is easily achieved with standard numerical procedures. We use scipy's linear algebra function *scipy.linalg.eigh_tridiagonal* based on LAPACK [16], that gives the $N-1$ solutions.

For the examples of this section, the Eigenvalues E_n of the matrix $\mathbf{H}$ are expressed as quantum numbers q_n s.t.

$$E_n = q_n^2 E_1^\infty$$

using E_1^∞ defined as in eq. 5.2 for infinite wells, computed with the average width of wells and the average effective mass when the mass of the particle is not constant. The energy E_1^∞ has no direct physical interpretation here. It can be simply viewed as a convenient scaling factor.

The code in Python is meant to be used with width of regions that are multiples of l. If not, numerical errors will be larger. Typically, one discretization interval per Angstrom works well (for widths that are integer numbers of $\mathring{A}$.)
At the junctions between two regions, the potential is taken at the mid-level between the potentials of the two regions. This improves the numerical accuracy and avoids unstable results due to rounding errors.

[16] scipy has eigenvalue routines based on LAPACK or ARPACK for tri-diagonal Hermitian, banded Hermitian, sparse and ordinary matrices. All algorithms propose to return the smallest (or the largest) values, but routines for sparse matrices are said to be slow for small eigenvalues.

Errors of the numerical procedure There are two main [17] sources of errors:

- The second order derivative is replaced by a finite difference of order $O(\frac{d_x^2}{N^2})$. We can clearly see that the error will decrease in N^2.
- We replaced the continuous problem with an infinite number of discrete solutions E_n, by a system with only $N-1$ solutions. Therefore, the solutions of the discretized system can not be exact, because the number of solutions is wrong to begin with.

Example of the infinite well As a toy example, we test the algorithm and its implementation in the code on an single infinite well of 200$\mathring{A}$ with $V=0$ and $N=50$. Results are given in fig. 23 where the 49 eigenvalues E_n are expressed in quantum numbers defined as $\sqrt{\frac{E_n}{E_1^\infty}}$. The chart on the left shows that the first few quantum numbers are close to their expected integer values, while the discretization error becomes large beyond $n=10$, or about $\frac{N}{5}$. With $N=1000$, we obtain the exact same results, with $\frac{N}{5}$ accurate numbers as depicted by fig. 24.
We do not need to define a criteria for accuracy. **In practice, we will make use of only the first few eigenvalues because others will have no impact in the range of wave-length for the spectrum we consider.**
The algorithm is very fast, but we can use *scipy.linalg.eigh_tridiagonal* that only computes the eigenvalues (we do not need the eigenvectors when computing density of states) up to a range.
The eigenvectors computed by the algorithm are not necessarily normalized in probability but they can be adjusted by a factor, because, if ψ_n is an eigenvector, so is $\alpha\psi_n$ for any $\alpha \neq 0$. We normalize them by computing the total probability with the trapezoidal rule that simplifies with $\psi_0=\psi_N=0$:

$$l\left(\frac{1}{2}\psi_0^2+\sum_{n=1}^{N-1}\psi_n^2+\frac{1}{2}\psi_N^2\right)=l\sum_{n=1}^{N-1}\psi_n^2=l\|\psi\|^2=1$$

Hence $\alpha=\frac{1}{\sqrt{l}\|\psi\|}$

5.5.2 Non constant effective masses

Borrowing from chapters 2 and 3 of [16], when the mass is not constant across heterojunctions of layers, the momentum operator must be defined as

$$\frac{\hbar^2}{2}\frac{\partial}{\partial x}\left(\frac{1}{m(x)}\frac{\partial}{\partial x}\right) \tag{5.8}$$

to ensure it remains Hermitian.
Defining the Hamiltonian $\mathcal{H}^{(0)}$ by

$$\mathcal{H}^{(0)}=-\frac{\hbar^2}{2}\frac{\partial}{\partial x}\left(\frac{1}{m(x)}\frac{\partial}{\partial x}\right)+V(x) \tag{5.9}$$

where the index (0) will be useful in sect. 5.6, the Schrödinger equation becomes

$$\mathcal{H}^{(0)}\psi(x)=E\psi(x) \tag{5.10}$$

Likewise, the boundary condition on the continuity of $\frac{\partial\psi(x)}{\partial x}$ at junctions must be replaced by the continuity of $\frac{1}{m(x)}\frac{\partial\psi(x)}{\partial x}$ instead. Note that imposing these conditions would only be necessary if we

[17] Other sources include the processor precision and the convergence of the Eigenvalue algorithm.

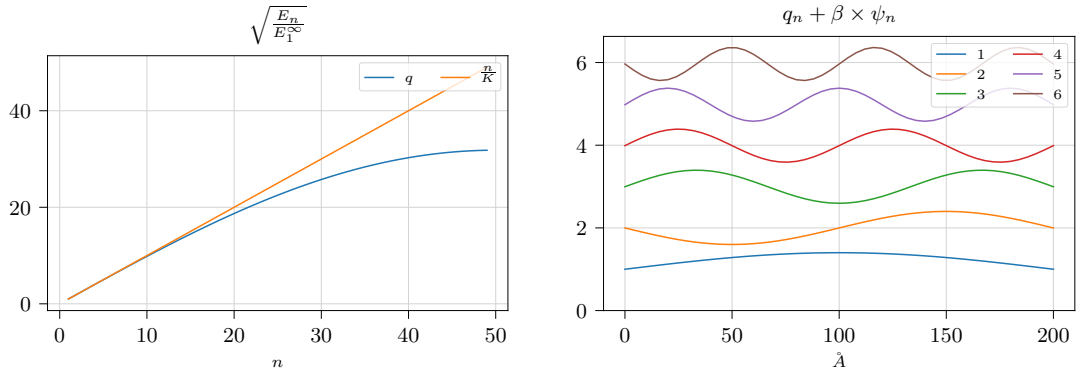

Figure 23: Eigenvalues expressed in quantum numbers (left) and the first few Eigenvectors (right) for an infinite well with null well potential $V = 0$, $d_x = 200\mathring{A}$ and 50 discretization steps. The first few quantum numbers $\sqrt{\frac{E_n}{E_1^\infty}}$ are close to their theoretical expected integer values. Errors increase beyond n =10. Lines on the right-hand chart are the wave functions scaled by an ad-hoc (simply chosen arbitrarily to avoid lines to overlap) factor and translated up by their quantum number: $q_n + 0.4\sqrt{\frac{d}{2}}\psi_n(x)$

tried to solve the problem by linking analytical solutions of contiguous regions. It is not necessary when solving numerically by the Eigenvalue decomposition algorithm on the discretized set-up, but we will check they are met.

Now, we need to approximate the new kinetic operator of eq. 5.8 by finite differences. Developing its expression omitting the factor $\frac{\hbar^2}{2}$, gives:

$$\frac{\partial}{\partial x}\left(\frac{1}{m(x)}\frac{\partial}{\partial x}\right) = -\frac{1}{m^2(x)}\frac{\partial m(x)}{\partial x}\frac{\partial}{\partial x} + \frac{1}{m(x)}\frac{\partial^2}{\partial x^2}$$

As $m(x)$ jumps by steps, its derivatives at junctions is an infinite Dirac-delta function. Therefore, we can not apply the same Taylor expansion (finite difference) as in the prior section. Instead, this issue is circumvented by directly taking a Taylor expansion of eq. 5.8 as follows:

$$\begin{aligned}\frac{\partial}{\partial x}\left(\frac{1}{m(x)}\frac{\partial \psi}{\partial x}\right) &\approx \frac{1}{l}\left(\frac{1}{m(x+\frac{l}{2})}\left.\frac{\partial \psi}{\partial x}\right|_{x+\frac{l}{2}} - \frac{1}{m(x-\frac{l}{2})}\left.\frac{\partial \psi}{\partial x}\right|_{x-\frac{l}{2}}\right) \\ &\approx \frac{1}{l^2}\left(\frac{1}{m(x+\frac{l}{2})}(\psi(x+l)-\psi(x)) - \frac{1}{m(x-\frac{l}{2})}(\psi(x)-\psi(x-l))\right)\end{aligned}$$

The Schrödinger equation is rewritten as, $\forall i = 1, \cdots, N-1$

$$-\frac{\hbar^2}{2l^2}\left(\frac{1}{m(x_i+\frac{l}{2})}(\psi_{i+1}-\psi_i) - \frac{1}{m(x_i-\frac{l}{2})}(\psi_i-\psi_{i-1})\right) + V_i\psi_i = E\psi_i$$

or

$$-\frac{\hbar^2}{2l^2}\left(\frac{\psi_{i+1}}{m(x_i+\frac{l}{2})} + \frac{\psi_{i-1}}{m(x_i-\frac{l}{2})}\right) + \psi_i\left(V_i + \frac{\hbar^2}{2l^2}\left(\frac{1}{m(x_i+\frac{l}{2})} + \frac{1}{m(x_i-\frac{l}{2})}\right)\right) = E\psi_i$$

Noting

$$\forall i = 1, \cdots, N \quad m_i = m\left((i-\frac{1}{2})l\right)$$

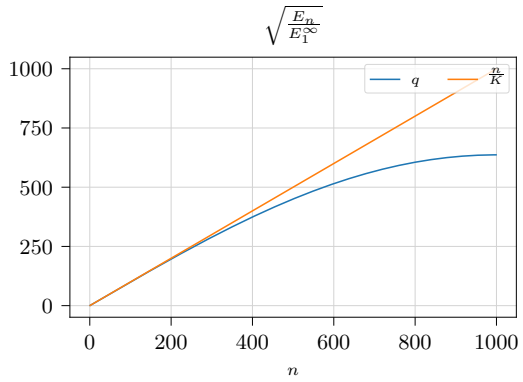

Figure 24: Eigenvalues with 1000 discretization steps.

and

$$\forall i = 1, \cdots, N-1, \quad a_i = -\frac{\hbar^2}{2m_i l^2} \quad \text{and} \quad b_i = V_i + \frac{\hbar^2}{2l^2}\left(\frac{1}{m_i} + \frac{1}{m_{i+1}}\right)$$

(we have one more m_i than x_i) the equation reads

$$\forall i = 1, \cdots, N-1 \quad a_i\psi_{i-1} + b_i\psi_i + a_{i+1}\psi_{i+1} = E\psi_i$$

or

$$\mathbf{H}^{(0)}\psi = E\psi \tag{5.11}$$

with

$$\mathbf{H}^{(0)} = \begin{pmatrix} b_1 & a_2 & 0 & \cdots & 0 \\ a_2 & b_2 & a_3 & \cdots & 0 \\ 0 & \ddots & \ddots & \ddots & 0 \\ \vdots & \ddots & a_{N-2} & b_{N-2} & a_{N-1} \\ 0 & \cdots & 0 & a_{N-1} & b_{N-1} \end{pmatrix} \quad \text{and} \quad \psi = \begin{pmatrix} \psi_1 \\ \psi_2 \\ \vdots \\ \psi_{N-1} \end{pmatrix}$$

$\mathbf{H}^{(0)}$ is still symmetric. Note that we do not use a_1 and a_N because they apply to ψ_0 and ψ_N which are null.

Single finite well The wave functions are illustrated in fig. 25. With a constant mass, they are very close (the sign of ψ does not matter) to that of the semi-analytical solutions of fig. 23 with an infinite well. They are even closer when we increase the width of barriers (not shown here). With a higher mass in the barriers, the quantum numbers get closer to the integer values of an infinite well.
In fig. 26, we confirm that $\frac{\partial\psi_n}{\partial x}$ is not continuous at junctions when the mass is discontinuous, whereas $\frac{1}{m}\frac{\partial\psi_n}{\partial x}$ is continuous as expected. This shows that the numerical procedure is fairly accurate and robust because the continuity condition at junctions are not imposed in the algorithm. In all cases, the second order derivative $\frac{\partial^2\psi_n}{\partial x^2}$ jumps because of the jumps of potential. Looking at the Schrödinger equation, it is obvious that $\frac{\partial^2\psi_n}{\partial x^2}$ must have the same discontinuity as V given than ψ is continuous.

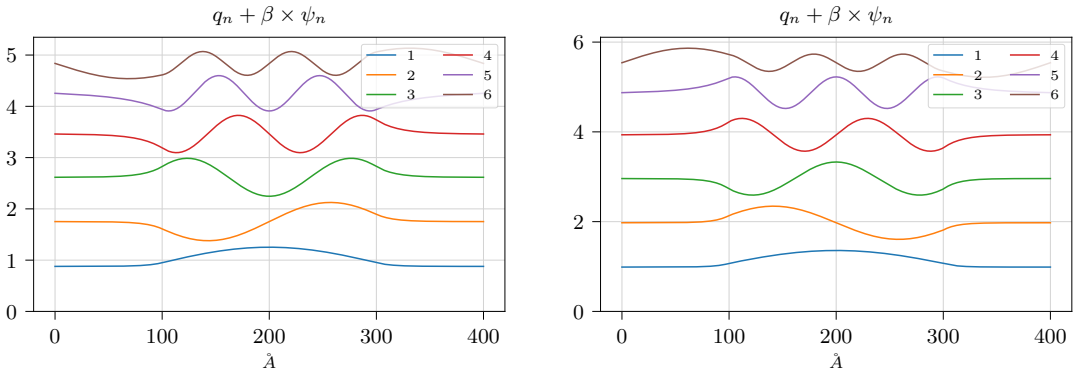

Figure 25: Eigen-solutions for a single well of $200\mathring{A}$ bounded by barriers of $100\mathring{A}$ at $V = 20\ meV$. The left-hand chart is with constant mass of m_e. It is identical to the left chart of fig. 19, except that it shows a 6^{th} solution that is above the q_V. The right-hand chart assumes a mass of $1.5m_e$ in the barriers. Discretization is done with two points per angstrom. With a higher mass in the barriers, the quantum numbers get closer to the integer values of an infinite well while the wave functions have very similar shapes. They are inverted but we need to keep in mind that ψ and $-\psi$ correspond to the same state.

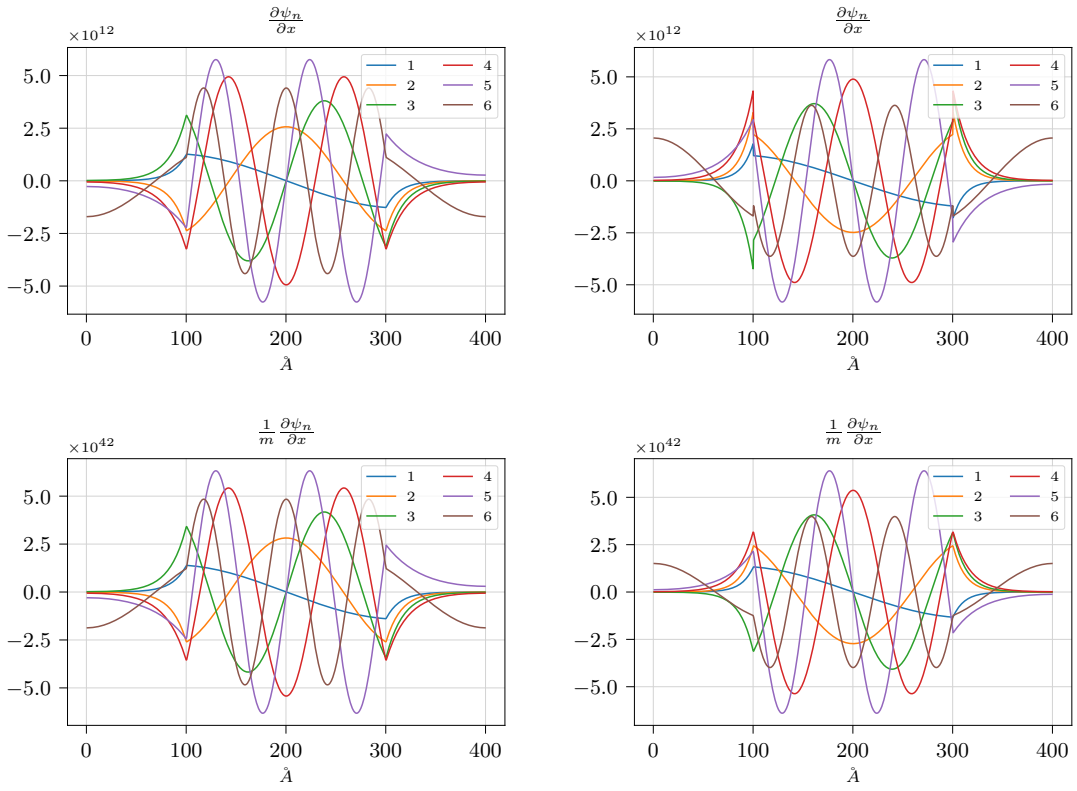

Figure 26: $\frac{\partial \psi_n}{\partial x}$ (top) and $\frac{1}{m}\frac{\partial \psi_n}{\partial x}$ (bottom) for the single well with constant (left) and non-constant masses (right)

Multiple wells We now test the algorithm on structures with multiple wells. For the sake of the examples, wells and barriers are resp. $200\mathring{A}$ and $100\mathring{A}$ wide. Barriers potential is at 20 meV. We observe on fig. 27 that Eigen-energies are degenerate in as many states as there are wells. [18] Therefore, we will need to account for this multiplicity in the calculation of density of states.
The degeneracy of Eigenvalues is emphasized in fig. 28. It is worth noting that expressing the energies as squared quantum numbers of E_1^∞ computed with the average well width was a nice choice. We also observe that the degenerate quantum numbers are the same for any number of wells, because determined solely by the barrier potential, the mass and the width of the wells.

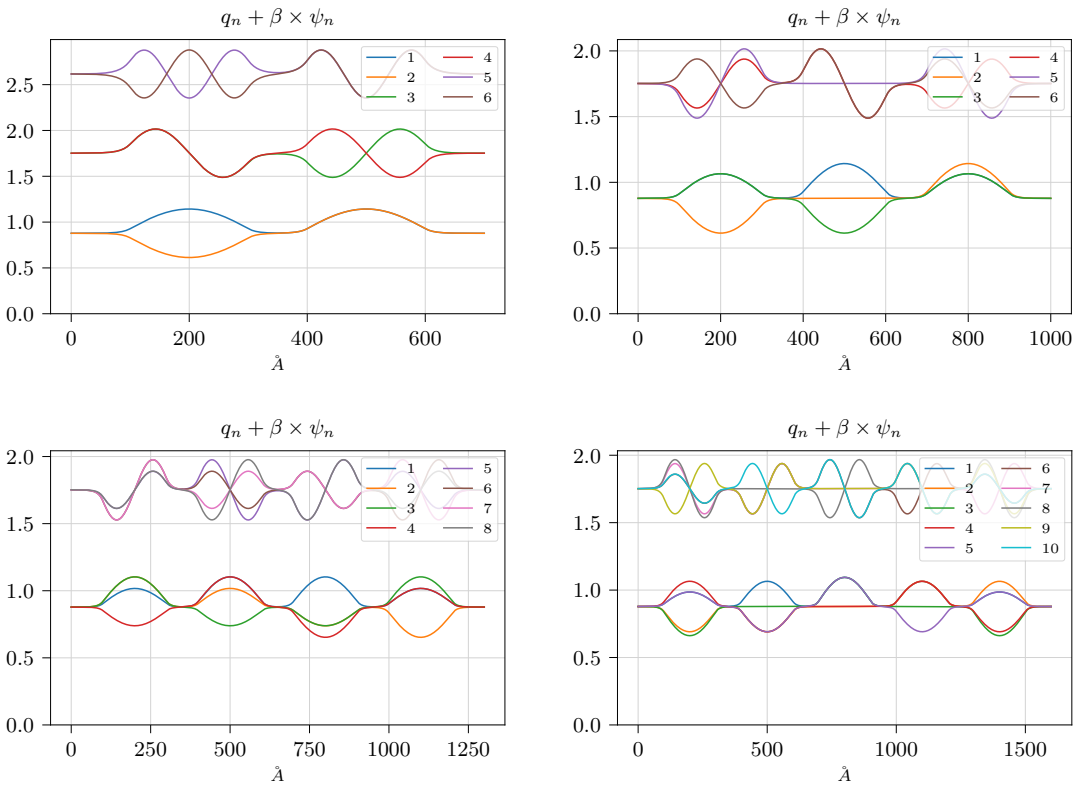

Figure 27: From left to right, top to bottom: Wave functions of multiple wells with 2, 3, 4 or 5 equal wells at 0 eV of width $200\mathring{A}$ and $100\mathring{A}$ barriers at $V = 20$ meV. In the first chart, we chose to display the first 3 degenerated eigenvalues, while we shows only the first 2 in the other charts. We can see that the first degenerated eigenvalue is the same in all cases.

The degeneracy is due to the very regular structures in these examples and to the wide inter-well barriers. Retrospectively, it is easy to see that, if barriers between wells were very wide, the multiple well would simply behave as the sum of independent wells. As a test, fig. 29 shows how the first four eigenvalues of a quadruple well converge to the first eigenvalue of a single well when the barriers between them grow. This demonstrate that the degeneracy coming is from the larger barriers: for thin barriers, it does not happen.
Note that we can not expect that eigenvalues of multiple wells with wells or barriers with different masses or widths will exhibit multiplicity.

[18] It must be easy to prove but this is not the object of this work and we will leave it aside.

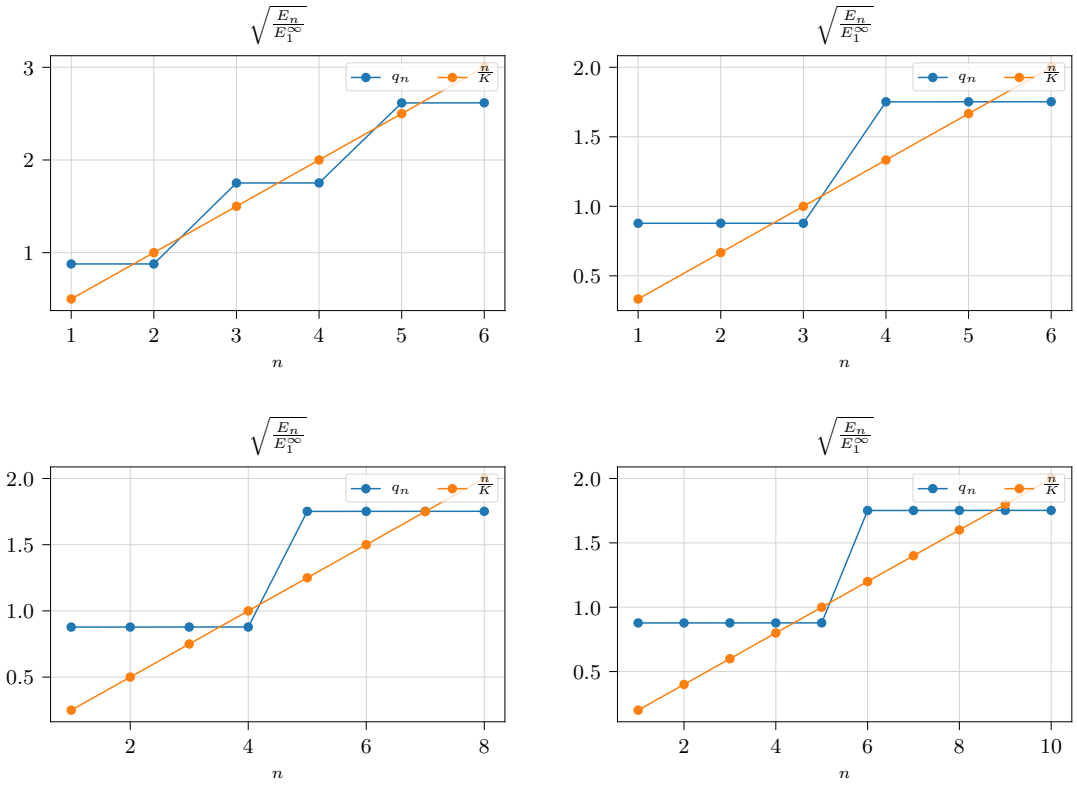

Figure 28: Degeneracy of the first $2K$ quantum numbers for wells with K wells and $K = 2, \cdots, 5$. Wells are $200\mathring{A}$ wide with $100\mathring{A}$ barriers at $V = 20meV$.

5.6 Density of states of MQW in three dimensions

We have so far considered the simplified case of one dimension. However, it is impossible to derive the density of state in three dimensions from the one-dimensional case because the energy cannot be written as the sum of energy components from axes x, y and z as this was the case for a particle in a box. We must work directly in three dimensions. Besides, we must account for the anisotropy of holes effective masses.

In this section, we derive some approximations of the Eigen-energies and the density of states in the most accurate expression of the Schrödinger equation in 3D. Note that the density of states for quantum well of sect. 4 assumes a constant mass and is only valid for single quantum wells. It is interesting because it provides simple insights as to how the density is expressed but it is not accurate enough for complex structures.

As the mass is discontinuous at hetero-junctions on the axis x, we must replace $\mathbf{p}^2$ by $\mathbf{p} \cdot \frac{1}{m}\mathbf{p}$ and the Schrödinger equation becomes

$$-\frac{\hbar^2}{2}\frac{\partial}{\partial x}\left(\frac{1}{m^{<100>}(x)}\frac{\partial}{\partial x}\right)\psi(\mathbf{r}) - \frac{\hbar^2}{2m^t(x)}\left(\frac{\partial^2\psi(\mathbf{r})}{\partial y^2} + \frac{\partial^2\psi_(\mathbf{r})}{\partial z^2}\right) + V(x)\psi(\mathbf{r}) = E\psi(\mathbf{r}) \quad (5.12)$$

where $m^{<100>}$ is the effective mass in the $k_{<100>}$ direction in the $\mathbf{k}$ space, m^t is the effective in the transversal plane of $k_{<100>}$ and we assume the bands are parabolic at the Γ point of interest.

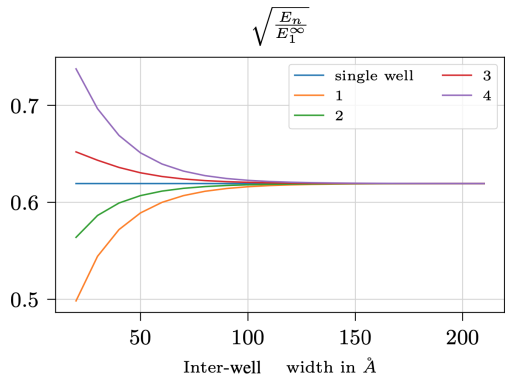

Figure 29: First four quantum numbers of a quadruple GaAs /$Al_{0.2}Ga_{0.8}$As well versus the width of barriers between wells. Wells and the most outside barriers are resp. $80\mathring{A}$ and $200\mathring{A}$ wide. The quantum numbers of the quadruple well converge to the first quantum number of a single well when the inter-well width widens, as the multiple well behaves as four independent wells.

As for the particle in a box, we look for solutions expressed as $\psi = \psi_x\psi_y\psi_z$. Replacing ψ by this product, multiplying by $m^t(x)$, dividing by ψ and re-arranging terms gives

$$-\frac{\hbar^2}{2}\frac{m^t(x)}{\psi_x}\frac{\partial}{\partial x}\frac{1}{m^{<100>}(x)}\frac{\partial\psi_x}{\partial x} + m^t(x)\left(V(x) - E\right) = \frac{\hbar^2}{2}\left(\frac{1}{\psi_y}\frac{\partial^2\psi_y}{\partial y^2} + \frac{1}{\psi_z}\frac{\partial^2\psi_z}{\partial z^2}\right)$$

The term on the left is only function of x while terms on the right are only functions of y and z, therefore they must be equal to a constant that we choose to note $-C$ for convenience. We look for the values of C and E such that there is a solution ψ that satisfies boundary conditions. First, let's look at the plane y, z. As the right term of the equation is the sum of two functions that only depend respectively of y and z, each function must be constant too. Splitting C in $C = C_y + C_z$, we get

$$-\frac{\hbar^2}{2}\frac{\partial^2\psi_y}{\partial y^2} = C_y\psi_y$$
$$-\frac{\hbar^2}{2}\frac{\partial^2\psi_z}{\partial z^2} = C_z\psi_z$$

This is similar to the set of equations obtained for the particle in a box, except that the mass is not in the equation and that C_y and C_z are not necessarily positive.

If C_y was negative, ψ_y would to be of the from $ce^{\kappa y} + de^{-\kappa z}$ with $\kappa = \sqrt{-\frac{2C_y}{\hbar^2}}$. We can easily show that conditions with $\psi_y = 0$ at boundaries impose that $c = d = 0$, hence, $\psi_y = 0$ everywhere, which is possible only if the particle is nowhere. Hence, C_y must be positive and so must C_z. Therefore, we have the usual sine wave functions with quantization of C_y and C_z that we rename C_{n_y} and C_{n_z} with $(n_y, n_z) \in \mathbb{N}^{*2}$:

$$C_{n_y} = n_y^2\frac{\hbar^2\pi^2}{2d_y^2}, \quad C_{n_z} = n_z^2\frac{\hbar^2\pi^2}{2d_z^2}$$

For a given pair n_y, n_z, the equation on x after multiplication by $\frac{\psi_x}{m^t(x)}$, reads

$$-\frac{\hbar^2}{2}\frac{\partial}{\partial x}\frac{1}{m^{<100>}(x)}\frac{\partial\psi_x}{\partial x} + \left(V(x) + \frac{C_{n_y} + C_{n_z}}{m^t(x)}\right)\psi_x = E\psi_x \tag{5.13}$$

which is the same equation as for the MQW with variable mass in one dimension of sect. 5.5, except that we modify the potential in each region.
We can discretize the equation and obtain one linear system for each pair (n_y, n_z):

$$(\mathbf{H}^{(0)} + \left(C_{n_y} + C_{n_z}\right)\mathbf{D})\psi_x = E\psi_x \tag{5.14}$$

where $\mathbf{H}^{(0)}$ is the same as in sect. 5.5.2 but evaluated with $m^{<100>}$ and $\mathbf{D}$ is a diagonal matrix whose elements are the inverse transversal masses $\frac{1}{m^t(il)}$ at the points $x_i = il$. Even though we can numerically solve each of the systems, combining the solutions to derive an expression of the density of states is not straightforward. We need to simplify the problem with some approximations and we will consider two approaches in the next two sections.

5.6.1 Constant average mass approximation

As $\mathbf{H}^{(0)}$ and $\mathbf{D}$ do not commute (i.e. they do not share a basis in the Hilbert space of states), there is no expression[19] for the eigenvalues of the combination of the matrices. However, if the transversal mass across layers was equal to some constant m^*, $\mathbf{D}$ would be $\frac{1}{m^*}$ times the identity matrix and the eigenvalues of the system would be the eigenvalues of $\mathbf{H}^{(0)}$, $E^{(0)}_{n_x}$ independent of n_y and n_z, shifted up by $\frac{C_{n_y}+C_{n_z}}{m^*}$. Now, nothing prevent us from using a different m^* for each n_x. In particular, it sounds intuitively a good idea to apply a mass weighted by the probability density of the particle as in [65] and cited in [87], that is:

$$m^*_{n_x} = \int m^t(x)|\psi^{(0)}_{n_x}|^2 dx \tag{5.15}$$

where $\psi^{(0)}_{n_x}$ is the solution n_x for $\mathbf{H}^{(0)}$ and the integral can be computed by a trapezoidal method. (after we make sure that eigenvectors are normalized.)
We can justify this choice by the fact that, if barriers were with infinite potential and wells of the same alloy, the average would be equal to the average effective mass in the wells as the particle can not escape ($|\psi^{(0)}_{n_x}|^2 = 0$ in the barriers.). With this approximation, the energy is given as

$$E(n_x, n_y, n_z) = E^{(0)}_{n_x} + \frac{C_{n_y} + C_{n_z}}{m^*_{n_x}} \tag{5.16}$$

In order to derive the density of states, we proceed similarly as in 4.3.4. The number of states up to quantum numbers n_y and n_z is

$$N_s(n_y, n_z) = \frac{\pi}{2}\left(n_y^2 + n_z^2\right)$$

Therefore $C_{n_y} + C_{n_z}$ reads, assuming $d_y = d_z = d$ for sake of simplicity but without loss of generality,

$$C_{n_y} + C_{n_z} = \frac{\hbar^2\pi^2}{2}\left(\frac{n_y^2}{d_y^2} + \frac{n_z^2}{d_z^2}\right) = \frac{\hbar^2\pi^2}{2d^2}\frac{2}{\pi}N_s(n_y, n_z) = \frac{\hbar^2\pi}{d^2}N_s(n_y, n_z)$$

Multiplying and dividing by $m^*_{n_x}$ and solving for $N_s(n_y, n_z)$ yields to

$$N_s(n_y, n_z) = \frac{m^*_{n_x}d^2}{\pi\hbar^2}\frac{C_{n_y} + C_{n_z}}{m^*_{n_x}}$$

[19] In 1962, Horn conjectured some inequalities for eigenvalues of sums of two Hermitian matrices, which often arise in quantum mechanics. The conjecture was proven in 1999 (c.f. [86]) but it is of no use here.

For any given n_x, the number of states up to n_y and n_z is $N_s(n_y, n_z)$ and the energy is up to $E(n_x, n_y, n_z)$. Replacing $\frac{C_{n_y}+C_{n_z}}{m^*_{n_x}}$ by $E - E^{(0)}_{n_x}$ from eq. 5.16, the number of states up to the energy E is

$$N_s(E, n_x) = \frac{m^*_{n_x} d^2}{\pi\hbar^2} f(E, n_x) \tag{5.17}$$

with the function f defined as $f(E, n_x) = \left(E - E^{(0)}_{n_x}\right)^+$.
Summing over all n_x, the number of states up to E is

$$N_s(E) = \sum_{n_x=1,\cdots} \frac{m^*_{n_x} d^2}{\pi\hbar^2} f(E, n_x) \tag{5.18}$$

Dividing by the volume $d^2 d_x$ where d_x is the sum of the widths of all layers (wells and barriers), and deriving versus E gives the density of states in $\mathrm{J}^{-1}\mathrm{m}^{-3}$

$$\begin{aligned}\rho(E) = \sum_{n_x=1,\cdots} \frac{m^*_{n_x}}{\pi\hbar^2 d_x} \frac{df(E, n_x)}{dE} &= \frac{1}{\pi\hbar^2 d_x} \sum_{n_x=1,\cdots} m^*_{n_x} \frac{df(E, n_x)}{dE} \\ &= \sum_{n_x=1,\cdots} \frac{1}{\pi\hbar^2 d_x} m^*_{n_x} \frac{df(E, n_x)}{dE} = \sum_{n_x=1,\cdots} \rho(E, n_x)\end{aligned} \tag{5.19}$$

with $\rho(E, n_x)$ defined as $\frac{1}{\pi\hbar^2 d_x} m^*_{n_x} \frac{df(E,n_x)}{dE}$.

Important note: We could divide by a volume different from $d^2 d_x$. In particular, one may prefer to divide by the volume of wells instead, in particular when considering a photon beam confined to wells. The density of states depends on the geometry of the device only because the geometry determines the boundary conditions of a differential equation. Without dividing by the volume, it is already a density (in J^{-1}). The subsequent division by a volume converts it to a density per energy and per unit of volume in $J^{-1}m^{-3}$ and is meant to express the gain of the device by unit of volume.

To conclude and summarize, every steps in this derivation are exact, except that we approximated the eigenvalues of the Hamiltonian by approximating the mass in the matrix $\mathbf{D}$ as a constant, while we applied variables masses for the eigenvalues of $\mathbf{H}^{(0)}$.

5.6.2 Perturbation

Instead, we can view the Hamiltonian of eq. 5.13 as perturbed version of $\mathcal{H}^{(0)}$ and apply first or second order perturbation method.
Eq. 5.13 can be written as

$$\left(\mathcal{H}^{(0)} + \frac{C_{n_y} + C_{n_z}}{m^t(x)}\right) \psi_x = \mathcal{H}\psi_x = E\psi_x \tag{5.20}$$

and its Hamiltonian as

$$\mathcal{H} = \mathcal{H}^{(0)} + \lambda\mathcal{H}'$$

with $\lambda = C_{n_y} + C_{n_z}$ and $\mathcal{H}' = \frac{1}{m^t(x)}$.
We can apply usual results of perturbation methods for this perturbation of the Hamiltonian, that is, we

look for solutions of the form

$$E = E^{(0)} + \lambda E^{(1)} + \lambda^2 E^{(2)} + \cdots$$
$$\psi_x = \psi_x^{(0)} + \lambda \psi_x^{(1)} + \lambda^2 \psi_x^{(2)} + \cdots$$

The superscript $^{(2)}$ for instance in the terms $E^{(2)}$ and $\psi_x^{(2)}$ denotes second-order terms, whereas the superscript ^{2} in λ^2 is simply the power 2 of λ.

Defining the unperturbed equation as

$$\mathcal{H}^{(0)}\psi_x = E\psi_x \tag{5.21}$$

we note its n_x^{th} solution by $E_{n_x}^{(0)}$ and $\psi_{n_x}^{(0)}$ [20].
Keep in mind that the solutions of the unperturbed equation are solved numerically by the procedure described in sect. 5.5.2 and that they are the solutions of the perturbed equation at order 0.

First order Following sect. 3.5 of [66], the n_x^{th} first order solution is given as

$$E_{n_x} = E_{n_x}^{(0)} + \lambda E_{n_x}^{(1)} \tag{5.22}$$

where $E_{n_x}^{(1)} = \mathcal{H}'_{n_x,n_x}$ and $\mathcal{H}'_{n_x,n_x} \in \mathbb{R}$ is the matrix element (i.e. the average value of $\mathcal{H}'$)

$$\mathcal{H}'_{n_x,n_x} = \left\langle \psi_{n_x}^{(0)} \middle| \mathcal{H}' \middle| \psi_{n_x}^{(0)} \right\rangle = \int \psi_{n_x}^{(0)*} \frac{1}{m^t(x)} \psi_{n_x}^{(0)} dx = \int \frac{1}{m^t(x)} |\psi_{n_x}^{(0)}|^2 dx$$

Defining $m^*_{n_x}$ from the probability-density-weighted average inverse mass as

$$\frac{1}{m^*_{n_x}} = \int \frac{1}{m^t(x)} |\psi_{n_x}^{(0)}|^2 dx \tag{5.23}$$

and replacing λ by its value $C_{n_y} + C_{n_z}$, the first order solution of eq. 5.22 become

$$E(n_x, n_y, n_z) = E_{n_x}^{(0)} + \frac{C_{n_y} + C_{n_z}}{m^*_{n_x}}$$

This is the same expression as eq. 5.16 of the prior section. This means that the first order approximation is equivalent to assuming a constant mass for the matrix $\mathbf{D}$ but the mass is computed from the average inverse mass instead, so as to obtain an error in λ^2. This does not necessarily mean that the new definition of the mass is better, but simply that we know the error we make. At last, it is easy to show that the density of states is still given by eq. 5.19.

Second order We derive here the second order approximation and find some relatively *nice* expressions. They are not implemented in the Python library because this is a bit tedious and second order accuracy is probably not necessary given that the model representation of the many physical phenomena is imperfect to begin with.
Still following sect. 3.5 of [66], the second order approximation is

$$E_{n_x} = E_{n_x}^{(0)} + \lambda E_{n_x}^{(1)} + \lambda^2 E_{n_x}^{(2)} \tag{5.24}$$

[20] We should rather note it $\psi_{x,n_x}^{(0)}$ to remind that this is the ψ_x part of $\psi = \psi_x \psi_y \psi_z$, but we drop the x subscript for ease of notation.

with the second order term

$$E_{n_x}^{(2)} = \sum_{m \neq n_x} \frac{\mathcal{H}'_{m,n_x} \mathcal{H}'_{n_x,m}}{E_{n_x}^{(0)} - E_m^{(0)}}$$

and

$$\mathcal{H}'_{m,n_x} = \left\langle \psi_m^{(0)} \middle| \mathcal{H}' \middle| \psi_{n_x}^{(0)} \right\rangle = \int \frac{1}{m^t(x)} \psi_m^{(0)^*} \psi_{n_x}^{(0)} dx$$

It is worth to note the following:

- $E_{n_x}^{(2)}$ takes into account of the overlap of the all wave functions (of order 0) $\psi_m^{(0)}$ for $m \neq n_x$ with the wave function $\psi_{n_x}^{(0)}$ due to the operator $\mathcal{H}'$.
- The inner product $\left\langle \psi_m^{(0)} \middle| \psi_{n_x}^{(0)} \right\rangle = \int \psi_m^{(0)^*} \psi_{n_x}^{(0)} dx$ is equal to 1 in $m = n_x$ and null otherwise because ψ_m and ψ_{n_x} are orthonormal solutions of the unperturbed equation, but $\mathcal{H}'_{m,n_x}$ is different.

Defining $m_{m,n_x}^{*2} = \left(\mathcal{H}'_{m,n_x} \mathcal{H}'_{n_x,m}\right)^{-1}$, eq. 5.24 gives

$$E = E_{n_x}^{(0)} + \left(C_{n_y} + C_{n_z}\right) \frac{1}{m_{n_x}^*} + \left(C_{n_y} + C_{n_z}\right)^2 \sum_{m \neq n_x} \frac{1}{m_{m,n_x}^{*2}} \frac{1}{E_{n_x}^{(0)} - E_m^{(0)}}$$

Replacing $C_{n_y} + C_{n_z}$ by its expression in the number of states N_s, we obtain the quadratic equation

$$a(n_x) N_s^2(n_y, n_z) + b(n_x) N_s(n_y, n_z) + c(E, n_x) = 0$$

with

$$a(n_x) = \frac{\hbar^4 \pi^2}{d^4} \sum_{m \neq n_x} \frac{1}{m_{m,n_x}^{*2}} \frac{1}{E_{n_x}^{(0)} - E_m^{(0)}}, \quad b(n_x) = \frac{\hbar^2 \pi}{d^2} \frac{1}{m_{n_x}^*}, \quad c(E, n_x) = E_{n_x}^{(0)} - E$$

and the discriminant.

$$\Delta = \frac{\hbar^4 \pi^2}{d^4} \left(\frac{1}{m_{n_x}^{*2}} + 4(E - E_{n_x}^{(0)}) \sum_{m \neq n_x} \frac{1}{m_{m,n_x}^{*2}} \frac{1}{E_{n_x}^{(0)} - E_m^{(0)}} \right)$$

The solutions $N_s(E, n_x)$ of the quadratic equation are

$$N_s(E, n_x) = \frac{-\frac{\hbar^2 \pi}{d^2} \frac{1}{m_{n_x}^*} \pm \frac{\hbar^2 \pi}{d^2} \left(\frac{1}{m_{n_x}^{*2}} + 4(E - E_{n_x}^{(0)}) \sum_{m \neq n_x} \frac{1}{m_{m,n_x}^{*2}} \frac{1}{E_{n_x}^{(0)} - E_m^{(0)}} \right)^{\frac{1}{2}}}{2 \frac{\hbar^4 \pi^2}{d^4} \sum_{m \neq n_x} \frac{1}{m_{m,n_x}^{*2}} \frac{1}{E_{n_x}^{(0)} - E_m^{(0)}}}$$

Multiplying the denominator and numerator by $m_{n_x}^{*2}$, $N_s(E, n_x)$ can be expressed using the same eq. as 5.17

$$N_s(E, n_x) = \frac{m_{n_x}^* d^2}{\hbar^2 \pi} f(E, n_x)$$

by defining

$$f(E, n_x) = \frac{\sqrt{1 + 2F(E - E_{n_x}^{(0)})} - 1}{F}$$

and

$$F = 2 \sum_{m \neq n_x} \frac{m^{*2}_{n_x}}{m^{*2}_{m,n_x}} \frac{1}{E^{(0)}_{n_x} - E^{(0)}_m}$$

Note that if its inside term is close to 1, taking the Taylor expansion of the square root leads to the same expression as for the first order approximation.
Finally, the density of state up to E is again given by eq. 5.19.
Computation-wise, each term m^{*2}_{m,n_x} can be computed by trapezoidal rule. Now, the sum on m in the expression of F contains an infinite number of terms and we have to hope there is no need to compute them all. Typically, we will be interested with the first few values of n_x and it is likely that the term in m will become small for m sufficiently larger than n_x.

5.6.3 Comparison with simple wells

For the simple well of sect. 4.3.4, the total energy was given as

$$E(n_x, n_y, n_z) = \frac{\hbar^2 \pi^2}{2m^*} \frac{n_x^2}{d_x^2} + \frac{\hbar^2 \pi^2}{2m^*} \left(\frac{n_y^2}{d_y^2} + \frac{n_z^2}{d_z^2} \right) \tag{5.25}$$

This is very similar to the expression obtained in sect. 5.6.2 with

$$E(n_x, n_y, n_z) = E^{(0)}_{n_x} + \frac{\hbar^2 \pi^2}{2m^*_{n_x}} \left(\frac{n_y^2}{d_y^2} + \frac{n_z^2}{d_z^2} \right) \tag{5.26}$$

The only differences are that a) we use a mass defined via first order perturbation, as the average inverse transversal mass $m^t(x)$ and that b) $E^{(0)}_{n_x}$ is obtained as the numerical solution of a discretized Schrödinger equation using a mass $m^{<100>}$ and a potential by layers.

In both cases, the final expression of the density of state is obtained by assuming that d_y and d_z are sufficiently large that we can assume continuous increments of energy and approximation via the surface of a disk.

6 Numerical examples of gains with Python

Sect. 3.4.2 gave the general expression of the material gain of active regions. Here, we provide a description of step-by-step calculation procedures as implemented in the Python code for three examples of structures of active regions. We begin with a bulk structure as the the simplest active region, for which we will describe basic methods that can apply to more complex cases. Then we present the computation method for a single quantum well and introduce how the k-selection of sect. 3.3.4 is ensured for wells. At last, we provide the implementation details of a more precise model for multiple quantum wells using the density of states derived in sect. 5.6 and that accounts for the probability of carrier presence in the various layers including barriers. For the sake of the example, it is applied to a single quantum well.

6.1 Bulk

In this section, we describe each step for the calculation of the gain for bulk regions. At the same time, we validate the Python code by replicating the chart of the gain spectrum for a bulk GaAs crystal of fig 4.24 of [19] shown in fig. 30.

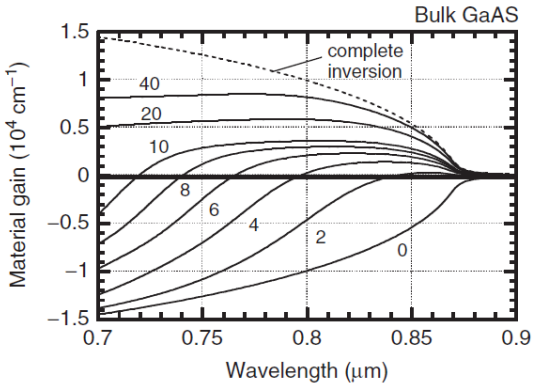

Figure 30: TE gain spectrum versus carrier density in GaAs based materials. Indicated values are the sheet carrier densities: $\times 10^{12}\text{cm}^{-2}$ (the bulk "sheet" density assumes an 80 $\mathring{A}$ width) (Source [19]).

As a reminder, the material gain per unit volume is given by

$$g_{21} = g_{max}(E_{21})\,(f_2(E_2) - f_1(E_1)) \tag{6.1}$$

where

$$g_{max}(E_{21}) = \frac{\pi e^2 \hbar}{n\,\varepsilon_0\,c\,m_0^2}\,\frac{1}{h\,\nu_{21}}\,|M_T|^2\,\rho_r(E_{21}) \tag{6.2}$$

Because the gain is used to solve the carrier and photons rate equations of sect. 2.3 for the respective densities N and N_p over the entire length of a device, it is common to show the gain spectrum as a function of the carrier density N. Therefore, the gain is calculated and depicted assuming N is known and the first step is to determine the quasi-Fermi levels of the conduction and valence bands in order to get the Fermi levels f_1 and f_2.

6.1.1 Determination of the quasi-Fermi levels

The state occupation probability, the Fermi factor f_2, of the conduction band is obtained by Fermi statistics using the quasi-Fermi levels E_{F_c}:

$$f_2|_{E_{F_c}}(E) = \frac{1}{e^{(E-E_{F_c})/k_BT}+1}$$

Likewise, f_1 has the same expression replacing E_{F_c} with the quasi-Fermi level of the valence band E_{F_v}. Fig. 31 gives an illustration of f. We use the term *quasi* because the usual Fermi levels are relative to the energy levels for crystals at equilibrium whereas we have a population inversion here. From the expression of f_2, we can see that the higher the quasi-Fermi level is, the higher is the probability of the state to be occupied. This corresponds to a high population inversion where a high level of energy was pumped into the crystal.
As N is given and as we assume charge neutrality, the density of holes is also known and we have:

$$N(E_{F_C}) = P(E_{F_v})$$

Therefore, we have two unknowns, E_{F_c} and E_{F_v} and two known variables N and P and we can solve for the quasi-Fermi levels by inversion:

$$E_{F_c} = N^{-1}(N), \quad E_{F_v} = P^{-1}(N)$$

The carries densities are given as the integrals over the range of possible energy levels of the density of state multiplied by the probability of the state to be occupied for N or empty for P:

$$N(E_{F_c}) = \int_{-\infty}^{+\infty} f_2|_{E_{F_c}}(E)\rho_c(E)dE$$

$$P(E_{F_v}) = \int_{-\infty}^{+\infty} \left(1 - f_1|_{E_{F_v}}(E)\right)\rho_v(E)dE$$

where the integration interval must be limited to the allowed relevant energy bands. Formulae of carrier densities for bulk and single quantum well are derived in sect. 4.6.
As shown in sect. 4.5, the density of states for bulk material in $\mathrm{J}^{-1}\ \mathrm{m}^{-3}$ are:

$$\rho_c(E) = \frac{\sqrt{E-E_c}}{2\pi^2}\left[\frac{2m_c}{\hbar^2}\right]^{\frac{3}{2}}, \quad \rho_v(E) = \frac{\sqrt{E_v-E}}{2\pi^2}\left[\frac{2m_c}{\hbar^2}\right]^{\frac{3}{2}}$$

Details on the computation of carrier densities ρ for bulk crystals are given in sect. 4.6. ρ is displayed in fig. 32 for a bulk crystal and two quantum well of different width d_x and the product ρf is shown in fig. 33.

Comments and observations:

- As expected, we observe that, as the width of the QW increases, the steps due to the discrete level of energy in the x direction become smaller. The bulk case is a limit case assuming that the discretization is so small that the energy level are continuous. This is illustrated by fig. 33 where we clearly observe that the density of a well converges to that of a bulk when the width of the well increases.
- For figures where we compare results of bulk crystal and QW 80 $\mathring{A}$, note that there is no such thing as a crystal of 80 $\mathring{A}$ behaving as a bulk with continuous densities. For this small width, the material will behave as a well, but nothing prevent us from applying the bulk equation just for the sake of comparison.

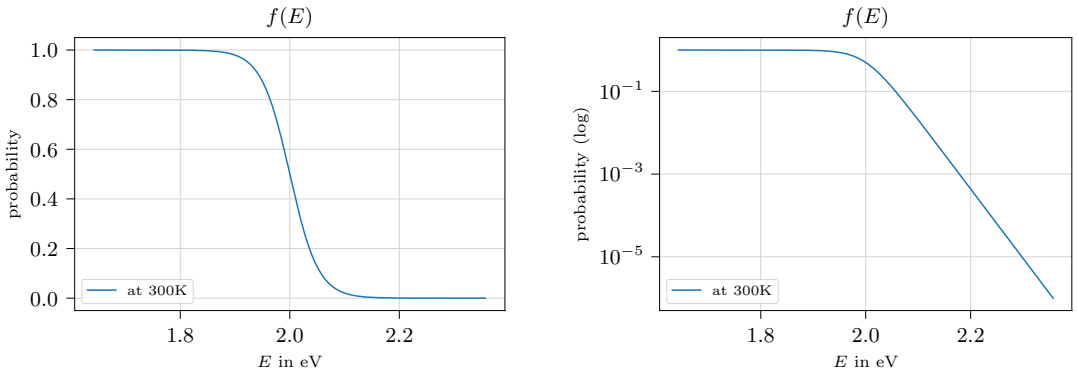

Figure 31: Fermi statistics $f(E)$, i.e., the probability of occupation, assuming $E_{F_c} = 2eV$ at 300K. Left: Linear scale, Right: Logarithmic scale.

- For the calculations, we took the band gap and the equivalent mass for GaAs as $E_g = 1.424eV$ at $300K$, $m_c = 0.067m_0$, $m_v = m_{LH} = 0.09m_0$. We took $E_v = 0$ and $E_c = E_g$ as the origin of energy is irrelevant (c.f. sect. 6.1.3).

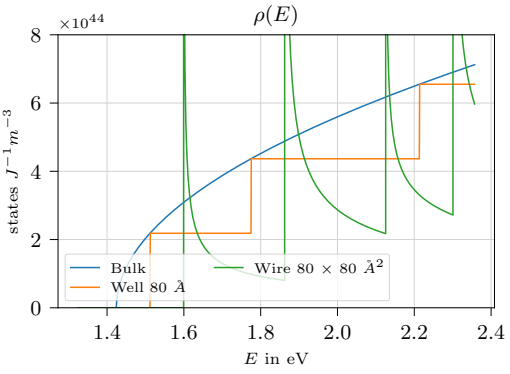

Figure 32: Density of states for GaAs bulk material, a quantum well and a quantum wire, with $m_c = 0.067$ and $E_c = 1.424eV$ as per eq. 4.6 and 4.8.

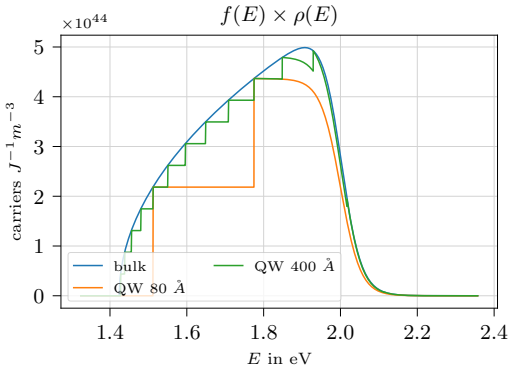

Figure 33: Product of state density and Fermi statistics for bulk and and 2 quantum wells ($d_x = 80\mathring{A}$ and $d_x = 400\mathring{A}$), assuming $E_{F_c} = 2eV$, with $m_c = 0.067$,$E_c = 1.424eV$ at 300K.

Fig. 34 shows $N(E_{F_c})$ and $P(E_{F_v})$ for various levels of E_F. There are many approximation closed-forms, surveyed in appendix 2 of [19], to compute N. We rather chose to perform the integration in Python using the well-suited generalized Gauss-Laguerre quadrature described in sect. D. Doing so, there is no need to worry about the range of accuracy of the closed-forms. With 50 quadrature points, the fractional error is of the order of 0.2%.
Inverting[21] [22] for example for $N = P = 20 \times 10^{12}\text{cm}^{-2}$, we find $E_{F_c} = 1.888eV$ and $E_{F_v} = -0.074eV$

[21] The inversion of N and P is done by the standard solver of scipy.

[22] If N is the density of carriers in m^{-3}, then $N \times 80\,10^{-10}$ is the surface density in m^{-2} and $N \times 80\,10^{-14}$ is the surface density in cm^{-2} for a width of $80\mathring{A}$. Finally, $N \times 80\,10^{-26}$ for the surface density expressed in $10^{12}cm^{-2}$. Hence, this multiplier in the python code.

for heavy holes.

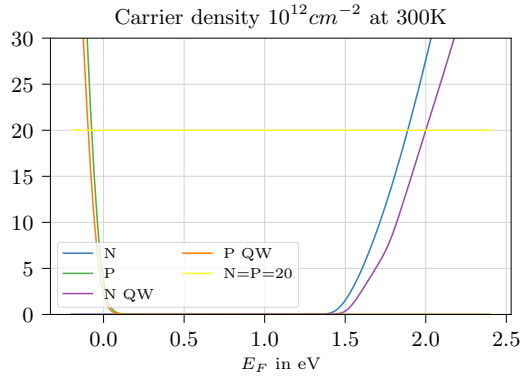

Figure 34: Sheet carrier densities $\times 10^{12}\text{cm}^{-2}$, for a bulk GaAs per 80 $\mathring{A}$ width and 80 $\mathring{A}$ QW. For $N = P = 20\times 10^{12}\text{cm}^{-2}$, the quasi-Fermi energy levels for bulk are $E_{F_c} = 1.888eV$ and $E_{F_v} = -0.074eV$. To obtain the same carrier density for te well, the quasi-Fermi levels are larger because the density of states is lower. Note that the carrier densities for the valence band are steeper due to larger mass of heavy holes.

6.1.2 Transition matrix element

As discussed in sect. 3.3.3, the term $|M_T|$ of the gain expression is given by tables 2 and 3. For bulk material, it is not function of the momentum k and the polarization is irrelevant. It is given as

$$|M_T|^2 = \frac{1}{3}\frac{m_0}{2}E_p = \frac{1}{3}\frac{m_0}{2}28.8 \text{ kg.eV}$$

which is consistent with eq. 3.15 for M_b^2.

6.1.3 E_{21}, ν_{21}, E_1, E_2 and n

The next step is to determine the values of E_{21}, ν_{21}, E_1, E_2 and n in the expression of the gain.

Freedom of gauge for energy levels: Because of the freedom of gauge, there is no need to know the absolute levels of energy: The origin of energy is arbitrary. For bulk, we simply take the origin as the top of the valence band, i.e., $E_v = 0$. (For more complex structures, we need other assumptions.) With this convention, Ec is equal to the band-gap E_g, as $E_c = E_v + E_g$.
The validity of the freedom of gauge is confirmed as we observe that the quantities needed to estimate the gain are only functions of a difference of energies whether this is for:

- The density of states in semiconductors of sect. 4.5.
- The Fermi factors that we could note $f(E - E_F)$ instead of $f(E)$.
- The expression of the carrier densities of sect. 4.6.
- The value of E_{21}.

The measurement of absolute levels of energy is complex and subject to errors, and discussed in some articles in the literature.

E_{21} **and** ν_{21}**:** Photons with energy $h\nu$ induce upward and downward transitions only between electron-hole pairs that conserve both energy and momentum. Therefore, E_{21} and ν_{21} are given by the usual relation[23]:

$$E_{21} = h\nu_{21}$$

and

$$\nu_{21} = \frac{c}{\lambda}$$

where λ is the wave-length of the light.

E_1 **and** E_2**:** To compute the gain, we need f_1 and f_2, hence E_1 and E_2. The k-selection rule of sect. 3.3.4 constrains transitions to iso-momentum vertical transitions on the $E - k$ characteristics of the material lattice of the semiconductor shown on a two-dimension k space in fig. 35. As we know E_c and

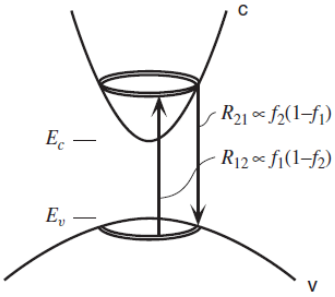

Figure 35: State pairs which interact with photons at E_{21}. Energy and momentum conservation reduces the set of state pairs to the annulus shown in the plot of energy versus momentum in two dimensions. Source: [19]

E_v and assuming the shape of $E - k$ is parabolic, E_1 and E_2 are entirely determined by their difference E_{21}. For instance, assuming a k-space of one dimension, the parabola equations are:

$$E_1 = E_v - \frac{\hbar^2}{2m_v}k^2, \quad E_2 = E_c + \frac{\hbar^2}{2m_c}k^2$$

Replacing E_2 by $E_1 + E_{21}$ gives

$$k^2\frac{\hbar^2}{2}(\frac{1}{m_c} + \frac{1}{m_v}) = E_{21} - (E_c - E_v)$$

With the same reduced mass m_r as defined in sect. 4.5 $\frac{1}{m_r} = (\frac{1}{m_c} + \frac{1}{m_v})$ and $E_g = E_c - E_v$, solving for k and re-injecting in the above equations yields:

$$E_1 = E_v - \frac{m_r}{m_v}(E_{21} - E_g), \quad E_2 = E_c + \frac{m_r}{m_c}(E_{21} - E_g) \tag{6.3}$$

In three dimensions, we obtain the same expression if the effective mass is isotropic, i.e., the same in all directions, that is, if E is given by $\frac{\hbar^2}{2m^*}(k_x^2 + k_y^2 + k_z^2)$. If not, E_1 and E_2 ar not entirely determined by the sole knowledge of E_{21} and can take a range of values, always separated by E_{21}.[24] In such case, the

[23] Basic relations of quantum mechanics: $\omega = 2\pi\nu, \quad \nu = \frac{c}{\lambda}, \quad E = h\nu = h\frac{\omega}{2\pi} = \hbar\omega$

[24] For example, let's assume the energies are given in two dimensions by

$$E_1 = -k_x^2 - 2k_y^2, \quad E_2 = 2k_x^2 + k_y^2$$

In the k-plane, iso-energy lines are ellipses of orthogonal major axes. As $E_2 - E_1 = 3(k_x^2 + k_y^2)$, the line with $E_2 - E_1$ constant at E_{21} is a circle of radius $\frac{E_{21}}{\sqrt{3}}$. Switching to polar coordinates with $k_x = \frac{E_{21}}{\sqrt{3}}\cos\theta$ and $k_y = \frac{E_{21}}{\sqrt{3}}\sin\theta$ with $\theta \in [0, 2\pi]$, E_2 takes the form:

$$E_2 = \frac{E_{21}}{\sqrt{3}}(1 + \cos^2\theta) \in [\frac{E_{21}}{\sqrt{3}}, 2\frac{E_{21}}{\sqrt{3}}]$$

gain g_{21} could be taken as an average, weighted in some fashion by $\rho_v(E_1)$ and $\rho_c(E_2)$, over the range of possible E_1 and $E_2 = E_1 + E_{21}$. Now, the expression of the density of states should be revised too because they were derived with an isotropic effective mass hypothesis. Throughout this document, we assume isotropic masses and parabola unless specified otherwise.

Refractive index n: At last, n is the refractive index taken from table 2.

6.1.4 Uncertainty of energy and lineshape broadening

Energies of carriers are uncertain because they can collide with phonons and other carriers. This is illustrated by the thick iso-energy circles of fig. 35.
As a consequence, we need to account for the probability density of the energies of electrons and holes, which, combined, result in a probability density function for transition energy E_{21}, called the *lineshape* function and noted $\mathcal{L}$. To account for the uncertainty of energies in the calculation of the gain, we take the convolution of g_{21} and $\mathcal{L}$ as follows:

$$g(h\nu_0) = \int g_{21}(h\nu_0, E_{21})\mathcal{L}(h\nu_0 - E_{21})dE_{21} = (g_{21}(h\nu_0, .) * \mathcal{L}(.))\,|_{\nu_0} \tag{6.4}$$

where $g_{21}(h\nu_0, E_{21})$ is given by eq. 6.1 in which $h\nu_{21}$ should be set to $h\nu_0$ and g_{21} should be viewed as a function of two separate variables $h\nu_0$ and E_{21}. Following [19], when scanning the domain of E_{21} in the integral, terms in the expression of g_{21} that depend on E_{21} must be updated, including the levels of E_1 and E_2 of eq. 6.3 derived in sect. 6.1.3, but ν_0 must be kept unchanged.[25]. The integral is the convolution over E_{21}, evaluated at the point ν_0, of a function that depends of ν_0.
The uncertainty of energy comes from the time-dependence evolution of the state of an electron that we note $P(t)$. From [51], an optical dipole subject to collision-induced relaxation is generally written as

$$P(t) = P_0 e^{\pm i\omega_0 t} e^{-L(t)}$$

and the lineshape function is defined as the Fourier transform of $P(t)$.
We look at the three distributions discussed in [19].

Lorentzian function The simplest lineshape function assumes an exponential decay, with $L(t) = a|t|$. Taking the Fourier transform from tables of standard functions, and replacing ω by $\frac{E}{\hbar}$ gives[26]:

$$\hat{P}(\omega) = P_0 \frac{2a}{a^2 + \omega^2} = P_0 \frac{2a}{a^2 + (\frac{E}{\hbar})^2} = P_0 \frac{2a\hbar^2}{a^2\hbar^2 + E^2}$$

Setting $\tau = \frac{1}{a}$ and choosing $P_0 = \frac{1}{2\pi\hbar}$ so that the total probability is 1, yields to the *Lorentzian* lineshape function:

$$\mathcal{L}(E) = \frac{1}{\pi} \frac{\hbar/\tau}{(\hbar/\tau)^2 + E^2}$$

where a typical value for τ is 0.1 ps.
We can verify that this is a probability distribution by confirming its integral is 1:

$$\int_{-\infty}^{\infty} \mathcal{L}(E)dE = \frac{\hbar/\tau}{\pi} \int_{-\infty}^{\infty} \frac{1}{(\hbar/\tau)^2 - E^2} dE = \frac{\left[\tan^{-1} \frac{E}{\hbar/\tau}\right]_{-\infty}^{\infty}}{\pi} = \frac{\pi}{\pi} = 1$$

[25] $h\nu_0$ must be kept constant because it is the energy of the incoming photons whose electric field creates perturbation in the Hamilton of electrons. In the interaction, only E_{21} is subject to the uncertainty of the electron energy.

[26] In fact, ω should be shifted by ω_0, as in $P_0 \frac{2a}{a^2 + (\omega - \omega_0)^2}$, but we assume $\omega_0 = 0$ to have a function that is symmetrical around $E = 0$.

In the above, it is important to note that $\mathcal{L}(E)$ is real because $P(t)$ is defined over $\mathbb{R}$ and not only for $t > 0$ and is even with $P(-t) = P(t)$. If $\mathcal{L}$ is to be computed by DFT, we need to take symmetrical samples of $P(t)$ to ensure the result is real. Because samples are numbered from 0 to $N-1$, sampling must be done so that $t = 0$ lies exactly at the middle of samples $\frac{N}{2} - 1$ and $\frac{N}{2}$: Time is shifted by $\theta = \frac{N-0.5}{2}\frac{1}{\nu_S}$, where N is the number of FFT points and ν_S the sampling frequency.
In order to compare this lineshape with others, we will normalize their energy full widths at half magnitude (FWHM) noted ΔE_{21}. We find that the density is half of its maximum at $E = 0$ for $E = \pm\frac{\hbar}{\tau}$. Therefore the width is $\Delta E_{21} = 2\frac{\hbar}{\tau}$.

Chinn function [50] As the Lorentzian function does not describe gain spectrum precisely, a good and efficient approximation of the lineshape function has been suggested by Chinn et al. [50] as discussed in [19], where $P(t)$ reads:

$$P(t) = e^{-l(t)}$$

and

$$\log_{10} l(t) \coloneqq 2 + 1.5\log_{10} t - 0.5\sqrt{(2+\log_{10} t)^2 + 0.36}$$

and t is in ps.
There is no analytical expression for its Fourier transform and we must resort to DFT. Here again, the DFT must be taken over an interval of time centered at $t = 0$. Besides, we need to make three adjustments to the definition of $P(t)$:

- First, as we want to obtain a lineshape function in $\mathbb{R}$, we set $P(-t) = P(t)$, by replacing t by $|t|$ in the above definition for $l(t)$.
- Second, we multiply by P by a constant P_0 in order to normalize the total probability. P_0 is chosen by integrating the DFT over the frequency range and normalizing it.
- Lastly, to preserve the same FWHM as that of the Lorentzian function, we scale the time by a factor β.[27]. We found a value of $\beta = 1.1245$ with 2^{16} FFT points.

Hence, P is rewritten as

$$P(t) = P_0 e^{-l(\beta|t|)}$$

Gaussian We also consider a Gaussian function, normalized in probability and in FWHM.

$$\forall t \in \mathbb{R},\ P(t) = P_0 e^{-\alpha t^2}, \quad \hat{P}(\omega) = P_0\sqrt{\frac{\pi}{\alpha}}e^{-\frac{\omega^2}{4\alpha}}$$

with $P_0 = \frac{1}{2\pi}$. At half the full width, $\hat{P}(\omega)/\hat{P}(0) = 0.5$. With $\omega = \frac{\Delta E_{21}}{2\hbar}$, we get $\alpha = \frac{1}{4\log(2)\tau^2}$.

The FWHM-normalized lineshape[28] functions are illustrated in fig. 36.

[27] As a general property, the Fourier transform of $x(at)$ is $\frac{1}{|a|}\hat{f}(\frac{\omega}{a})$. Therefore, we can adjust the width of the Fourier transform by scaling the time.
[28] Implemented in Lineshape.py

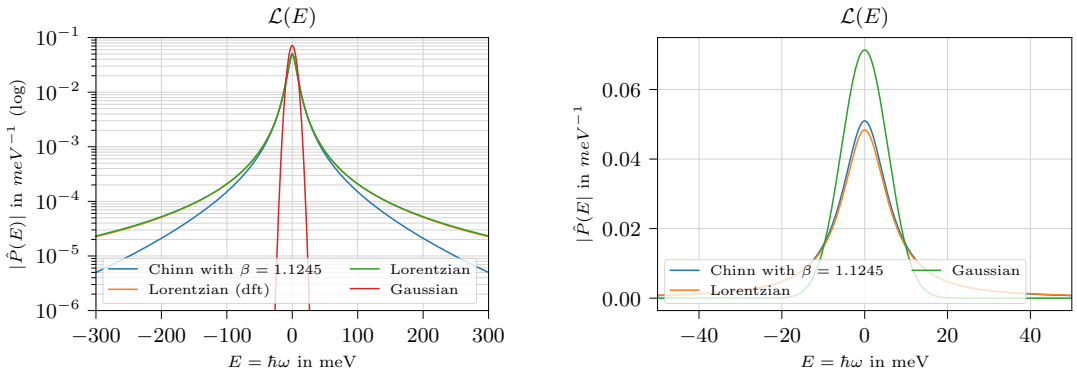

Figure 36: Lineshape functions with normalized energy at full-width half magnitude. With $m = 5$ and 2^{16}-points FFT. On the left, we show that the Lorentzian computed by FFT of $P(t)$ is very precise and match its analytical expression.

Choice of the sampling parameters We choose a sampling frequency ν_S such that half of ΔE_{21} corresponds to a multiple of the interval between discrete frequency levels of frequency of the FFT.

$$\exists p,\ 2\pi\hbar\nu_S \frac{p}{N} = \frac{\Delta E_{21}}{2}$$

Besides we want ν_S to be larger than a given multiple m of $\frac{1}{\tau}$.

$$\nu_S \geq \frac{m}{\tau}$$

This translates to

$$p = \max\left(\lfloor \frac{N}{m}\frac{\Delta E_{21}\tau}{4\pi\hbar} \rfloor, 1\right), \quad \nu_S = \frac{N}{p}\frac{\Delta E_{21}}{4\pi\hbar}$$

The functions $\mathcal{L}$ are not band-limited but drop quite rapidly. As per the Nyquist–Shannon sampling theorem, we must take a sampling frequency equal to 2 times the maximum frequency of $\mathcal{E}$ to avoid aliasing. For sake of accuracy, we chose $m = 5$ for which corresponds to an energy of 1300 meV. Now, from the chart, we could consider that the lineshape is very small at 200 meV and take a sampling at 400 meV.

Computation of the gain by convolution $g(h\nu_{21})$ can be computed as follows[29]:

- Take the inverse Fourier transform of $g_{21}(\nu_{21}, E_{21})$ with respect to E_{21}.
- Multiply it by $P(t)$ with a window centered around $t = 0$.
- Take the Fourier transform of the product, that should be real and even.

As an example, fig. 37 shows the impact of convolution on a dummy gain function, defined by $100 - 5E$ for $E \in [40, 60]$ with E in meV.

[29] As it is a bit tedious to implement in such way, the python code uses the function that convolution by FTT from the scipy library.

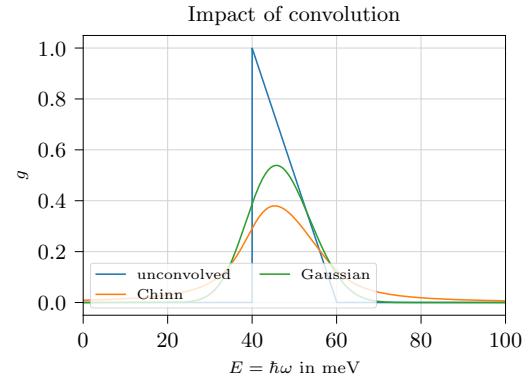

Figure 37: Convolution of a dummy gain function with FWHM-normalized lineshapes.

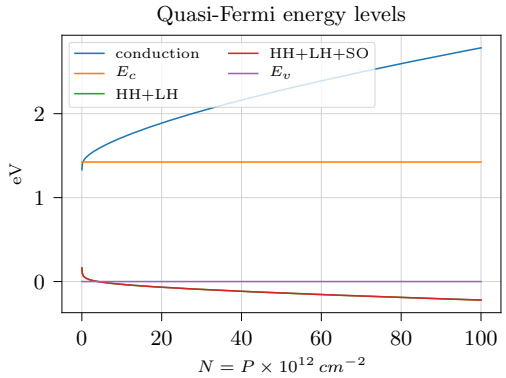

Figure 38: Quasi-Fermi levels implied from the carrier density for conduction and valence bands, for bulk regime assuming a width of 80 $\mathring{A}$. The bottom and top of the bands are indicated by the horizontal lines. The split-off band has no impact on the energy levels.

6.1.5 Reduced density of states

The reduced density of state of the term $\rho_r(E_{21})$ in the expression of the gain is calculated as the sum of the reduced density of states as per sect. 4.5 computed for the three possible transitions: conduction-heavy hole pairs, conduction-light hole pairs and conduction split-off pairs.

6.1.6 Implying the quasi-Fermi levels

For the valence bands, the carrier density is the sum of that of heavy, light and split-off holes using the same quasi-Fermi level for all three sub-bands. Fig. 38 shows the quasi-Fermi energy levels obtained by inversion of the carrier density. It shows that the split-off band has no impact on the Fermi level of the valence band.
According to its formula, the carrier density can not be null and tends to 0 when the energy level tends to $+\infty$ ($-\infty$) for the conduction (valence) band. This is not apparent in the chart because of numerical precision: for low carrier density, the Fermi level is almost a vertical line and its inversion is prone to numerical errors.

6.1.7 Spectrum

Finally fig. 39 shows the gain for a bulk structure at various wave-lengths. In order to clearly show the first wavelength where transitions start to occur and to clearly show the small impact of the split-off just

above 0.7μm for $N = 0$ and $= 200$, we did not apply the lineshape convolution because it smoothing effect would hide these. As the spectrum is smooth, the convolution is expected to have a relatively small impact and we should find results similar to Coldren's.

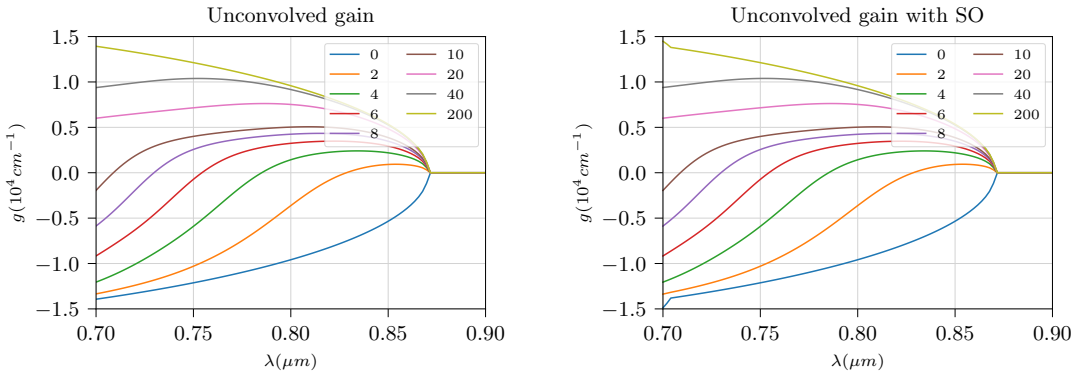

Figure 39: Material gain for bulk material (per 80 $\mathring{A}$ width) at various levels of carrier density N in $10^{12} cm^{-2}$. Both graphs account for heavy and light holes. The graph on the right also accounts for the split-off band in the calculation of the Fermi level and of the gain. Because its top energy is low, the split-off band bumps the gain only below some low wave-length threshold.

6.2 Single quantum well

In this section, we compute the spectrum of a single quantum well using the simplified approach of chapter four of [19]. The spectrum of a GaAs/$Al_{0.2}Ga_{0.8}As$ quantum well is depicted in Fig. 40 before and after applying lineshape broadening. We apply non-integer quantum numbers of finite potential well for x from sect. 5.3 and the simple density of states for quantum well of sect. 4.3.4. The band gaps of GaAs and $Al_{0.2}Ga_{0.8}As$ respectively are 1.424 eV and 1.673 eV.

Calculation is done with the following assumptions:

- To imply the quasi-Fermi levels from carrier densities, we need to align the band offsets at hetero-interfaces. For sake of simplicity and given that the model is quite simplified here, we choose to apply half of the difference of the band gap, i.e. $\Delta E_c = \Delta E_v = \frac{1}{2}\Delta E_g = 0.1245$ eV, in the calculation of the densities of states for the conduction and valence bands. We use eq. 4.8 of sect. 4.3.4 for the density of states, with the energy quanta q_n from sect. 5.3 $E_{n_x} = q_n^2 E_1^\infty$.
- The density of states of the valence band is taken as the sum of the densities for heavy and light holes only as we earlier saw that split-off holes have barely no impact. Note that the energy quanta for heavy holes and light holes are different because their equivalent masses are different.
- The k-selection rules described in sect. 3.3.4 for quantum wells is such that transitions between conduction and valence bands are dominant for the same quantum numbers, i.e. $n_{hh} = n_c$ or $n_{lh} = n_c$. Here, we instead compute the total gain as a sum over heavy and light holes and over the quantum numbers using reduced densities. We will see in sect. 6.3 that this is consistent with the k-selection rule. The gain before line-shape broadening is given as:

$$g(h\nu_{21}, E_{21}) = \frac{\pi e^2 \hbar}{n\,\varepsilon_0\,c\,m_0^2}\frac{1}{h\,\nu_{21}} r(E_{21}) \tag{6.5}$$

where

$$r(E_{21}) = \sum_{\text{hh, lh}} |M_T|^2 \left(f_2(E_2) - f_1(E_1)\right) \sum_n \rho_r(E_{21}, n) \tag{6.6}$$

- The matrix element M_T is a function of the hole type and given tables 2 and 3.
- The energies E_1 and E_2 are functions of the hole type via the reduced masses and computed by eq. 6.3.
- For the reduced density of states $\rho_r(E_{21}, n)$, we assume parabolic $E - k$ curves and apply the density of a finite potential well to the particle of reduced effective mass. We set the potential barrier as the full band gap difference between the active and barrier materials, 0.245 eV. Eq 4.8 of the density of state is adjusted by replacing n by q_n or simply E_n:

$$\rho_r(E) = \sum_n \rho_r(E, n) = \frac{m^*}{\pi\hbar^2 d_x} \sum_{q_{n=1,\cdots}} \mathcal{H}(E - q_n^2 E_1^\infty) = \frac{m^*}{\pi\hbar^2 d_x} \sum_{q_{n=1,\cdots}} \mathcal{H}(E - E_n) \tag{6.7}$$

- Injecting eq. 6.5, the convolution by the lineshape function reads:

$$\begin{aligned} g(h\nu_{21}) &= \int g_{21}(h\nu_{21}, E_{21}) \mathcal{L}(h\nu_{21} - E_{21}) dE_{21} \\ &= \frac{\pi e^2 \hbar}{n\,\varepsilon_0\, c\, m_0^2} \frac{1}{h\,\nu_{21}} \int r(E_{21}) \mathcal{L}(h\nu_{21} - E_{21}) dE_{21} \end{aligned}$$

  This expression is nice because we can first compute $r(E_{21})$, then convolve with the Chinn windows of sect. 6.1.4 (here with $\beta = 1$), and finally divide by $h\nu_{21}$. For sake of precision, the charts are computed on 1024 energy levels with a window of 256 points.

- Photons at lower wavelength will interact with the carrier in the barrier material. This is not calculated here.

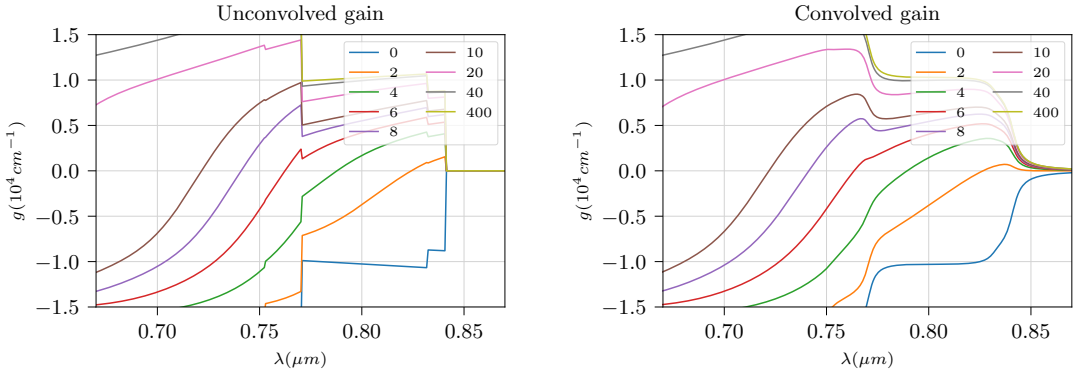

Figure 40: TE gain spectrum for a GaAs/$Al_{0.2}Ga_{0.8}As$ of 80 $\mathring{A}$ width at various levels of carrier density N in $10^{12} cm^{-2}$. On the left, the gain is not convolved. The first bump corresponds to the band-gap energy shifted by the first quantum number from heavy holes, $E_g + q_1^2(\text{HH}) E_1^\infty(\text{HH})$. The second bump to the first quantum of energy from light holes, $E_g + q_1^2(\text{LH}) E_1^\infty(\text{LH})$ and the third to the second quantum of energy of heavy holes, $E_g + q_2^2(\text{HH}) E_1^\infty(\text{HH})$

6.3 Multiple quantum well

In this section, we derive the gain spectrum for the structure with multiple quantum wells illustrated by fig. 22.
Before we describe the calculation methodology, we must consider where the charges and photons are. This leads us to make the following considerations about the density of states and the locality of the gain.

6.3.1 Considerations on density and locality of the gain

In sect. 5.6, we solve for the Eigen-energies of the 3D Hamiltonian over the entire device. As a consequence, the number of states N_s up to a given energy of eq. 5.17 is a function of the entire geometry of the device and of the relevant boundary conditions. Viewing the number of states as a function of the position or as a function of the well layer would be a misinterpretation. When derived with respect to E, **it gives a density of the energy as a function of the energy. It is by no mean a density as a function of some spacial position**. For instance, it is not comparable to the density of electrostatic charge inside a metal or to the density of a gaz in a volume.

When we divide the number of states by the volume of the device, it could lead to the erroneous perception that this gives a density as a function of the position or that, if we multiplied each dimension by two, then the number of states will be multiplied by eight. This is not true except for bulk device where the number of states happens to be nicely proportional to the volume, and this is solely due to the fact that the number of harmonics in each direction doubles. Now, it is not entirely false for a single quantum well whose density of states is inversely proportional to the width of the well. The number of quantum states in infinite, but they are spaced by increments of energy that decrease as the width increase. Therefore the number of states up to a given energy will nearly be multiplied by eight.
Dividing by the width of the well in the calculation of densities for a single well as in sect. 6.2 is an arbitrary choice and we could divide by any width. For a well with barrier with infinite potential, carriers are entirely confined inside the well. If photons were also perfectly confined, then dividing by the width of the well is the most relevant choice. For MQW with thin barriers, electrons are not confined to well and we can rather divide by the total width of well and barriers.

At last, ultimately, the actual gain will depend on the confinement of photons and on whether their electric field modifies the Hamiltonian uniformly. But the gain g_{21} does not need to know about that because if is a function of the carrier density N and is applied to the photon density N_p, both of which are local and functions of z in the rate equations of sect. 2.3. **Therefore g_{21} is local and depends on z via N.**

6.3.2 Methodology

Calculation is done in a same manner as for single quantum well except the following. The main difference is that we will take into account transitions that can happen between electrons and holes everywhere inside the device including inside the barriers.
As discussed above, the density of transition pairs at a given energy E_{21} is a function of the entire device and not of the position. Yet, for an incoming photon of energy $h\nu_{21} = E_{21}$, the levels of energy of the hole, E_1, and of the electron, E_2, involved in the transition depend on their effective masses, hence on the layer l. Hence, we have to compute them for each layer. Besides, we propose to adjust eq. 6.6 to account for the probability $P_{n_x}^{h,l}$ of the pair in state number n_x to be in the layer l.

$$g(h\nu_{21}, E_{21}) = \frac{\pi e^2 \hbar}{\varepsilon_0 \, c \, m_0^2} \frac{1}{h \, \nu_{21}} \sum_{\text{h=hh, lh}} \sum_{l} \frac{1}{n_l} \left| M_T^{h,l} \right|^2 \left(f_2(E_2^{h,l}) - f_1(E_1^{h,l}) \right) \sum_{n_x} P_{n_x}^{h,l} \rho_r(E_{21}, n_x) \tag{6.8}$$

where we moved the refractive index n_l inside the sum over the layer l. We neglected the sensitivity of the refractive index to the photon wavelength and use its level at the 1μm of interest.
We also indicated the dependency of the matrix element on the hole and the crystal of the layer by the superscripts h and l. Note that the density ρ_r^h is not a function of the layer because computed from Eigenvalues of the entire device, but a function of the hole h. It is computed from eq. 5.19.
The probability is computed as the integral of the square modulus of the wave function for x over the layer l (for the hole h)

$$P_{n_x}^{h,l} = \int_l |\psi_{n_x}^h|^2 dx \tag{6.9}$$

with $\forall h$, $\forall n_x$, $\sum_l P_{n_x}^{h,l} = 1$.

Eq. 6.8 is only valid if the effect of photons on transitions is uniform along x and y and the same in all layers including *barriers* [30]. If light was perfectly confined to wells only and in an uniform manner in each well, then each layer should also be multiplied by its confinement factor Γ_l, null in barriers. By comparison, it is worth noting that we did not account for the probability of the transition to occur in the well for the spectrum on the single well of sect. 6.2 and we defined d_x as the width of the single well: The result is valid only assuming we can neglect the probability of the pair to be outside and assuming the confinement of the light is perfect. This explains the differences of spectrum between this section and sect. 6.2.
Some papers (for instance, [75]) on MQW in the literature assume that barriers are sufficient large that wells are uncoupled. Their results are valid if the probability of carriers to be outside wells is also assumed to be null, which is fair as it is small for low quantum numbers as shown in sect. 5.3 and as we are interested in low quantum numbers for the range of wavelength of the spectrum we consider.
The above considerations imply that calculation of spectral gain should be adapted to the geometry of the wave-guide.

6.3.3 Details of the implementation

- Band offsets are aligned using the methodology of electron affinity of sect. 3.5. All energies are then shifted by the middle of the lowest conduction band bottom across all layers and the highest valence band top. This is depicted in fig. 16a.[31]

- Zero-order approximation of the Eigenvalues E_{n_x} in the conduction band and the heavy and light holes valence bands are obtained by the numerical methodology described in sect. 5.5 and 5.6. In each region of the structure, we apply the effective mass of the relevant crystal and the relevant band. For instance, for energies of heavy holes in the valence band, we apply the effective masses along $< 100 >$ and its transveral plane of heavy holes in both the wells and the barriers. The density of states is computed from the first [32] approximation of E_{n_x} of the perturbation method of sect. 5.6.2.

- The density of transition pairs is also computed using sect. 5.6 with reduced masses along $< 100 >$ and its transversal plane.

- We assume that the Fermi levels E_{F_c} and E_{F_v} for the conduction and valence bans are unique for the entire device. This is reasonable because we are working with wave functions that are solutions

[30] We put the term *barrier* in italic because, in devices made of more than two types of crystals, there are intermediary layers that are neither *barriers* nor *wells*.

[31] The code assumes the band offset alignment is such that no valence energy is higher than no conduction energy. If not, minor code adjustments are required.

[32] The second order formula was not implemented.

on the entire device. Therefore, it is computed by inversion of the number of carriers computed as the integral over the entire volume of the device of the density of states multiplied by the Fermi function. Besides, we apply the same Fermi levels for the heavy and light sub-valence bands.

- At last, we deduct E_2 and E_1 from E_{21} as in 6.1.3 and we must use isotropic approximations of effective masses (as a function of the layer) from [68]:

$$m_{hh}^{\text{iso}} = \frac{m_0}{\gamma_1 - 2\gamma_2^*}$$
$$m_{lh}^{\text{iso}} = \frac{m_0}{\gamma_1 + 2\gamma_2^* f}$$

where $\gamma_2^* = \frac{\gamma_2+\gamma_3}{2}$

6.3.4 Compliance with the k-selection rule

As per the k-selection rule of sect. 3.3.4, we should only consider transitions at iso-quantum numbers. For instance, transition from the first sub-band level of the valence band to the second sub-band of the conduction band is not possible. Now, when we apply the reduced mass mathematical artifact, we do not compute the density of transition pairs from the densities of states of the two bands (conduction and heavy hole valence band for instance) but instead from the reduced density of states. It is not obvious that this calculation complies with the selection rule. In particular, does the n$^{\text{th}}$ solution of the Schrödinger equation with reduced mass corresponds to the difference of the n$^{\text{th}}$ solutions for both bands, for all n? We do not attempt to derive a proof but we confirm below that: a) the first three *reduced* Eigen-energies E_{21}^i for $i = 1, 2, 3$ are indeed very close to the first three elements on the diagonal of the matrix $\left(E_c^i - E_{hh}^j\right)$; and b) no non-diagonal element shows up in the reduced Eigen-energies. The values are not exactly the same because there is no reason for the Hamiltonian of the various bands to commute, suggesting that a proof would not be trivial because the reduced mass trick is an approximation to begin with.

$$\left(E_c^i - E_{hh}^j\right) = \begin{pmatrix} 1.47 & 1.50 & 1.55 \\ 1.59 & 1.62 & 1.66 \\ 1.67 & 1.70 & 1.74 \end{pmatrix} eV \quad E_{21}^i = \begin{pmatrix} 1.48 \\ 1.62 \\ 1.76 \end{pmatrix} eV$$

6.3.5 Spectrum

As discussed at the end of sect. 5.5, if the wells are of the same width and if the inter-well barriers are large, the multiple well behaves as a sum of independent wells. Eigen-energies are degenerate with a multiplicity equal to the number of wells. As the number of states is multiplied by the number of wells and the volume too, the density of state per volume of wells will be the same as that of a single well.
When the barriers are narrow, each degenerate energy level splits in separate energies scattered around the energy level of a single well. Therefore, the jumps of the spectrum of a single well, will be cut into several smaller jumps spread around it.
Here, we only show the spectrum obtained by this methodology to a single quantum well for sake of comparison with the previous case. it is shown in fig. 41b. We do not expect results to be equal because the prior methodology is much less precise, but they are similar.

Notes for subsequent work

- For the first quantum number, holes in the valence band and electrons in the conduction band do not have the same probability to be inside the wells. Hence, we may need to adjust $\rho_r(E_{21}, n_x)$ by the probability of both particles to be in the same layer l. Above, we used the probability of the

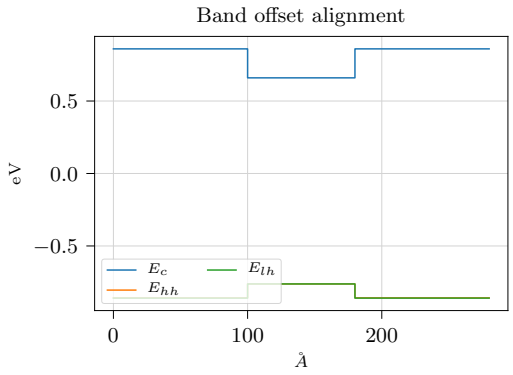

(a) Band offset aligned based on electron affinity, shifted by the mid point between the lowest conduction band and the highest valence band.

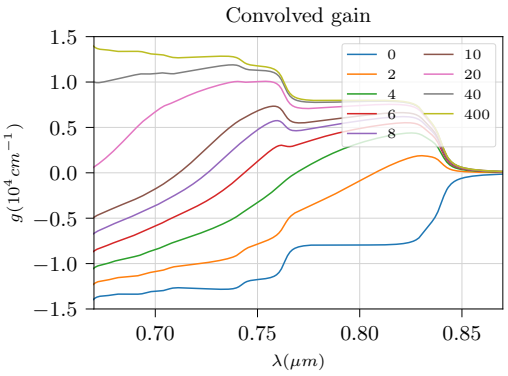

(b) Gain spectrum computed inside the well only.

Figure 41: Band offset alignment (a) and TE gain spectrum (b) for a GaAs/$Al_{0.2}Ga_{0.8}As$/GaAs of 100/80/100 $\mathring{A}$ width at various levels of carrier density N in $10^{12} cm^{-2}$.

pair to be in the layer l, derived from the wave functions computed using the reduced mass trick. We should confirm that this result in the same.

- When computing gain of SOA using a confinement factor, it is necessarily an approximation unless the confinement factor not only accounts for the confinement of photons, but also the confinement of transition pairs in the well, which depends on the quantum number. If so, it would be more straightforward to directly compute the gain using the density of photon and of pairs. For that purpose, we must start by considerations on the transition phenomenon, the application of the Fermi Golden rule and the creation of the perturbing electric field generated by photons in layers with different refractive indices.

- Carrier pumping may not be uniform either.

7 Bandgap engineering and design of Al-free GaAs based 1um SOA

This section discusses the various parameters or features that can be engineered in order to obtain an amplifying medium, in our case an SOA. By chosing adequate parameters, we will propose new quantum well and barrier structures with different properties.

7.1 Parameters for engineering

For a given SOA structure, we will primarily analyze its material gain spectrum and differential gain. Therefore, the variables we need to carefully tune are those that actually influence these characteristics. We distinguish **3 most important parameters** that can be adjusted to achieve various tailor-made properties of an active device.

The choice of **materials of layers, wells and barriers,** is the most primordial step for SOA designing. Each material has its own properties, such as band gap and lattice constant as shown by 42. A range of semiconductor elements can be used for layers. Popular ones in photonics application are III-V compounds because they exhibit direct bandgap in most cases, which leads to higher efficiency in optoelectronic energy transitions. Most structures have wells and barriers made of alloys combining several of these elements: Al, Ga, In for type III, and N, P, As and Sb for type V. Binary (e.g. GaAs) and ternary (e.g. $In_xGa_{1-x}As$) are the most common compounds because there properties are widely studied and documented, but quaternary compounds (e.g. $In_xGa_{1-x}As_yP_{1-y}$) are as much important because the two mole fractions x and y provide more degrees of freedom for more flexible design.

Here, we will not study IV-IV compounds (Si, Ge,...) nor II-VI compounds (Zn, Mg, S, Se,...). IV-IV compounds are popular because of their already wide use and low cost, but have indirect bandgaps. Thus they are not compatible or adapted for photonic applications by nature. In the other hand, bandgaps of II-VI compounds are direct but considerably large. Therefore, these are not suited for operation at 1um.

We will focus on SOA with single or multiple quantum wells and **the obvious key factor regarding the objective of this work is to chose the proper compound for the wells, that offers a bandgap that corresponds to a wavelength near 1um. This will be addressed in sect. 7.3.**

The choice of the material for barriers is important too because the difference of bandgap between barriers and wells represents the potential of the finite quantum well of sect. 5.3. Therefore it determines how the quantum numbers of the well are close to their integer ceiling values. In effect, the recombination occurs not for electrons and holes separated by the energy gap E_g, but by the difference between the first Eigen-energies of the conduction band and of the valence band (heavy and light holes). Besides, deeper wells also means higher carrier confinement, potentially increasing the total gain of the SOA.

The **widths of wells and barriers** are the next important parameters. Barrier widths are usually in the range from 10 to 100nm for MQW and can be as wide as needed for SQW. For single quantum wells, changing the barrier width has no influence on the material gain or the differential gain. Instead, large barriers with no strain are typically used for compensating the strain in the well. While the barrier width is not so important for SQW, it will have an upmost importance for MQW.

The width of wells will change the energy quanta $\frac{\hbar^2\pi^2}{2m}\frac{q_n^2}{d^2}$ in the same manner as the choice of the materials modifies the Eigen-energies. It is typically very thin and takes values from 5 to 10nm. The larger the well, the more subbands there will be in the conduction band and valence band because their spacing decreases and this affects the performance of the well because it will require more injection current. Also, the larger the well, the lower the effective bandgap E_{21} will be, because the first energy quanta is smaller. Eventually, if the well is very large, it will behave as a bulk and the effective bandgap becomes close to E_g.

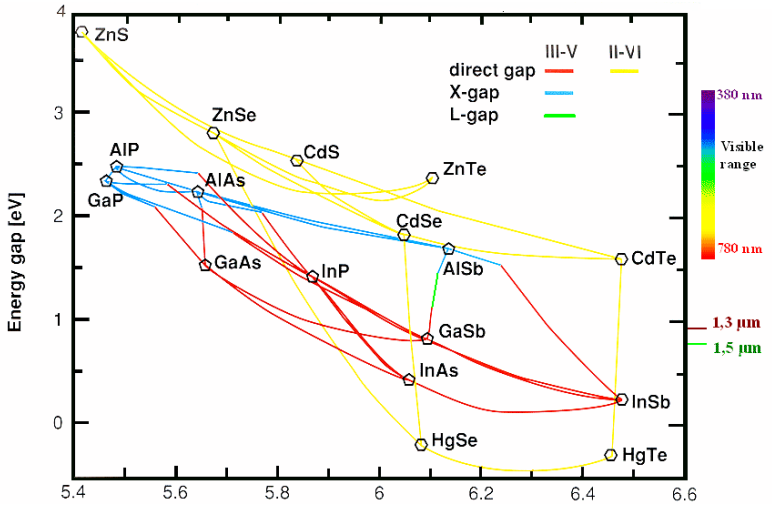

Figure 42: Diagram showing the bandgap energy and lattice constant of several alloys. Ternary alloys are located on the lines between the points, with varying mole proportion.

Strains on wells and barriers are the third important quantities. Strain is not a parameter per se because it is a consequence of the choice of materials, but it is crucial to make sure that strain is not too large to ensure the stability of the device. While the ability to chose various materials is key to adjust the characteristics of the SOA, different materials have different lattice constants. However, the wells and barriers must share the same lattice constant as the substrate in order to be able to grow the overall structure. Applying strain on the wells and barriers allow to change their crystal lattice and achieve a lattice match. The strain is therefore a complementary parameter used to balance the choice of materials and widths and the need to obtain a stable structure.

7.2 Experimental considerations for bandgap engineering

Before addressing the choice of the well and barrier, a few considerations coming from experimental observations are worth to be noted and must be kept in mind in our design:

- The substrate choice for 1μm wavelength SOA is GaAs. This is simply because it is not possible to grow structures that perform amplification at 1μm with other substrates, InP including. Besides, existing OPA at 1μm are typically grown on GaAs. Therefore, to integrate the SOA in the OPA, the SOA must be also grown on the same substrate.

- The overall strain of the active region must be neutral in order to have a stable structure. For MQW, if the wells have a compressive strain, barriers must have the adequate tensile strain and adequate width to obtain a 0 strain on average in the active region. For SQW on the other hand, because the barrier width has no impact on the SOA property, we can chose barriers that are as wide as needed. Therefore, the average strain can be approximated by the strain of the barrier itself, that we will preferably set to be 0.

- Strain is only possible up to some reasonable and adequately low level. Experimentally, the maximum recommended strain is of 3% of the original crystal lattice. For example, an alloy with $5.5\mathring{A}$ lattice can have a strained lattice between 5.35 and $5.65\mathring{A}$. Even though the strain allows

more flexibility for the choice of materials, it also imposes a physical limit that must be taken into account.

- The bandgap must be chosen about 0.1eV below the energy gap that corresponds to the targeted wavelength. Indeed, as mentioned above, the effective bandgap E_{21}, i.e. the lowest energy gap of actual stimulated transitions, is slightly higher than E_g. In our case, a 1μm wavelength corresponds to E_{21}=1.24eV. Therefore, the well's bandgap must be slightly lower, typically at around 1.14eV depending on its width and potential depth.

7.3 Choice of well

Alloy: As the primary objective of this work is to propose SOA that work at 1000nm, we must chose the alloy of the well to have a bandgap of about 1.14eV while keeping the lattice constant at 5.65 $\AA$ of the GaAs substrate. Fig.43 shows the energy gaps of different alloys and their strains when lattice-matched to GaAs. The alloys represented on the figure were taken among those commonly found in articles in the literature relative to lasers at 1μm. For ternaries in the upper charts, it clearly appears that there are only two compounds that can have a bandgap E_g=1.14eV, either $In_xGa_{1-x}As$ or $InAs_xP_{1-x}$. For quaternary InGaAsP on the lower charts, E_g at 1.14eV can be obtained for many values of pair (x,y). Therefore InGaAsP is can be also a good candidate for the well as it provides a high degree of freedom.

Now, regarding the strain, we observe that $InAs_xP_{1-x}$, when lattice-matched to GaAs, bears a strain of around 4.5% compressive for values of x at the target E_g. This is too high and InAsP must be rejected. On the other hand, InGaAs has an adequate strain for x<0.4. Because it reaches E_g=1.14eV while having small strain, InGaAs is a good candidate as well material for 1μm SOA. At last, InGaAsP, within the range of (x,y) with an energy gap of 1.14eV (x<0.5 and y>0.87), has a satisfactory strain. But its strain is larger than InGaAs and is the lowest for y=1, that is, when InGaAsP is actually InGaAs itself. Therefore, we choose $In_{0.27}Ga_{0.73}As$ for our quantum well structure. It is worth mentioning that InGaAs is chosen for the active region in many articles on laser structures at 0.98 or 1.05μm. See for instance [25], [27], [26], [22], [45] to cite a few. This is not surprising as this is the virtually the only possible choice.

Width: The material of the well being chosen, we can now select its width. Fig.44 show the wavelength corresponding to the first Eigen-energy of the transition pair, as a function of the width for InGaAs. When the well is thin, E_{21} is large and the wavelength short. This is consistent with eq. 5.2 of sect. 5.2. The figures shows that the width of the well can be clearly adjusted to fine-tune the operating wavelength of the OSA. It also shows that the wavelength converges to a constant when the width grows because the well starts behaving as a bulk. The maximum corresponds to the bandgap of InGaAs. Note that the chart suggests one could achieve much lower wavelengths with very thin wells. Therefore, one could use materials with lower E_g if thinner, to achieve the same target of 1um. However there is an actual limitation for practical fabrication considerations: the layer can not be too thin.
For now, we choose 5.5nm but it should be adjusted depending on exact required specifications for the SOA and the OPA, and depending of the finite potential gap of the well, which will be determined by the material of the barrier.

To conclude, we choose a well made in $\mathbf{In_{0.27}Ga_{73}As}$ with a **5.5nm** width. It has a compressive strain of **1.9%** on GaAs and a bandgap E_g**=1.12eV**.

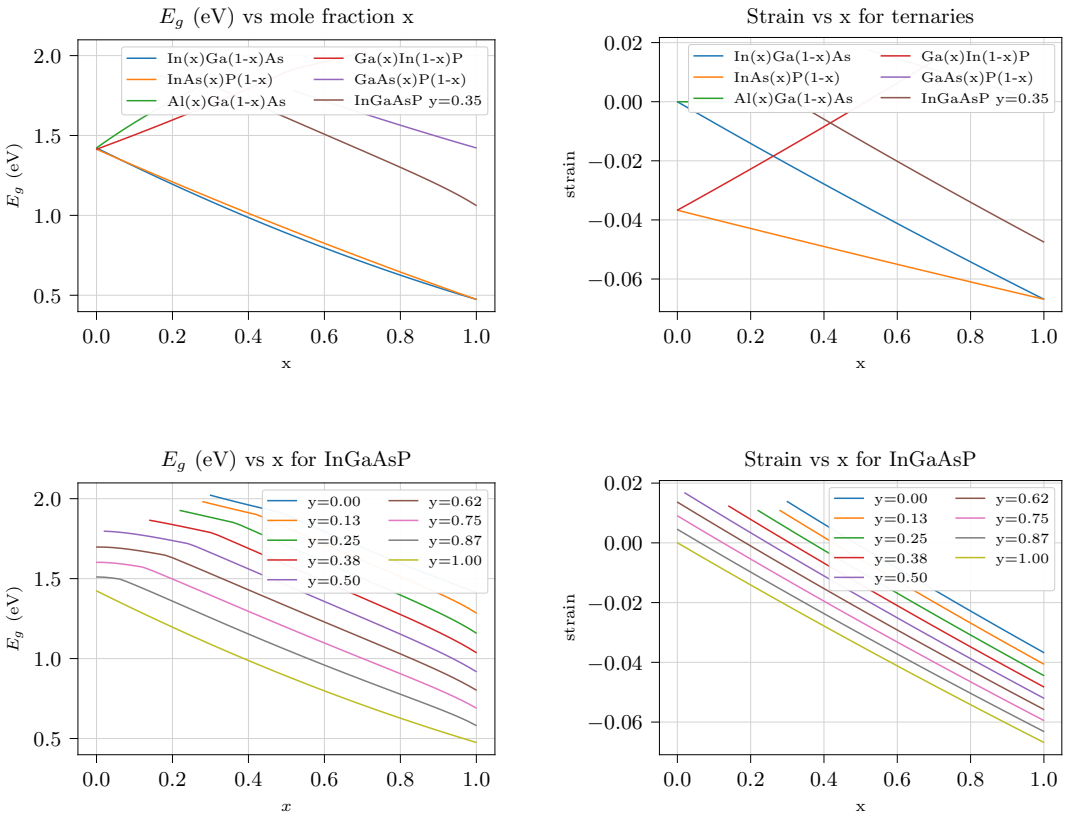

Figure 43: GaAs-matched band gap (left) and strain (right) of some ternary alloys and of $In_xGa_{1-x}As_yP_{1-y}$. Data points with indirect gap are excluded. The lower of $E_{c,hh}$ and $E_{c,lh}$ are displayed. (Python: Ternaries.py and InGaAsP.py)

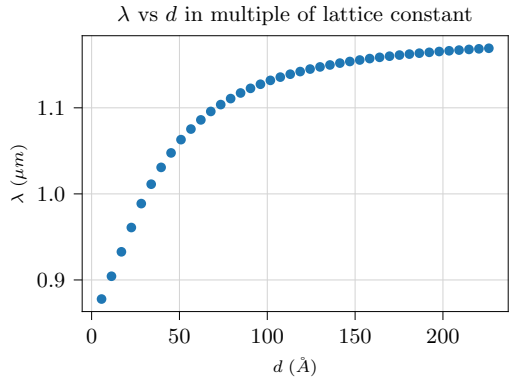

Figure 44: Wavelength of first Eigen-energy pair E_{21} for InGaAs as a function of the width of well. Each points are at multiples of the lattice constant a=5.65$\AA$ of GaAs.

7.4 Choice of Barrier

The first criteria for the choice of the material for barriers is that it must obviously have a larger bandgap than the well. To begin with, we would like to see how the gain and differential gain are affected by the bandgap of the barrier. Looking at fig. 43, we selected a few examples of alloys with various E_g sorted by descending order. Table 7 show their simulated differential gain a and material gain g. AlGaAs is added for reference as we seek alternative Al-free devices with similar properties. However, we see no obvious impact of the level of the barrier bandgap on a or g.

Barrier Alloy	Strain	E_g	Device N_θ	E	λ	a	g
	(%)	(eV)	(10^{12} cm^{-2})	(eV)	(μm)	(10^{15} cm^2)	(10^4 cm^{-1})
$Al_{0.35}Ga_{0.65}As$	-0.0	1.90	0.56	1.25	0.99	4.88	0.71
$In_{0.50}Ga_{0.50}P$	-0.1	1.90	0.71	1.25	0.99	3.72	0.71
$GaAs_{0.60}P_{0.40}$	1.5	1.82	0.60	1.25	0.99	4.59	0.70
$In_{0.40}Ga_{0.60}As_{0.35}P_{0.65}$	-0.6	1.71	0.70	1.24	1.00	3.75	0.70
$In_{0.30}Ga_{0.70}P$	-1.6	1.69	0.89	1.24	1.00	2.63	0.70
$GaAs_{0.80}P_{0.20}$	0.7	1.62	0.66	1.24	1.00	4.14	0.68
$In_{0.12}Ga_{0.88}As_{0.76}P_{0.24}$	0.0	1.57	0.60	1.23	1.01	4.46	0.69
$In_{0.60}Ga_{0.40}As_{0.40}P_{0.60}$	-2.2	1.46	1.19	1.22	1.02	1.38	0.66
GaAs	0.0	1.42	0.94	1.22	1.02	2.28	0.58

Table 7: Active region: $In_{0.27}Ga_{0.73}As$, strain=-1.9%, E_g=1.12eV. Impact of barrier gap and strain on λ and $\frac{dg}{dN}$ at the threshold carrier density level N_θ. g_0 is computed for a carrier density of $N = 10 \times 10^{12} cm^{-2}$ for a width of 55$\mathring{A}$. Rows are sorted by decreasing barrier gap. (Python: ExSQWTable1.py)

As we focus on SQW and remembering one of the considerations of sect, 7.2, we want 0 strain in the barrier. Therefore, we rather shift our attention to the four alloys of zero or near-zero strain listed in table 8. Concerning InGaAsP, we deduced from fig. 43 that its strain is null for $y = 1 - \frac{x}{0.495}$ for which the main characteristics are depicted in Fig. 45. Since all other parameters but the differential gain a are fairly constant over x, we chose the two values of x where a reaches its minimum or maximum: At x=0.12, and y= 0.76, we have the highest differential gain, reaching a=4.46 10^{15}cm^2. At x=0 and y=1, i.e. a simple GaAs alloy, we get the lowest differential gain a=2.28 10^{15}cm^2.

Barrier Alloy	Strain	E_g	Device N_θ	E	λ	a	g	P_{os}
	(%)	(eV)	(10^{12} cm^{-2})	(eV)	(μm)	(10^{15} cm^2)	(10^4 cm^{-1})	(mW)
$Al_{0.35}Ga_{0.65}As$	-0.0	1.90	0.56	1.25	0.99	4.88	0.71	9.99
GaAs	0.0	1.42	0.94	1.22	1.02	2.28	0.67	20.88
$In_{0.48}Ga_{0.52}P$	-0.3	1.88	0.72	1.25	0.99	3.66	0.71	13.33
$In_{0.12}Ga_{0.88}As_{0.76}P_{0.24}$	0.0	1.57	0.60	1.23	1.01	4.46	0.69	10.80

Table 8: Active region: $In_{0.27}Ga_{0.73}As$, strain=-1.9%, E_g=1.12eV. Impact of barrier gap and strain on λ and $\frac{dg}{dN}$ at the threshold carrier density level N_θ. g_0 is computed for a carrier density of $N = 10 \times 10^{12} cm^{-2}$ for a width of 55$\mathring{A}$. Rows are sorted by decreasing barrier gap. (Python: ExSQWTable2.py)

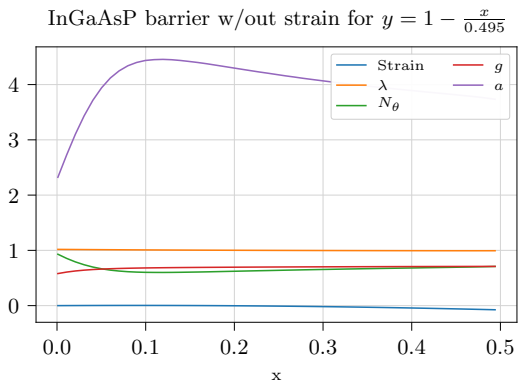

Figure 45: Strain (%), λ (μm), N_θ (10^{12}cm^{-2}), g (10^4 cm^{-1}) and a (10^{15} cm^2) of the SOA with no-strain $In_xGa_{1-x}As_yP_{1-y}$ barrier. The differential gain reaches a peak at 4.46 for $x = 0.12$ and $y = 0.76$ while the gain is flat. (Python: ExInGaAsPBarrier.py)

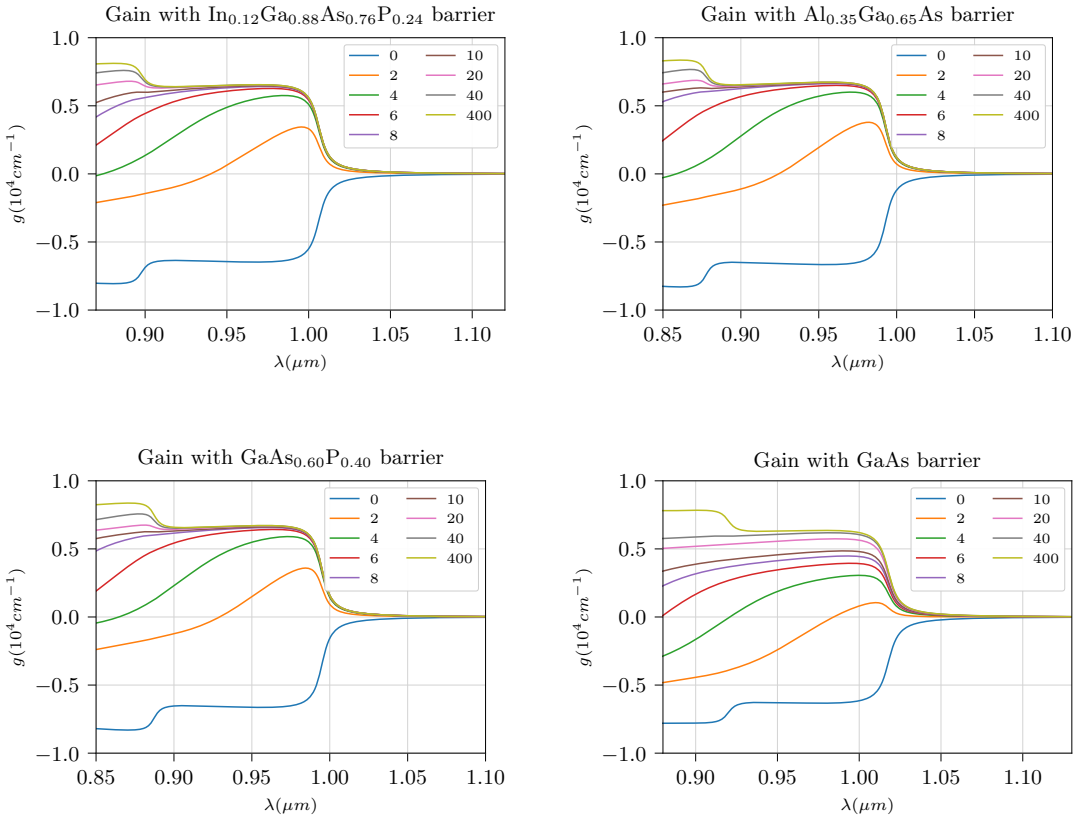

Figure 46: Gain spectra for several barriers versus the carrier density N. Some abscissa are shifted by up to 0.03μm to make the charts more easily comparable. In any case, the position of the first Eigen-energy can be fine-tuned to the specification of the SOA by changing the mole fraction of the well or its width.

7.5 Conclusion and discussion

Regarding the differential gain a and material gain g, table 8 shows that the well with $In_{0.12}Ga_{0.88}As_{0.76}P_{0.24}$ barrier exhibits very similar properties as with $Al_{0.35}Ga_{0.65}As$. Besides their material gain spectra shown in fig. 46 also have very much the same shape. At last, they both have 0 strain and are directly lattice-matched to GaAs. **In that regard, we conclude that $In_{0.27}Ga_{73}As$ / $In_{0.12}Ga_{0.88}As_{0.76}P_{0.24}$ can be proposed as an alternative to its equivalent with an AlGaAs barrier, for an Al-Free SQW SOA at 1μm.**

Now, the design should be adjusted in accordance with the application for which the SOA is meant.
For high-speed laser applications, a high differential gain improves the modulation response of the laser. Likewise, a large a would be recommended a good frequency response of a SOA for amplification of high-speed signals.
On the other hand and as derived in sect. 2.4, the output power saturation P_{o_s} of the SOA is inversely proportional to the differential gain a. P_{o_s} for each barrier candidate are shown in table 8 to typical values of A, B, C and w. We observe that the saturation output power is twice as high for GaAs barrier than both AlGaAs and InGaAsP barriers. Keeping that in mind, the increase of P_{o_s} also comes at the cost of a lower material gain. This may suggest that the GaAs would not be suited for applications where the injection current will be limited.
To conclude, the design of the SOA should be tine-tuned according to its desired properties and in particular about whether saturation matters.

This ends our work on the design of a 1um SOA with SQW active region.

Further work: Now that we understand precisely some of the main physical phenomena at stake in opto-electronics and that we have developed a foundation for a model library in Python, further study or research could be done. The Python library gives a great flexibility to run other sensitivity analysis while it might need further development as listed in sect. 8.1.

- For instance, it is known that **the differential gain is dependent on the structure of the active region**, be it, a bulk, a quantum well, or a strained quantum well. The code will easily allow one to run simulation and study this.
- Similarly, we know that **the width of the well also has an impact on a or on threshold injection**. This could be analyzed by plotting the chart of the gain g as a function of the carrier density for various wavelengths.
- The code is also ready for MQW and it would be interesting to **investigate to impact of the number of wells on the properties of the SOA**. From [19], distributing the carriers over N_w wells, the gain within each well is reduced by less than N_w times, but the modal gain is multiplied by nearly N_w times.
- **Current injection**: We know that for a SQW, most of the electrons coming from the injection current are going in the well except some that are lost. In the case of the MQW, the wells that are the nearest to the minus electrode (where electrons come) are the first served. There is no guarantee that each of the wells will contain the same carrier density, virtually creating a difference of Fermi energy between each well thus a difference in gain. This could lead to the modification of the light mode (e.g. a gaussian beam will not be gaussian anymore) and become problematic for some applications of SOA. MQW will therefore deserve a thorough study of the diffusion of electrons inside the active regions.

- **Confinement factor**: The confinement factor has not been dealt precisely int this work because the material gain of the active region is independent from it. In order to compute the final gain of the device with the rate equations, it is necessary however. As it was defined in sect. 2, the confinement factor needs a precise definition of the volume of the active region and the light.
- The geometry of MQW or asymmetric MQW have an impact as well on **the performance sensitivity of the device versus polarization** as discussed in [93], [94], [95], [96], [97], [98], [99], [100], [101] and [102].

8 Description of the Python library

This section describes the Python code developed for the purpose of this research. All equations used in algorithms are in this dissertation, which can be used as a documentation for the code. Comments are also provided in the code itself for ease of reading.
To avoid confusion, calculations are done using the International System of Units. Therefore, results must be converted to appropriate units only for display or charts.
We describe in details the main four Python files. Other less important files are listed in sect. 8.5.

8.1 Why a Python library?

A Python library offers a number of advantages:

- Even if one understands an equation and how it was derived, implementing the code is sometime the only way to clearly spot what are data are needed and what are the exact impact of parameters. Therefore, the code can be used **to learn or for teaching** purpose.
- If the code is properly documented, it is easy to know what are the model assumptions or the physical or mathematical approximation that have been made. Besides, **If the Python code fails, it is easy to go through it step by step.**
- **A Python library can evolve**. New models can be added, some models can be improved.
- With Python, it is easy to change parameters to compute charts, analyze the sensitivity of some properties as a function of parameters. This provides **a great flexibility to test ideas or assumptions** and get results quickly.

The code here is mostly limited to the computation of density of states, to solutions of some Schrödinger equations and to computation of material gain, but **it provides a good foundation for further development**. More models or algorithms could be added including for instance:

- A solver for the rate equations (A model has to be chosen or proposed first for multiple layer devices.)
- A model for non-radiative recombination and spontaneous emissions to be included in rate equation model.
- Model for other losses such as current and photon loss.
- Ab initio methods or $\mathbf{k} \cdot \mathbf{p}$ method for better band calculation.
- Model for heat diffusion and its impact on the dynamics of devices.

8.2 Settings.py

The paths of the folders for charts in pdf files and for csv files (binary alloys and bowing parameters) that contain semiconductor data must be specified in Settings.py. The format in pdf for figures was found to be the most efficient for quality and size for inclusion in LaTeX documents.
Notes: When charts are saved to pdf files, python might display some warnings that can be discarded.

8.3 Alloy.py

This file contains the definition of the Alloy class that implements:

- Creation of binary alloy by reading data from csv files.
- Creation of ternary and quaternary alloys by the interpolation method described in sect. 3.5 of data of two binary alloys and four ternary alloys respectively. Linear interpolations are done with the addition and multiplication operator described below. For example, the ternary AB_xC_{1-x} is initiated by a single instruction, x * AB + (1.0 - x) * AC, where AB and AC are two binary alloys. Then, bowing adjustments are done.
- The addition operator between two alloys. The addition creates a new alloy whose parameters are the sum of the parameters of the two alloys.
- The operator for the multiplication of an alloy by a scalar. It creates a new alloy whose parameters are the parameters of the alloy multiplied by a scalar.
- The match method that matches the alloy to a given lattice constant. It computes the conduction and heavy/light holes valence bands energies, aligned by electron affinities or average band energies, as well as the effective masses as in sect. 3.5. The code checks whether the strain is excessive of the gap indirect.
- Some consistency checks are also done, for instance to prevent creating an alloy with an impossible combination of III/V groups elements.

An example of the class usage is given in fig. 47. Note the code can take into account the temperature for the calculation of Fermi statistics but the Alloy class is not. It only computes parameter at room temperature for now. (T=300K)

```
substrate = Alloy.binary('Ga', 'As')
active = Alloy.ternary('As', 'In', 'Ga', 0.27)
active.match(substrate.a, alignment='Affinity', exception_if_indirect_gap=True)
```

Figure 47: Definition of GaAs binary substrate and $In_{0.27}Ga_{0.73}As$ ternary and matching of the latter to the lattice constant of GaAs.

8.4 MultilayerDevice.py and DiscreteEigen.py

MultilayerDevice.py contains the definition of two Python classes: the MultilayerDevice class and the Band class. The MultilayerDevice class constructs an object from a list of Alloy objects (that must be matched to the relevant lattice constant) and a list of widths. The initialization creates five objects of the class Band:

- 3 for the conduction, heavy-hole and light-hole bands: They will be used to compute the quasi-Fermi levels.
- 2 for transition pairs conduction-heavy-holes and conduction-light-holes: They will be used for the computation of the reduced density terms of the gain equation.

When an object of the Band class is created, the code sets the proper potentials and masses for the Schrödinger equation 5.12 corresponding to the band of interest. For instance, for the conduction-heavy-bands, the potential in each layer is set as the band gap $E_c - E_{v,hh}$ and the mass $m^{<100>}$ and m^t as the reduced mass. Then, the discretized Schrödinger equation 5.14 is solved at order 0 (that is eq. 5.11) by calling the function MultipleWells of DiscreteEigen.py which returns

- The Eigen-energies E_{n_x} of the system.
- The average masses m^t of eq. 5.15 and 5.23.
- The probability of each layer for each quantum number n_x of eq. 6.9.

The MultilayerDevice class implements the following functions among others:

- carrier_density: A function that returns the carrier density of sect. 4.6, using the state density of eq. 5.19 for a given Fermi level.
- fermi_level: A function that returns the implied quasi-Fermi level from the density N using the carrier_density function.
- gain: A function that computes the gain of eq. 6.8 for an array of $h\nu$ and for given quasi-Fermi levels E_{F_c} and E_{F_v}.
- gain_characteristics: A function that returns the threshold carrier density N_θ, the gain g at a given density N, the differential gain a computed by finite difference at $N_t h$ and saturation output power P_{o_s} of eq. 2.18. Everything is compute for a photon energy level 0.01 eV above the first Eigen-Energy of the well conduction-heavy-holes.
- A few functions to display charts of density of states, carrier density, quasi-Fermi levels, gain spectrum.
- view_check_k_selection_rule: A function that outputs data to check the compliance with the k-selection rule as in sect. 6.3.4.
- display_bands: A function to display the band-offset alignment chart as in fig. 41a.

Fig. 48 shows an example of application of the MultilayerDevice class to display the spectrum of fig. 41.

```
# Create two alloys
GaAs = Alloy.binary('Ga', 'As')
AlGaAs = Alloy.ternary('As', 'Al', 'Ga', 0.2)

# Align one on the other
strain = AlGaAs.match(GaAs.a, alignment=alignment, exception_if_indirect_gap=True)

# Create a multi-layer device
layer_alloys = np.array([AlGaAs, GaAs, AlGaAs])
layer_widths = np.array([100, 80, 100]) * constants.angstrom
device = MultilayerDevice(layer_alloys, layer_widths)

# Draw the chart of band offset alignment
device.display_bands(show_charts)
# Draw the spectrum
device.chart_gain(show_charts, convolve=True, apply_width_of_cavities=True, polarization='TE',
                  lambda_min=0.67, lambda_max=0.87, yrange=1.5)
```

Figure 48: Definition of a single quantum well with a GaAs well and AlGaAs barriers matched on GaAs. Display the band offset alignment and the spectrum. From: ExGaAsAlGaAsSpectrum.py

8.5 List of Python files

Note that four of the older Python files are using simple semiconductor data defined in SemiconductorData.py. They are indicated in italic in the table. Ideally, they should be migrated to use the Alloy class instead.

Main files	**Description**
Settings.py	Definition of paths, data file names and parameters for charts in pdf format. C.f. sect. 8.2.
Alloy.py	Alloy class for binary, ternary and quaternary compounds described in sect. 8.3.
MultilayerDevice.py	Definition of the Band and Multilayer classes described in sect. 8.4.
DiscreteEigen.py	Resolution of the discretized Schrödinger equation 5.11.
Fermi.py	Fermi statistic, Fermi-Dirac function and inverse, Solver for Fermi level from carrier density of sect. D.
Lineshape.py	Gaussian, Lorentzian and Chinn lineshape calculation and charts of sect. 6.1.4.
FiniteWell.py	Solver and chart for the quasi-analytical solutions for finite quantum well of sect. 5.3.
GainBulk.py	Calculation of gain for bulk in sect. 6.1.7.
GainQW.py	Computation of gain for a single quantum well of sect. 6.2 using the finite potential quai-analytical solution of FiniteWell.py
FermiStatistics.py	Simple charts for Fermi Statistics and Bulk density of states.
StateAndCarrierDensity.py	Computation of density of states for bulk, well, wires and of carrier densities.

Utilities	**Description**
Charts.py	2D line charts for display on monitor or ouput in pdf format.
SemiconductorData.py	Semiconductor data for GaAs and AlGaAs. This definition of alloy parameter is obsolete. One should use the Alloy class instead.

Examples	**Description**
ExSQWTable1.py	Code for table 7.
ExSQWTable2.py	Code for table 8.
ExGaAsAlGaAsSpectrum.py	Code for fig. 16
ExTernaries.py	Code for upper fig. 43
ExInGaAsP.py	Code for lower part of fig. 43
ExInGaAsPBarrier.py	Code for the fig. 45.
ExFiguresForThesis.py	Computation of various charts for the figures of this document.

Appendix

A $\mathcal{H}'^{\dagger} = \frac{q}{2m_0}\mathcal{A}^*(\mathbf{r})\hat{\mathbf{e}}\cdot\mathbf{p}$

This section provides proves a results used in sect. 3.3.2.

First, we remind a few definitions and properties related to Hilbert space:

1. The Hermitian adjoint $\hat{O}^\dagger$ of an operator $\hat{O}$ is such that $\langle\psi|\hat{O}|\phi\rangle = \left\langle \hat{O}^\dagger|\psi\rangle \middle| \phi \right\rangle$.
2. An operator $\hat{O}$ is Hermitian or self-adjoint iif $\hat{O}^\dagger = \hat{O}$.
3. The expression of $\langle\psi|\hat{O}|\phi\rangle$ in integral form is $\langle\psi|\hat{O}|\phi\rangle = \int \psi(\mathbf{r})^*\hat{O}(\mathbf{r})\phi(\mathbf{r})d\mathbf{r}$.
4. $\langle\lambda\psi|\phi\rangle = \lambda^*\langle\psi|\phi\rangle$ with $\lambda \in \mathbb{C}$ and * denotes the complex conjugate.
5. $\langle\psi|\lambda\phi\rangle = \lambda\langle\psi|\phi\rangle$ with $\lambda \in \mathbb{C}$.

Lemma: $\hat{\mathbf{e}}\cdot\mathbf{p}$ is Hermitian

Proof. In one dimension, we first show that $\mathbf{p} = -i\hbar\frac{\partial}{\partial x}$ is Hermitian. Let compute $\langle\psi|\mathbf{p}|\phi\rangle$ by integration by parts:

$$\langle\psi|\mathbf{p}|\phi\rangle = \int \phi^*(x)(-i\hbar\frac{\partial\phi(x)}{\partial x})dx = -i\hbar\int \phi^*(x)\frac{\partial\phi(x)}{\partial x}dx = -i\hbar\big\{[\phi^*(x)\phi(x)] - \int \frac{\partial\psi^*(x)}{\partial x}\phi(x)dx\big\}$$

Assuming that $\phi^*(x)\phi(x)$ vanishes at $\pm\infty$,

$$\langle\psi|\mathbf{p}|\phi\rangle = \int i\hbar(\frac{\partial\psi(x)}{\partial x})^*\phi(x)dx = \int(-i\hbar\frac{\partial\psi^*(x)}{\partial x})^*\phi(x)dx = \int(\mathbf{p}\psi(x))^*\phi(x)dx = \langle\mathbf{p}\,|\psi\rangle|\phi\rangle$$

Therefore $\mathbf{p}$ is Hermitian. Furthermore, we can derive the same result for $p_x = \frac{\partial}{\partial x}$, $p_y = \frac{\partial}{\partial y}$ and $p_z = \frac{\partial}{\partial z}$ in three dimensions.
Finally, $\hat{\mathbf{e}}\cdot\mathbf{p}$ is a linear combination of Hermitian operators given as

$$\hat{\mathbf{e}}\cdot\mathbf{p} = -i\hbar\left(e_x p_x + e_y p_y + e_z p_z\right)$$

where e_x, e_y and e_y are the coordinates of $\hat{\mathbf{e}}$. Therefore, it is itself self-adjoint. ■

Lemma: $\left(\lambda\hat{O}\right)^\dagger = \lambda^*\hat{O}^\dagger$ for $\lambda \in \mathbb{C}$.

Proof. Let's calculate $\langle\psi|\lambda\hat{O}|\phi\rangle$.

$$\langle\psi|\lambda\hat{O}|\phi\rangle = \left\langle\psi\middle|\lambda\hat{O}\,|\phi\rangle\right\rangle = \lambda\left\langle\psi\middle|\hat{O}\,|\phi\rangle\right\rangle = \lambda\left\langle\hat{O}^\dagger\,|\psi\rangle\middle|\phi\right\rangle = \left\langle\lambda^*\hat{O}^\dagger\,|\psi\rangle\middle|\phi\right\rangle$$

Besides, we also have

$$\langle\psi|\lambda\hat{O}|\phi\rangle = \left\langle(\lambda\mathcal{O})^\dagger\,|\psi\rangle\middle|\phi\right\rangle$$

Therefore $(\lambda\mathcal{O})^\dagger = \lambda^*\hat{O}^\dagger$. ■

Lemma: If $\mathcal{H}' = \frac{q}{2m_0}\mathcal{A}(\mathbf{r})\hat{\mathbf{e}}$ with $\mathcal{A}(\mathbf{r}) \in \mathbb{C}$, then $\mathcal{H}'^{\dagger} = \frac{q}{2m_0}\mathcal{A}^*(\mathbf{r})\hat{\mathbf{e}} \cdot \mathbf{p}$

Proof. As per the second lemma above, we have:

$$(\mathcal{A}\hat{\mathbf{e}} \cdot \mathbf{p})^{\dagger} = \mathcal{A}^* (\hat{\mathbf{e}} \cdot \mathbf{p})^{\dagger}$$

Besides, as per the first lemma, we have:

$$(\mathcal{A}\hat{\mathbf{e}} \cdot \mathbf{p})^{\dagger} = \mathcal{A}^* (\hat{\mathbf{e}} \cdot \mathbf{p})$$

■

B Fermi Golden Rule

We give a summary of the Fermi's Golden rule, whose derivation can be found in many references. We adopt the presentation of [66].
Consider the time-dependent Schrödinger equation of an electron in a system whose Hamiltonian H_0 is perturbed by a time-dependent term $H'(\mathbf{r}, t)$ caused for instance by the electromagnetic field of a photon beam of frequency ω:

$$i\hbar\frac{\partial\psi(\mathbf{r}, t)}{\partial t} = (\mathcal{H}_0 + \mathcal{H}'(\mathbf{r}, t))\,\psi(\mathbf{r}, t) \tag{B.1}$$

where $\mathcal{H}'$ is applied from $t \geq 0$ and takes the form

$$\mathcal{H}'(\mathbf{r}, t) = \mathcal{H}'(\mathbf{r})e^{i\omega t} + \mathcal{H}'^{\dagger}(\mathbf{r})e^{-i\omega t} \tag{B.2}$$

Let the solutions of the unperturbed system be

$$\phi_n(\mathbf{r}, t) = \phi_n^s(\mathbf{r})e^{-i\frac{E_n}{\hbar}t}$$

where the superscript s indicates reference to the stationary equation. The set of solutions ϕ_n forms an orthonormal basis of the solutions of the unperturbed system but not necessarily of the perturbed system. Nevertheless we project solutions of B.1 on it:

$$\psi(\mathbf{r}, t) = \sum_n a_n(t)\phi_n^s(\mathbf{r})e^{-i\frac{E_n}{\hbar}t}$$

Eq. B.1 becomes

$$i\hbar\sum_n \frac{da_n(t)}{dt}\phi_n^s(\mathbf{r})e^{-i\frac{E_n}{\hbar}t} + i\hbar\sum_n a_n(t)\frac{\partial\phi(\mathbf{r}, t)}{\partial t} = \sum_n a_n(t)\mathcal{H}'(\mathbf{r}, t)\phi_n^s(\mathbf{r})e^{-i\frac{E_n}{\hbar}t} + \sum_n a_n(t)\mathcal{H}_0 a_n(t)$$

As the second terms on each side are equal (they are a linear combination of unperturbed Schrödinger applied to its solutions), it simplifies as

$$i\hbar\sum_n \frac{da_n(t)}{dt}\phi_n^s(\mathbf{r})e^{-i\frac{E_n}{\hbar}t} = \sum_n a_n(t)\mathcal{H}'(\mathbf{r}, t)\phi_n^s(\mathbf{r})e^{-i\frac{E_n}{\hbar}t}$$

Taking the Hermitian inner product by the left of the equation with $\phi_m(\mathbf{r})$:

$$i\hbar\sum_n \frac{da_n(t)}{dt}e^{-i\frac{E_n}{\hbar}t}\int_{\mathbf{r}} \phi_m^{s*}(\mathbf{r})\phi_n^s(\mathbf{r})d\mathbf{r} = \sum_n a_n(t)e^{-i\frac{E_n}{\hbar}t}\int_{\mathbf{r}} \phi_m^{s*}(\mathbf{r})\mathcal{H}'(\mathbf{r}, t)\phi_n^s(\mathbf{r})d\mathbf{r}$$

Using $\langle \phi_m^s | \phi_n^s \rangle = \delta_{m,n}$, we obtain

$$\frac{da_m(t)}{dt} = -\frac{i}{\hbar} \sum_n a_n(t) \mathcal{H}'_{mn}(t) e^{i\frac{E_m - E_n}{\hbar}t} \tag{B.3}$$

where $H'_{mn}(t)$ is the matrix element

$$\begin{aligned} H'_{mn}(t) = \langle \phi_m^s | H'(\mathbf{r},t) | \phi_n^s \rangle &= \int_{\mathbf{r}} \phi_m^{s*}(\mathbf{r}) H'(\mathbf{r},t) \phi_n^s(\mathbf{r}) d\mathbf{r} = \int_{\mathbf{r}} \phi_m^{s*}(\mathbf{r}) \left(\mathcal{H}'(\mathbf{r}) e^{i\omega t} + \mathcal{H}'^{\dagger}(\mathbf{r}) e^{-i\omega t} \right) \phi_n^s(\mathbf{r}) d\mathbf{r} \\ &= e^{i\omega t} \int_{\mathbf{r}} \phi_m^{s*}(\mathbf{r}) \mathcal{H}'(\mathbf{r}) \phi_n^s(\mathbf{r}) d\mathbf{r} + e^{-i\omega t} \int_{\mathbf{r}} \phi_m^{s*}(\mathbf{r}) \mathcal{H}'^{\dagger}(\mathbf{r}) \phi_n^s(\mathbf{r}) d\mathbf{r} \\ &= e^{i\omega t} \langle \phi_m^s | \mathcal{H}'(\mathbf{r}) | \phi_n^s \rangle + e^{-i\omega t} \langle \phi_m^s | \mathcal{H}'^{\dagger}(\mathbf{r}) | \phi_n^s \rangle = e^{i\omega t} H'_{mn} + e^{-i\omega t} H'^{\dagger}_{mn} \end{aligned}$$

with $H'_{mn} = \langle \phi_m^s | \mathcal{H}'(\mathbf{r}) | \phi_n^s \rangle \in \mathbb{C}$ and $H'^{\dagger}_{mn} = \langle \phi_m^s | \mathcal{H}'^{\dagger}(\mathbf{r}) | \phi_n^s \rangle \in \mathbb{C}$.
Using perturbation, we look for solutions of eq. B.3 of the form

$$a_n(t) = a_n^{(0)}(t) + \lambda a_n^{(1)}(t) + \lambda^2 a_n^{(2)}(t) + \cdots$$

and we note $\mathcal{H} = \mathcal{H}_0 + \lambda \mathcal{H}'$ where λ can be set to 1. Substituting this expression into eq. B.3 and identifying the terms of order 0 and 1 in λ gives

$$\frac{d}{dt} a_m^{(0)}(t) = 0 \tag{B.4}$$

$$\frac{d}{dt} a_m^{(1)}(t) = -\frac{i}{\hbar} \sum_n a_n^0(t) H'_{mn}(t) e^{i\frac{E_m - E_n}{\hbar}t} \tag{B.5}$$

At order 0, the coordinates of the particle on the basis functions are constant. This is expected because $\mathcal{H} = \mathcal{H}_0$.

Now, let's consider that the particle is in state i initially at $t = 0$ and see how it evolves to a final state f. As we have $a_m^{(0)}(t) = \delta_{m,i}$. Eq. B.5 becomes

$$\frac{d}{dt} a_f^{(1)}(t) = -\frac{i}{\hbar} H'_{fi}(t) e^{i\frac{E_j - E_i}{\hbar}t} = -\frac{i}{\hbar} \left(H'_{fi} e^{i(\omega_{fi} + \omega)t} + H'^{\dagger}_{fi} e^{i(\omega_{fi} - \omega)t} \right) \tag{B.6}$$

with $\omega_{fi} = \frac{E_f - E_i}{\hbar}$.
$a_f^{(1)}(t)$ is obtained by integration of eq. B.6. We are interested by its square modulus which gives the probability of the electron to be in state f. Borrowing from sect. 3.5 of [66], under the assumption that the photon frequency ω is near $\pm\omega_{fi}$ and that interaction time t is long, the probability is approximated as

$$|a_f^{(1)}(t)|^2 = \frac{2\pi t}{\hbar^2} |H'_{fi}|^2 \left(\delta(\omega_{fi} - \omega) + \delta(\omega_{fi} + \omega) \right)$$

and its derivatives versus time, i.e. the rate of transition from state i to state f is given as

$$W_{i \to f} = \frac{2\pi}{\hbar} |H'_{fi}|^2 \left(\delta(E_f - E_i - \hbar\omega) + \delta(E_f - E_i + \hbar\omega) \right)$$

From this equation, we make the following observations. The transition from one Eigen-state (solution of the stationary Schrödinger equation) to another is only possible if the state energies are separated by the energy of the photon. If $E_f = E_i + \hbar\omega$, only the first term is non null, the final state of the electron has a higher energy as it absorbed the photon. If $E_f = E_i - \hbar\omega$, only the second term is non null, the final state of the electron has a lower energy and emits another photon. There also is a probability that the state of the electron does not change from the zero order part of the solution from the 0 order equation.

C The $\mathbf{k}\cdot\mathbf{p}$ method

There are several methods to solve the equation for one electron Hamiltonian of eq. 3.2. The $\mathbf{k}\cdot\mathbf{p}$ method is one (c.f. [52], [58], [57]). Applying the Hamiltonian to $\phi_{n,k}$ gives

$$\left(\frac{\mathbf{p}^2}{2m}+V(\mathbf{r})\right)e^{i\mathbf{k}\cdot\mathbf{r}}u_n(\mathbf{k},\mathbf{r})=E_{n,\mathbf{k}}e^{i\mathbf{k}\cdot\mathbf{r}}u_n(\mathbf{k},\mathbf{r}) \tag{C.1}$$

Using the definition of $\mathbf{p}$ and $\mathbf{p}^2$ as

$$\mathbf{p}=\begin{pmatrix}p_x\\p_y\\p_z\end{pmatrix}=-i\hbar\begin{pmatrix}\frac{\partial}{\partial x}\\\frac{\partial}{\partial y}\\\frac{\partial}{\partial z}\end{pmatrix},\quad \mathbf{p}^2=\mathbf{p}\cdot\mathbf{p}=-\hbar^2\left(\frac{\partial^2}{\partial x^2}+\frac{\partial^2}{\partial y^2}+\frac{\partial^2}{\partial z^2}\right)$$

and taking the partial derivatives of the Bloch function with respect to x gives

$$\frac{\partial e^{i\mathbf{k}\cdot\mathbf{r}}u_n(\mathbf{k},\mathbf{r})}{\partial x}=e^{i\mathbf{k}\cdot\mathbf{r}}\left(\frac{\partial u_n(\mathbf{k},\mathbf{r})}{\partial x}+ik_xu_n(\mathbf{k},\mathbf{r})\right)$$

The term in x of $\frac{\mathbf{p}^2}{2m}$ can be written as:

$$\begin{aligned}-\frac{\hbar^2}{2m}\frac{\partial^2 e^{i\mathbf{k}\cdot\mathbf{r}}u_n(\mathbf{k},\mathbf{r})}{\partial x^2}&=-\frac{\hbar^2}{2m}e^{i\mathbf{k}\cdot\mathbf{r}}\left(\frac{\partial^2u_n(\mathbf{k},\mathbf{r})}{\partial x^2}+2ik_x\frac{\partial u_n(\mathbf{k},\mathbf{r})}{\partial x}-k_x^2u_n(\mathbf{k},\mathbf{r})\right)\\&=e^{i\mathbf{k}\cdot\mathbf{r}}\left(\frac{1}{2m}p_x^2\left(u_n(\mathbf{k},\mathbf{r})\right)+\frac{\hbar}{m}k_xp_x\left(u_n(\mathbf{k},\mathbf{r})\right)+\frac{\hbar^2k_x^2}{2m}u_n(\mathbf{k},\mathbf{r})\right)\end{aligned}$$

Therefore developing the above Schrödinger equation yields

$$\mathcal{H}_{\mathbf{k}}u_{n,\mathbf{k}}=E_{n,\mathbf{k}}u_{n,\mathbf{k}},\quad\text{with}\quad\mathcal{H}_{\mathbf{k}}=\frac{\mathbf{p}^2}{2m}+\frac{\hbar\mathbf{k}\cdot\mathbf{p}}{m}+\frac{\hbar^2\mathbf{k}^2}{2m}+V(\mathbf{r})$$

where $\mathbf{k}\cdot\mathbf{p}=k_x(-i\hbar\frac{\partial}{\partial x})+k_y(-i\hbar\frac{\partial}{\partial y})+k_z(-i\hbar\frac{\partial}{\partial z})$

Earlier paper from Cardona is cited as [64]. Examples of $\mathbf{k}\cdot\mathbf{p}$ method applied to GaAs are given in [70], [71], [72], [73], [74].
To be continued.

D Fermi-Dirac function and generalized Gauss-Laguerre quadrature

The generalized Gauss-Laguerre quadrature[33] provides approximation of integrals of the form:

$$\int_0^{+\infty}x^\alpha e^{-x}f(x)dx\approx\sum_i w_if(x_i)$$

where the weights w_i and abscissas x_i are chosen so that the sum is exact if f is a polynomial of degree less than $2n-1$. if f is not a polynomial but is well approximated by a polynomial, the sum gives an accurate estimate of the integral.

[33] Implemented in Fermi.py

The generalized Gauss-Laguerre quadrature with $\alpha = \frac{1}{2}$ is very well suited for this integral because a) the domain of integration is $\mathbb{R}^+$ and b) the exponential term tends to e^{-x}.
Before applying the quadrature, we multiply and divide the integrand of $F_{1/2}$ by e^{-x}

$$F_{1/2}(v) = \int_0^{+\infty} x^\alpha e^{-x} f(x) dx$$

where $f(x) = \frac{1}{e^{-x}+e^{-v}}$.
Convergence and comparison with closed-form described in appendix 2 of [19] are illustrated in fig. 49 and 50

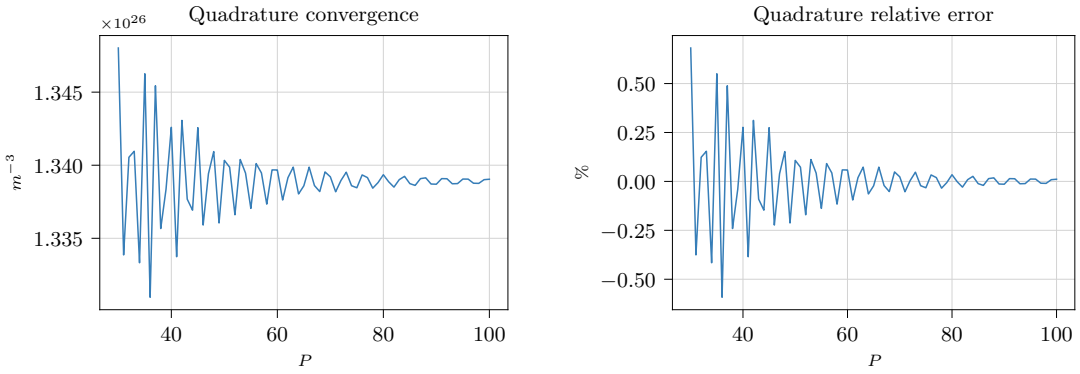

Figure 49: Computation of $N_c(E_{F_c})$ by generalized Gauss-Laguerre quadrature, for $E_F = 1.424eV$, $m_c = 0.067m_0$ and $K = 300K$. The error is relative to the value calculated with 180 points.

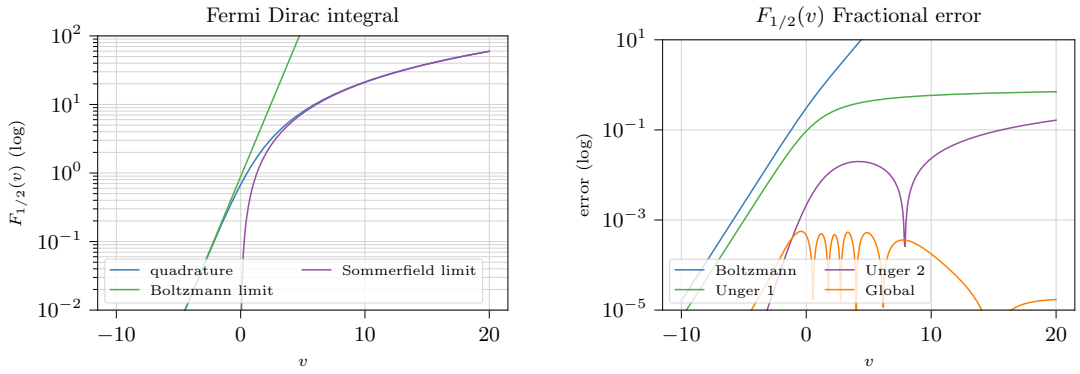

Figure 50: Fermi-Dirac integral calculation by quadrature and closed-forms. Errors are with respect to values computed with 180 points quadrature. As the later is itself erroneous, the shape is slightly off versus [19].

References

[1] S.Onoduka, Design and fabrication of Semiconductor Optical Amplifier for High Power Optical Phased Array, Master Thesis, University of Tokyo, 2020

[2] V.Y. Aleshkin et al., Monolithically integrated InGaAs/GaAs/AlGaAs quantum well laser grown by MOCVD on exact Ge/Si(001) substrate, Appl. Phys. Lett. 106, 061111, 2016

[3] Wight D. R., Heaton J. M., Hughes B. T., Birbeck J. C. H., Hilton K. P., Taylor D. J., Novel phased array optical scanning device implemented using GaAs/AlGaAs technology, Appl. Phys. Lett. 59, 899, 1991.

[4] Walker R. G., Cameron N. I., Zhou Y., Clements S. J., Optimized Gallium Arsenide Modulators for Advanced Modulation Formats, IEEE Journal of Selected topics in Quantum Electronics, vo. 19, no. 6, 2013

[5] Lammlin, M.: GaAs-Based Semiconductor Optical Amplifiers with Quantum Dots as an Active Medium, Doctoral thesis, Mathematik und Naturwissenschaften der Technischen Universität Berlin, (2007)

[6] Schubert, C., Ludwig, R., Weber, H-G.: High-speed optical signal processing using semiconductor optical amplifiers, Journal of Optical and Fiber Communications Reports, Vol. 2, 171-208, (2004)

[7] Haridim, M., Lembrikov, B.I., Ben-Ezra, Y. : Semiconductor Optical Amplifiers, Advances in Optical Amplifiers, Paul Urquhart, IntechOpen, DOI: 10.5772/13415, (2011)

[8] Venkataraman, V.: Optical Amplifiers, Course, Institute for Optical Sciences, University of Toronto

[9] Bonk, R.: Linear and Nonlinear Semiconductor Optical Amplifiers for Next-Generation Optical Networks, Dissertation, Karlsruhe Institute of Technology (KIT), Institute of Photonics and Quantum Electronics (IPQ), KIT Scientific Publishing (2013)

[10] Marculescu, A.: Semiconductor Optical Amplifiers: Modeling, Signal Regeneration and Conversion, Doctoral thesis, ETH Zürich Series in Electromagnetic Fields, Vol. 7, (2018)

[11] Connelly, M. J.: Dept. Electronic and Computer Engineering, University of Limerick, (2004)

[12] Leuthold, J., Bonk, R., Vallaitis, T., Marculescu, A., Freude, W., Meuer, C. , Bimberg, D., Brenot, R., Lelarge, F., Duan, G.-H.: Linear and Nonlinear Semiconductor Optical Amplifiers, Institute of Photonics and Quantum Electronics, Karlsruhe Institute of Technology, et al., Optical Networking and Communication Conference, OFC/NFOEC 2010

[13] Spiekman, L.: Economics and markets of semiconductor optical amplifiers, IEEE, 11th International Conference on Transparent Optical Networks, (2009)

[14] Oh, W. Y.: Optical Coherence Tomography for Clinical Applications, Smart Sensors for Health and Environment Monitoring, KAIST Research Series, Springer (2015)

[15] Kaspar, P., et al: Hybrid III-V/silicon SOA for photonic integrated circuits, Proceedings of SPIE - The International Society for Optical Engineering, (2014)

[16] Harrisson P., Quantum Wells, Wires and Dots: Theoretical and Computational Physics of Semiconductor Nanostructures, 5th edition, 978-1118923368, John Wiley, (2016)

[17] Harrisson P., Jovanovic V.D. , Strained Quantum Wells, 5th edition, 978-1118923368, John Wiley, (2016).

[18] Neamen D. A., Semiconductors Physics and Devices, Basic Principles, 4th edition, 978-0073529585, Mc Graw Hill, (2011)

[19] Coldren L. A., Corzine S. W., Masanovic M. L., Diode Lasers and Photonic Integrated Circuits, 2nd edition, 978-0470484128, John Wiley, (2012)

[20] Mitin V. V., Sementsov D. I., Vadigov N. Z., Quantum Mechanics for Nanostructures, 1st edition, 978-0521763660, Cambridge University Press, (2011)

[21] Kasap S., Capper P., Springer Handbook of Electronic and Photonic Materials, Springer, 978-0-387-26059-4 (2006)

[22] Fukunaga T., Wada M., Hayakawa T., Reliable operation of strain-compensated 1.06 μm InGaAs/InGaAsP/GaAs single quantum well lasers, Appl. Phys. Lett. 69, 248 (1996)

[23] Tanemura T., Lecture, 半導体集積フォトニクス（後半）大6回目、東京大学、電気系工学専攻 , 2019/7/2

[24] Hayakawa T., Akinaga F., Kuniyasu T., Matsumoto K., Fukunaga and T. , Highly reliable and high-power operation of 1.05 μm InGaAs/GaAsP strain-compensated single-quantum-well laser diodes for pumping Tm-doped fiber amplifiers, Optical Fiber Communication Conference, 2002, 1-55752-700-8

[25] Akinaga F., Kuniyasu T., Matsumoto K., Fukunaga T., Hayakawa T., 350mW reliable operation in fundamental transverse-mode InGaAs (λ=1.05 μm)= GaAsP strain-compensated laser diodes, Electronics Letters, Vol. 39, Issue 1, (2003), 10.1049/el:20030081

[26] Duan L. H., Fang L., Zhang J., Zhou Y., Guo H., Luo Q. C., Zhang S. F., Fabrication and characteristics of high speed InGaAs/GaAs quantum-wells superluminescent diode emitting at 1053 nm, Semicond. Sci. Technol. 29 (2014), 10.1088/0268-1242/29/5/05500

[27] Li X., Duan L. H., Zhou Y., Wei Z. R., Strained InGaAs/GaAs Quantum-Well Laser Emitting at 1054 nm, J Supercond Nov Magn (2010) 23: 937–939, 10.1007/s10948-010-0741-9

[28] Ohgoh T., Mukai A., Yaguchi ., Asano H., Demonstration of 1.0 μm InGaAs High-Power and Broad Spectral Bandwidth Superluminiscent Diodes by Usin Dual Quantum Weel Structure, Appl. Phys. Express 6 (2003), 10.7567/APEX.6.014101

[29] Guol S-H., Chou, M-G., Yang Y-J., Sun C-K., Shi J-W., GaAs-Based Transverse Junction Superluminescent Diodes With Strain-Compensated InGaAs–GaAsP Multiple-Quantum-Wells at 1.1-μm Wavelength, IEEE Photonics Technology Letters, Vol. 22, No. 12, (2010)

[30] Kawasaki K., Yamamura S., Takemoto A., Yagi T., Mitsui Y., High-Power and Highly Reliable 1020-nm Ridge Waveguide Laser Diodes With Small Aspect Ratio as a Pumping Source for Praseodymium-Doped Fiber Amplifiers, IEEE Photonics Technology Letters, Vol. 15, No. 5, (2003)

[31] Schlenker D., Pan Z., Miyamoto T.,Koyama F., Iga K., Effect of Surface Quality on Overgrowth of Highly Strained GaInAs/GaAs Quantum Wells and Improvement by a Strained Buffer Layer, Jpn. J. Appl. Phys. Vol. 38 (1999) pp. 5023–5027

[32] Li H., Wolf P., Moser P., Larisch G., Lott J. A., Bimberg D., Temperature-Stable, Energy-Efficient, and High-Bit Rate Oxide-Confined 980-nm VCSELs for Optical Interconnects, IEEE Journal of slected topics in quantum electronics,vol. 21, no. 6, 2015

[33] Li H., Wolf P., Moser P., Larisch G., Lott J. A., Bimberg D., Temperature-Stable 980-nm VCSELs for 35-Gb/s Operation at 85 °C With 139-fJ/bit Dissipated Heat, IEEE Photonics Technology Letters, vol. 26, n0. 23, 2014

[34] Li H., Wolf P., Moser P., Larisch G., Lott J. A., Bimberg D., Vertical-cavity surface-emitting lasers for optical interconnects, SPIE, doi 10.1117/2.1201411.005689

[35] Toprasertpong K., Novel Analysis Method of Carrier Transport in Quantum Wells for 4-Junction Solar Cells, Master's thesis, Dep. of Elect. Eng. and Inf. Sys, The University of Tokyo, 2014

[36] Toprasertpong K., Fujii H., Thomas T., Führer M., Alonso-Álvarez D., Farrell D. J., Watanabe K., Okada Y., Ekins-Daukes N. J., Sugiyama M., Nakano Y., Absorption threshold extended to 1.15eV using InGaAs/GaAsP quantum wells for over-50%-efficient lattice-matched quad-junction solar cells, Prog. Photovolt: Res. Appl. (2015)

[37] Asada M., Suematsu Y., Density-Matrix Theory of Semiconductor Lasers with Relexation Broadening Molde-Gain and Gain-Suppression in Semiconductor Lasers, IEEE Journal of Quantum Electronics, Vol. QE-21, No. 5, (1985)

[38] Park, Y. H., Kang, B-K., Lee S., woo, D. H., Kim S. H., Structure of the Quantum Well for a Broad-Band Semiconductor Optical Amplifier, Journal of the Korean Phys. Soc., Vol. 36, No. 4, (2000)

[39] Makino T., Analytical Formuals for the Optical Gain of Quantum Wells, IEEE Journal of Quantum Electronics, Vol. 32, No. 3, (1996)

[40] Steed R., Quantum Wells with Multiple Intersubband Transitions, Theory Notes (2016)

[41] Gallep C. M., Conforti E., Simulation of single quantum-well semiconductor optical amplifiers, SBMO/IEEE MTT-S IMOC 2001 Proceedings, (2001)

[42] Photon Design, Harold version 5.0.2, user manual.

[43] Vurgaftman I., Meyer J. R., Ram-Mohan L. R., Band parameters for III–V compound semiconductors and their alloys, Jounal of Applied Physics, Vol. 89, No. 11, (2001)

[44] Vukovic M., Design and Fabrication of InGaAsP Quantum-well Seminconductor Optical Amplifiers for Integration with Silicaon Photonics, Master Thesis, (2020)

[45] Phkubo M., Ijichi T., Iketani A., Kikuta T., 980-nm Aluminium-Free InGaAs/InGaAsP/InGaP GRIN-SCH SL-QW Lasers, IEEE Journal of Quantum Electronics, Vol. 30, No. 2, (1994)

[46] Asonen H., Ovtchinnikov A., Zhang G., Nappi J., Pessa M., Aluminium-Free 980-nm GaInAs/GaInAsP/GaInP Pump Lasers, IEEE Journal of Quantum Electronics, Vol. 30, No. 2, (1994)

[47] Fukuda M., Okayasu M., Temmyo J., Nakano, J., Degradation Behavior of 0.98- μm Stained Quantum Well InGaAs/AlGaAs Lasers Under High-Power Operation, IEEE Journal of Quantum Electronics, Vol. 30, No. 2, (1994)

[48] Sagawa M., Toyonaka T., Hiramoto K., Shinoda K., Uomi K., High-Power Highly-Reliable Operation of 0.98- μm InGaAs-InGaP Strain-Compensated Single-Quantum-Well Lasers with Tensile-Strained InGaAsP Barriers, IEEE Journal of Selected Topics in Quantum Electronics, Vol.1, No. 2, (1995)

[49] Zhang G., Ovtchinnikov A., Temperature sensitivity of strained-layer InGaAs/Ga(In)As(P)/GaInP separate-confinement heterostructure quantum well lasers ($\lambda \approx$980 nm), Journal of Applied Physics, Vol. 73, (1993)

[50] Chinn S. R., Zory P. S., Reisinger A. R., A Model for GRIN-SCH-SQW Diode Lasers, IEEE Journal of Quantum Electronics, vol. 24, No. 11, (1988)

[51] Yamanishi M., Lee Y., Phase dampings of optical dipole moments and gain spectra in semiconductor lasers, Journal of Quantum Electronics, vol. 23, No. 4, (1987)

[52] Yu P. Y., Cardona M., Fundamentals of Semiconductors, Physics and Material Properties, Springer

[53] El-Saba M., Energy band theory

[54] Levi A. F. J., Essential Semiconductor Laser Device Physics, Morgan & Claypool, 2018

[55] Ashcroft N. W., Mermin N. D., Solid State Physics, Harcourt College Publishing, 1976

[56] Kittel C., Introduction to Solid State Physics, 8th edition, John Wiley & Sons, 2005

[57] Willatzen M., Lew Yan Voon L. C., The k.p method, Electronic properties of semiconductors, Springer, 2009

[58] Deen J., Basu P. K, Silicon photonics: Fundamentals and devices, Wily, 2012

[59] Singh J., Electronic and Optoelectronic Properties of Semiconductor Structures, Cambridge University Press, 2003

[60] Singleton J., Band theory and electronic properties of solid, Oxford master series in condensed matter physics, Oxford University Press, 2001

[61] Sharma R. O., Saini L. K., Prasad Bahuguna B., Quantum Monte Carlo Study of Buckled GaAs Monolayer, Macromolecualr Symposia, doi: 10.1002/masy.201600206

[62] Yang Y., Orelov V., Pierleoni C., Ceperley D. M., Holzmann M., Electronic band gaps from Quantum Monte Carlo methods, 2019, arXiv 1910.07531

[63] Cakan A., Sevik C., Bulutay C., Strained band edge characteristics from hybrid density functional theory and empirical pseudopotentials: GaAs, GaSb, InAs and InSb, 2016, arXiv 1605.06807v1

[64] Cardona M., Pollak F. H., Energy-Band Structure of Germanium and Silicon: The $\mathbf{k} \cdot \mathbf{p}$ Method, Physical review, vol. 142, no. 2, 1966

[65] Barnham K., Vvedensky D., Low-dimensional semiconductor structures, Fundamental and device applications, Cambridge University Press, 2001

[66] Chuang S. L., Physics of Optoelectronic Devices, John Wiley & Sons, 1995

[67] Connelly M. J., Semiconductor Optical Amplifiers, Kluwer Academic Publishers, 2004

[68] Piprek J., Semiconductor Optoelectronic Devices, Introduction to Physics and Simulation, Academic Press, Elsevier Science, 2003

[69] Dutta N. K., Wang Q., Semiconductor Optical Amplifiers, World Scientific Publishing, 2006

[70] Bahder T. B., Eight-band k.p model of strained zinc-blende crystals, Physical review B, Vol. 41, no. 16, 1990

[71] Holmstedt J., Svensson V., Porsteinsson D. O., GaAs band structure calculation using k.p theory including strain, 2015

[72] Saidi O., Ben Radhia S., Boujdaria K., Band structures of GaAs, InAs, and InP: A 34 k.p model, Journal of applied physics 104, 2008

[73] Ostromek T. E., Evaluation of matrix elements of the 838 k–p Hamiltonian with k-dependent spin-orbit contributions for the zinc-blende structure of GaAs, Physical review B, Vol. 54, no. 20, 1996

[74] Gladysiewicz, Kudrawiec R., Wartak M. S., 8-band and 14-band kp modeling of electronic band structure and material gain in Ga(In)AsBi quantum wells grown on GaAs and InP substrates, Journal of applied physics 118, 2015

[75] Wartak M.S., Weetman P., Alajoki T., Aikio J., Heikkinen V., Pikhtin N.A., Rusek P., Optical modal gain in multiple quantum-well semiconductor lasers based on InP, Can. J. of Phys. 84, 2006.

[76] Connelly M. J., Wideband semiconductor optional amplifier steady-state numerical model, IEEE Journal of quantum electronics, vol. 37, no. 3, 2001

[77] Manzhos S., Machine learning for the solution of the Schrödinger equation, Machine Learning: Science and Technology, vol. 1, no.1, 2020.

[78] Huang L. Wang L., Accelerate Monte Carlo Simulations with Restricted Boltzmann Machines, Physical Review B 95, 035105, 2017

[79] Borin A., Abanin D. A., Approximating power of machine-learning ansatz for quantum many-body states, Physical Review B 101, 195141, 2020

[80] Carleo G., Troyer M., Solving the Quantum Many-Body Problem with Artificial Neural Networks, Science, vol. 355, issue 6325, 2017

[81] Carrasquilla J., A machine learning perspective on the many-body problem in classical and quantum physics, Deep learning for physical sciences 31st NIPS Conference, 2017, https://www.youtube.com/watch?v=mSo2ODzeI1k

[82] Vistnes A. I., Physics of Oscillations and Waves with use of Matlab and Python, Springer International, 2018, doi: 10.1007/978-3-319-72314-3_1...16

[83] Dasgupta K., Course: Physics 551 Quantum Theory, Motion of a charged particle in a magnetic field, McGill University, http://www.physics.mcgill.ca/~keshav/551/QHE.pdf

[84] Wolski A., Lectures: Theory of Electromagnetic Fields, Part I: Maxwell's Equations, Cockcroft Institute, University of Liverpool, 2010.

[85] Press W. H., Teukolsky S. A., Vetterling W. T., Flannery B. P., Numerical recipes in C, the Art of Scientific Computing, Cambridge University Press.

[86] Bathia R., Algebraic Geometry Solves an Old Matrix Problem, Resonance 1999.

[87] Alonso-Alvarez D., Wilson T., Pearce P., Fuhrer M., Farell D., Ekins-Daukes N., Solcore: a multi-scale, Python-based library for modelling solar cells and semiconductor materials, Journal of Computational Electronics, 2018.

[88] New Semiconductor Materials. Biology systems. Characteristics and Properties. http://www.ioffe.ru/SVA/NSM/Semicond

[89] RefractiveIndex.info, https://refractiveindex.info/

[90] Levinshtein M., Rumyantsev S., Shur M., Handbook Series on Semiconductor Parameter, World Scientific, 1996.

[91] Adachi S., Material parameters of In_{1-x} $Ga_xAs_yP_{1-y}$ and related binaries, J. Appl. Phys. 53(12), December 1982

[92] Takizawa T., J. Phys. Soc. Jpn. 52, 3 (1983) 1057-1063

[93] Nkanta J. E., Maldonado-Basilio R., Benhsaien A., Khan K., Abdul-Majid S., Zhang J., Hall T. J., Characterization of an Asymmetric InGaAsP/InP Multi Quantum Well Semiconductor Optical Amplifier, Proc. of SPIE Vol. 8915, 2013

[94] Ikeda S., Shimizu A., Hara T., Asymmetric dual quantum well laser—wavelength switching controlled by injection current, Applied Physics Letters 55, 1155, 1989

[95] Ito T., Yoshimoto N., Magari K., Wide-Band Polarization-Independent Tensile-Strained InGaAs MQW-SOA Gate, IEEE Photonics Technology Letters, vol. 10, no. 5, May 1998

[96] Koonath P., Kim S., Cho W-J., Gopinath A., Polarization-Insensitive Quantum-Well Semiconductor Optical Amplifiers, IEEE Journal of Quantum Electronics, vol. 38, no. 9, Sep. 2002

[97] Lysak V.V., Kawaguchi H., Sukhoivanov I. A., Gain spectra and saturation power of asymmetrical multiple quantum well semiconductor optical amplifiers, IEE Proc.-Optoelectron., Vol. 152, No. 2, April 2005

[98] Morito K., Ekawa M., Watanabe T., and Yuji Kotaki, High-Output-Power Polarization-Insensitive Semiconductor Optical Amplifier, Journal of Lightwave Technology, vol. 21, no. 1, Jan 2003

[99] Raring J. W. , Skogen E. J., Mašanović M. L., DenBaars S. P., Coldren L. A., Demonstration of high saturation power/high gain SOAs using quantum well intermixing based integration platform, 2005

[100] Tiemeijer L. F., Thijs P. J. A., van Dongen T., Binsrna J. J. M., Jansen E. J., Polarization Resolved, Complete Characterization of 1310 nm Fiber Pigtailed Multiple-Quantum-Well Optical Amplifiers, Journal of Lightwave Technology, vol. 14, no. 6, June 1996

[101] Zhu, Cassidy D. T., Hamp M. J., Thompson D. A., Robinson B. J., Zhao Q. C., Davies M., 1.4-μm InGaAsP–InP Strained Multiple-Quantum-Well Laser for Broad-Wavelength Tunability, IEEE Photonics Technology Letters, vol. 9, no. 9, Sep. 1997

[102] Prasanth R., Haverkort J. E. M., Wolter J. H., InAsP/InGaAs composite quantum well for separate TE and TM gain, Applied Physics Letters 88, 2006